EXPERIMENTAL STUDY ON SUBCOOLED FLOW BOILING ON HEATING SURFACES WITH DIFFERENT THERMAL CONDUCTIVITIES

BY

LING ZOU

DISSERTATION

Submitted in partial fulfillment of the requirements
for the degree of Doctor of Philosophy in Nuclear Engineering
in the Graduate Collage of the
University of Illinois at Urbana-Champaign, 2010

Urbana, Illinois

Doctoral Committee:

Professor Barclay G. Jones, Chair
Professor Roy A. Axford
Professor Rizwan Uddin
Professor Ty A. Newell

ABSTRACT

Subcooled flow boiling is generally characterized by high heat transfer capacity and low wall superheat, which is essential for cooling applications requiring high heat transfer rate, such as nuclear reactors and fossil boilers. In this study, subcooled flow boiling on copper and stainless steel heating surfaces was experimentally investigated from both macroscopic and microscopic points of view.

Flow boiling heat flux and heat transfer coefficient were experimentally measured on both surfaces under different conditions, such as pressure, flow rate and inlet subcooling. Significant boiling heat transfer coefficient differences were found between the copper and the stainless steel heating surfaces. To explain the different flow boiling behaviors on these two heating surfaces, nucleation site density and bubble dynamics were visually observed and measured at different experimental conditions utilizing a high-speed digital video camera. These two parameters are believed to be keys in determining flow boiling heat flux. Wall superheat, critical cavity size and wall heat flux were used to correlate with nucleation site density data. Among them, wall heat flux shows the best correlation for eliminating both pressure and surface property effects. The observed nucleation site distribution shows a random distribution. When compared to the spatial Poisson distribution, similarity between them was found, while the measured nucleation site distribution is more uniform. From experimental observations, for the two surface materials investigated, which have similar surface wettability but sharply different thermal properties, bubble dynamics displayed fairly similar behavior. The obtained experimental results indicate that thermal conductivity of heating surface material plays an important role in boiling heat transfer. This is due to thermal conductivity having a significant impact on the lateral heat conduction at the heating surface and consequently temperature uniformity of the heating surface.

A model was then developed and solved numerically for heat conduction at the heating surface when bubbles are present. Several key parameters which impact lateral heat conduction and surface temperature profile were studied. These parameters include material

thermal conductivity, bubble size, heating surface thickness, etc. Numerical results show that, temperature profile on the heating surface tends to be more uniform and have a lower average value on a heating surface with higher thermal conductivity, which agrees well with the experimental observation.

ACKNOWLEDGEMENTS

I would like to express my deepest appreciation to my advisor and committee chair, Dr. Barclay G. Jones, for his excellent advising, inspiring discussion and guidance on the research during my thesis work. Without Dr. Jones' persistent support on both academic and general fields, this dissertation would not have been possible. I would like to thank Dr. Ty A. Newell for his support on experimental facilities and his guidance on my thesis work. I would also like to thank Dr. Roy A. Axford and Dr. Rizwan Uddin, for being my committee members and giving invaluable suggestions on my dissertation.

A special thank goes to Dr. Wen Wu and Dr. Emad W. Jassim for sharing the knowledge on image processing and conducting experiments.

Lastly, I would like to express my appreciation to my family: my parents and brother, my wife and my baby girl. Without their love and encouragement, this dissertation wouldn't have happened. I dedicate this thesis to them.

TABLE OF CONTENTS

LIST OF FIGURES

Figure

LIST OF TABLES

Table

NOMENCLATURE

Bo	Bond number
Co	Convection number
C_p	Specific heat
D	Bubble diameter
D_c	Critical cavity diameter
D_h	Hydraulic diameter
f	Bubble frequency
F	Force
Fr	Froude number
G	Mass flow rate
h	Heat transfer coefficient
h_{fg}	Latent heat
Ja	Jacob number
k	Thermal conductivity
N_a	Nucleation site density
Nu	Nusselt number
p	Pressure
Pr	Prandtl number
q, q''	Heat flux
r	Surface cavity radius
R	Bubble radius
R_e	Reynolds number
T	Temperature
t	Time
v	Velocity

Greek symbols

α	Thermal diffusivity
β	Half cone angle of a cavity
δ	Thickness of thermal boundary layer
ΔT_w	Wall superheat
θ	Contact angle
μ	Dynamic viscosity
v	Kinetic viscosity
ρ	Density
σ	Surface tension
υ	Specific volume

Subscripts

b	Bubble
bi	Boiling
c	Critical
d	Departure
f	Liquid phase
fc	Forced convection
g	Growth
g	Vapor phase
i	Inlet
l	Liquid phase
max	Maximum
min	Minimum
o	Outlet
s	Surface
sat	Saturation

sp	Single phase flow
sub	Subcooled
tc	Transient conduction
tp	Two phase flow
v	Vapor phase
w	Wall
w	Waiting

CHAPTER 1

INTRODUCTION

Boiling heat transfer is defined as a process in which intensive liquid to vapor phase change occurs. It's normally characterized by a high heat transfer capacity and a low wall temperature, which is essential for industrial cooling applications requiring high heat transfer capacities, such as nuclear reactors and fossil boilers. Due to its importance in industry, a large amount of researches have been extensively carried out to study the boiling heat transfer capacity and mechanism.

The boiling phenomenon has been systematically studied since early last century. Nukiyama (Tong and Tang 1997, 2) was the first to propose the concept of a 'boiling curve', in which the wall heat flux is plotted against the wall superheat, Figure 1.1. In the nucleate boiling regime, region B-C in Figure 1.1, intense phase change with bubble formation occurs. A large portion of the energy is transferred into the bulk liquid in the form of latent heat carried by bubbles.

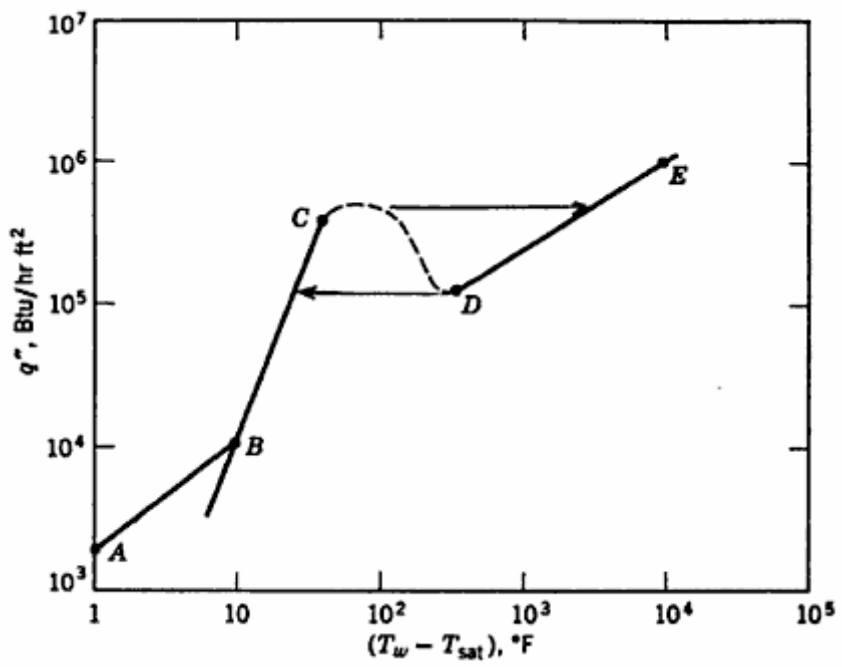

Figure 1.1. A typical pool boiling curve. A-B, natural convection regime; B-C, nucleate boiling regime; C-D, partial film boiling; D-E, stable film boiling. (Tong and Tang 1997, 2)

In general, boiling phenomena are divided into two major categories, pool boiling and flow boiling. Pool boiling is a process in which the heating surface is submerged in a liquid pool, while flow boiling is normally confined to flow channels. The major difference between these two is the presence of a forced liquid flow in flow boiling. The flow boiling phenomenon has attracted a lot of researches for its high heat transfer rate and wide applications in industry. As the flow boiling is widely used, many early efforts were devoted to predicting its performance, such as experimental measurement of the heat transfer coefficient and critical heat flux under different conditions. Parametric studies were also carried out to understand the impacts of several key parameters, such as fluid velocity, inlet subcooling level, heating surface materials and surface roughness conditions. Based on experimental work, empirical and semi-empirical correlations were proposed for industry applications. Some representative correlations include McAdam's (McAdams et al. 1949), Chen's (Chen 1966), etc. As an example, Figure 1.2 shows the effects of liquid velocity and inlet subcooling level on subcooled flow boiling heat transfer, given by McAdams (Collier and Thome 1996, 204).

Other than direct experimental measurements, model development efforts were also devoted to understanding the boiling mechanisms, such as nucleation site activation criteria, bubble dynamics, bubble interactions, etc. Bankoff (Bankoff 1958) first examined gas entrapment in cavities present on heating surfaces, and a criterion was set up to identify a potential nucleation site. Griffith (Griffith and Wallis 1960) proposed a model to study the role of surface conditions in nucleate boiling, from which the wall superheat required to active a nucleation site is established. In recent years, with utilizations of new technologies, such as high-speed cameras and liquid crystal thermography, more details of the boiling phenomena were successfully revealed. For example, both bubble growth rate and departure size could be visually captured by the advanced high-speed camera. The technology of liquid crystal thermography was used to measure surface temperature profiles around an active

nucleation site. A laser was employed to artificially activate multiple bubbles with desired separation distances. This was used to study boiling chaos due to bubble interactions.

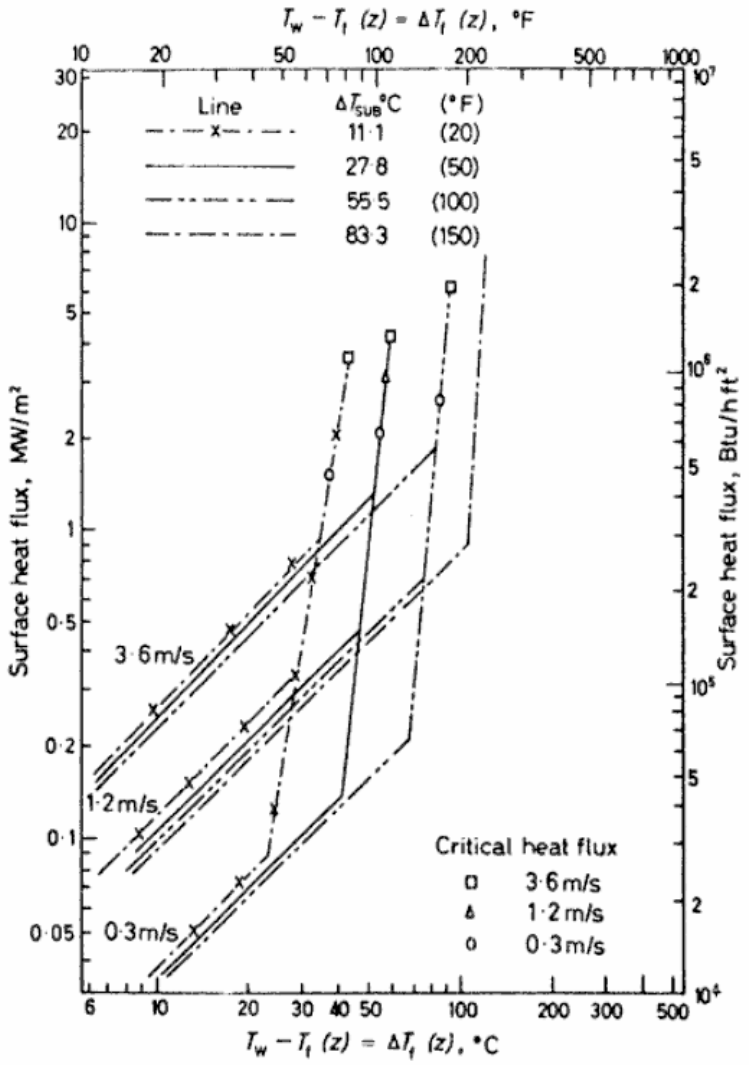

Figure 1.2. Effects of liquid velocity and inlet subcooling level on subcooled flow boiling heat transfer (Collier and Thome 1996, 204)

Subcooled flow boiling compared to saturated flow boiling, is referred as a flow boiling process with bulk flow temperature lower than saturation level. Figure 1.3 shows typical transitions from forced single-phase convection to subcooled flow boiling and to saturated flow boiling. The transition from single-phase convection to subcooled flow boiling is sometimes referred as the onset of nucleate boiling (ONB). After ONB, bubbles start to generate on the heating surface, they enhance the heat transfer. As bubble numbers increase, heat carried by bubbles becomes a large portion of the total energy transferred. The transition

from subcooled flow boiling to saturated flow boiling occurs as the bulk temperature reaches the saturation point. Subcooled flow boiling is of interest to the nuclear industry because it's present in typical pressurized water reactors (PWR) and plays an important role in the cooling of the rector core. Other than the high heat transfer rate which is essential for nuclear reactor performance, subcooled flow boiling has been identified as a possible reason to induce CRUD (Chalk River Unidentified Deposits) layer formation on fuel rods. This layer potentially causes the undesired reactor power shift, normally referred as axial offset anomaly (AOA). In addition, the understanding of critical heat flux in subcooled flow boiling is essential for designing nuclear reactors.

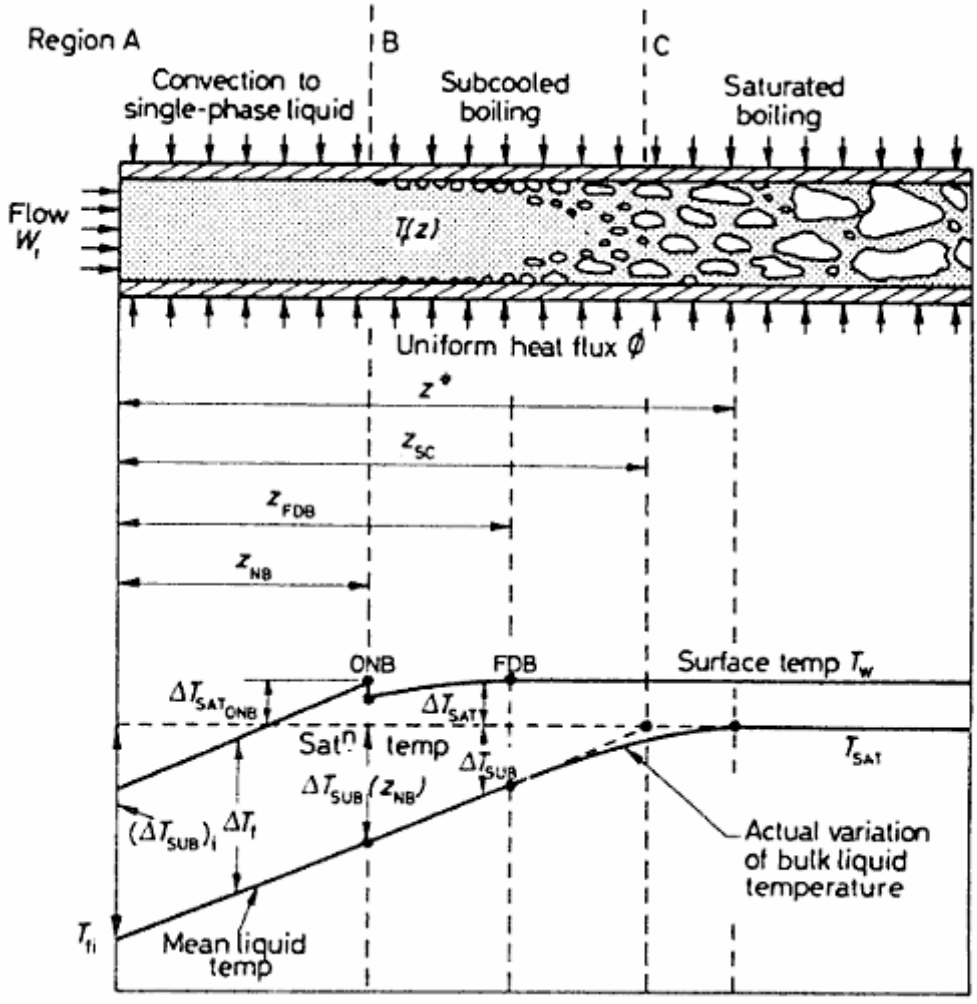

Figure 1.3. Surface and liquid temperatures distribution in a flow boiling (Collier and Thome 1996, 184)

The objective of this thesis is to experimentally study subcooled flow boiling with a simulant fluid, R134a, from both macroscopic and microscopic points of view. The experimental work includes three major parts, e.g., subcooled flow boiling performance from the macroscopic point of view, nucleation site density and distribution, and bubble dynamics from the microscopic point of view. The subcooled flow boiling performance can be directly estimated by measuring the heating surface temperature and wall heat flux. The nucleation site density, its distribution and bubble dynamics can be obtained from images and videos taken by a high-speed digital camera. The effects of surface materials, or more specifically their thermal properties and wettability of R134a, will also be examined by employing two heating surfaces made of copper and of stainless steel. The measurement of subcooled flow boiling heat transfer rate and nucleation site density and observation of bubble dynamics will be studied on both surfaces to examine the heating surface material effects. A simplified heat transfer model to study heat conduction within the heating block is then proposed to explain the different flow boiling behaviors of the two surface materials.

CHAPTER 2

LITERATURE REVIEW

During the past decades, extensive efforts have been devoted to understanding boiling phenomena, including both pool boiling and flow boiling. These efforts include direct experimental measurements and observations, theoretical analyses, empirical correlations, model developments, etc. In recent years, with the help of state-of-the art technologies, such as high-speed digital cameras and thermochromic liquid crystals, more insightful information has been obtained to understand the boiling process. Some of the latest findings include knowledge on fundamental bubble dynamics, active nucleation site densities, bubbles and nucleation site interactions, heat flux predictions, critical heat flux models, etc. The literature review presented in this chapter will mainly focus on several key topics of subcooled flow boiling heat transfer. These include activation of nucleation sites, their densities and distributions, bubble dynamics, and subcooled flow boiling heat transfer correlations and models.

2.1 NUCLEATION SITES AND NUCLEATION SITE DENSITY

The importance of heating surface conditions to boiling processes has been recognized for decades. It has been found that bubbles originate from preexisting vapor or gas pockets captured in pits, cavities, scratches and grooves (all generally referred as cavities) on a heating surface. The cavity size and shape have proved to be critical to entrap vapor and/or gas and to initiate a bubble, and have already been explored by various researchers. In addition, the active nucleation site density is a key parameter to predicting the boiling heat flux, and has been extensively studied. The following section gives some of the important research on nucleation sites, their densities and distributions.

Bankoff (Bankoff 1958) examined the entrapment of gas in the spreading of a liquid on a rough surface. It was found that the contact angle and surface cavity geometry were important parameters during the incomplete displacement of gas from the cavity valley by a liquid drop advancing over the cavity ridges. As shown in Figure 2.1, the liquid contact angle is θ, and the angle between ridge and horizontal line is ϕ. To entrap gas volume in the valley, the following criteria must be satisfied,

$$\theta > 180^o - 2\phi \tag{2-1}$$

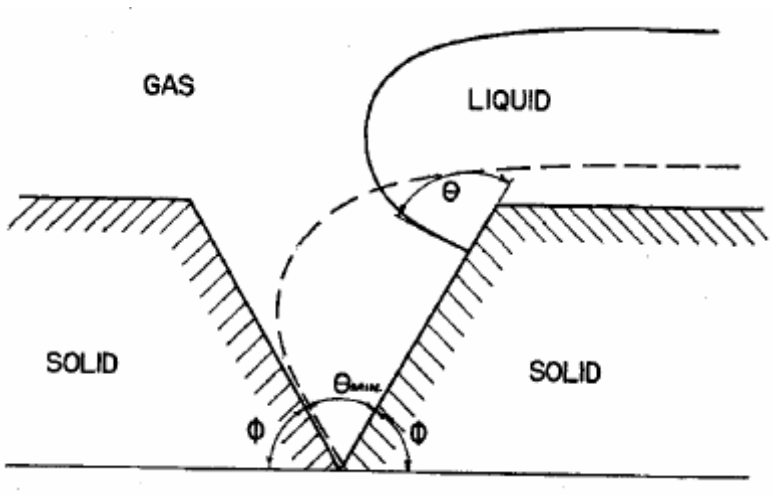

Figure 2.1. Conditions for entrapment of gas in the advancing of a semi-infinite liquid sheet across a groove (Bankoff 1958).

Griffith and Wallis (Griffith and Wallis 1960) proposed a model to study the role of surface conditions in nucleate boiling. Considering a stable bubble forming on a conical cavity, the pressure difference between the vapor phase inside the bubble and the surrounding superheated liquid phase is governed by the Gibbs equation,

$$\Delta p = \frac{2\sigma}{r} \tag{2-2}$$

The vapor phase inside a bubble is assumed to be at saturation temperature corresponding to its pressure and the surrounding liquid is at the same temperature and,

therefore, superheated. The minimum wall superheat which is needed to initiate a bubble from a cavity with a mouth radius r^* can be calculated by the Clapeyron relation,

$$r^* = \frac{2\sigma T_w \upsilon_{fg}}{h_{fg}\left(T_w - T_{sat}\right)} \tag{2-3}$$

However, a question has been raised as to whether the wall superheat would eventually vanish if the cavity size were to increase without bound, if Griffith's equation stands. This contradicts the fact that a boiling process has to occur at a certain level of wall superheat. By including the temperature gradient in the liquid thermal layer adjacent to the heating wall, Hsu (Hsu 1962) concluded that nucleation sites could only be effective within a certain size range. This size is a function of liquid subcooling level, system pressure, liquid/vapor properties and thickness of the superheated liquid layer. As shown in Figure 2.2, the liquid temperature at the top of the bubble has to satisfy Griffith's criteria, equation 2-2. Combing the temperature gradient in the liquid superheated layer and equation 2-2, a quadratic equation was obtained which gives the minimum and maximum cavity sizes for a given wall superheat,

$$\left\{r_{c,\min}, r_{c,\max}\right\} = \frac{\delta}{2C_1}\frac{\Delta T_w}{\Delta T_w + \Delta T_{sub}}\left[1 \mp \sqrt{1 - \frac{8\sigma T_{sat} C_3\left(\Delta T_w + \Delta T_{sub}\right)}{h_{fg}\rho_v \delta \Delta T_w{}^2}}\right] \tag{2-4}$$

in which, δ is the thickness of the superheated liquid layer; constants C_1 and C_3 are functions of the contact angle, φ.

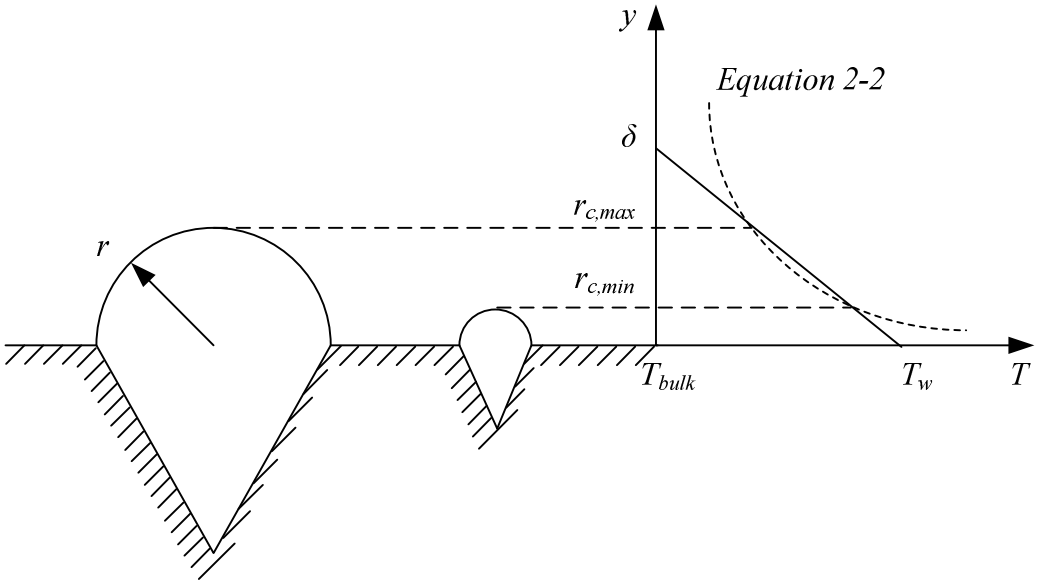

Figure 2.2, Hsu's criteria to determine the maximum and minimum nucleation cavity size at a given wall superheat

In a later study by Han and Griffith (Han and Griffith 1965), a liquid contact angle of 90 deg and critical bubble height of 3/2 r_c were assumed. The constants, C_1 and C_3 in equation (2-3) were both solved equal to 3/2, and equation (2-3) was rewritten as,

$$\left\{r_{c,\min}, r_{c,\max}\right\} = \frac{\delta}{3}\frac{\Delta T_w}{\Delta T_w + \Delta T_{sub}}\left[1 \mp \sqrt{1 - \frac{12\sigma T_{sat} C_3 \left(\Delta T_w + \Delta T_{sub}\right)}{h_{fg}\rho_v \delta \Delta T_w{}^2}}\right] \tag{2-5}$$

Kandlikar et al. (Kandlikar et al. 1997) later numerically solved the flow distribution on a truncated bubble to obtain the stagnant point of a bubble. It was found that the distance from the stagnant point to the heating surface is around 1.1 times the bubble radius. Hsu's equation then became,

$$\left\{r_{c,\min}, r_{c,\max}\right\} = \frac{\delta \sin\varphi}{2.2}\frac{\Delta T_w}{\Delta T_w + \Delta T_{sub}}\left[1 \mp \sqrt{1 - \frac{9.2\sigma T_{sat} C_3 \left(\Delta T_w + \Delta T_{sub}\right)}{h_{fg}\rho_v \delta \Delta T_w{}^2}}\right] \tag{2-6}$$

in which, φ is the contact angle.

In addition to analytical work, direct experimental measurements were also done to understand the relationship among wall superheat, nucleation site density and heat transfer

rate during boiling. The umber of nucleation sites was counted throughout the nucleate boiling region by Gaertner and Westwater (Gaertner and Westwater 1963). An aqueous solution of nickel salts containing 20% solid was boiled at atmospheric pressure on a horizontal, flat copper surface. The number of boiling sites was then counted from the nickel salts deposition. Other than a liner relationship, the heat flux was found to be proportional approximately to the square root of the number of sites.

Eddington and Kenning (Eddington and Kenning 1978) used a gas bubble nucleation method to study bubble nucleation from a supersaturated gas solution to compare with bubble formation during boiling processes. A same stainless steel surface having 0.8 mm thickness was used in both gas nucleation experiments and flow boiling experiments. The comparison between these two kinds of experiments showed that there were many more sites in the gas bubble nucleation method, which satisfied the site activation criteria, equation (2-2), than were actually observed on the same surface during the boiling process. It was found that site seeding and thermal interference, which were not present in gas nucleation experiments, caused the difference between the gas nucleation and flow boiling experiments. A similar result was also found by Eddington et al. (Eddington et al. 1978) from comparison of gas and vapor bubble nucleation numbers on a brass surface in water. The authors suggested that the contact angle might play an important role. The effect of contact angle was later examined from comparison of the gas bubbles formed in supersaturated solutions of nitrogen in water and ethanol-water mixtures on two metal surfaces by Eddington and Kenning (Eddington and Kenning 1979). It was found that a decrease in contact angle results in a decreasing bubble nucleation site density.

Bergles and Rohsenow (Bergles and Rohsenow 1964) stated that on a commercial surface the cavity size covered wide range and therefore the onset of boiling was surface condition independent. The heat flux at onset of boiling could only be a function of fluid and thermal properties, such as system pressure and wall superheat. However, in a later work, Mikic and Rohsenow (Mikic and Rohsenow 1969) related the active nucleation site density to

the surface cavity size. It's been found that the active nucleation site density is inversely proportional to the power function of the critical size,

$$Na \sim \left[\frac{D_s}{D_c}\right]^{6.5} \tag{2-7}$$

in which, D_s is the maximum cavity size present on the heating surface and D_c is the critical diameter derived from equation (2-2),

$$D_c = \frac{4\sigma T_w \upsilon_{fg}}{h_{fg}\left(T_w - T_s\right)} \tag{2-8}$$

A similar correlation proposed by Bier et al. (Bier et al. 1978) also expressed the active nucleation site density as a function of cavity size,

$$\ln Na = \ln\left(N_{\max}\right)\left[1-\left(\frac{D_s}{D_c}\right)^m\right] \tag{2-9}$$

in which, N_{max} is the value corresponding to $D_c = 0$ andthe empirical constant, m, was found to be dependent on the surface preparation procedure. For boiling of Freon-115 and Freon-11 on copper surfaces, the value of m was found to be 0.42 and 0.26, respectively.

Cornwell and Brown (Cornwell and Brown 1978) studied water boiling on copper surfaces at atmospheric pressure with different surface conditions from smooth to rough. The active nucleation site density was found to be proportional to a power function of the wall superheat, or inversely proportional to a power function of the critical cavity size,

$$Na \sim \Delta T_w{}^{4.5} = \frac{1.36\times 10^{-19}}{D_c{}^{4.5}} \tag{2-10}$$

Kocamustafaogullari and Ishii (Kocamustafaogullari and Ishii 1983) correlated existing pool boiling nucleation site density data by means of parametric study. It's assumed that the nucleation site density in pool boiling, N_{np}, is a function of both surface conditions and fluid thermo-physical properties. Mainly based on existing water data, a non-dimensional correlation was proposed,

$$N_{np}{}^* = f\left(\rho^*\right) R_c{}^{*-4.4} \tag{2-11}$$

in which, $N_{np}^{*} \equiv N_{np} D_d^{\,2}$ (2-12)

$$f(\rho^{*}) = 2.157 \times 10^{-7} \rho^{*-3.2} \left(1 + 0.0049 \rho^{*}\right)^{4.13} \tag{2-13}$$

$$\rho^{*} \equiv \frac{\rho_f - \rho_g}{\rho_g} \tag{2-14}$$

$$R_c^{*} \equiv \left(R_c / \left(D_d / 2\right)\right) \tag{2-15}$$

in which, D_d is the departure diameter, which can be estimated from an empirical correlation. Taking account of the difference between the effective liquid superheat, $\Delta T_e = S \Delta T_w$, and the similarity between pool and convective boiling, Kocamustafaogullari and Ishii concluded that the proposed nucleation site density correlation for pool boiling could be used for convective boiling by replacing the wall superheat with an effective superheat, proposing for flow boiling that,

$$N_{np}^{*} = f(\rho^{*}) R_c^{*-4.4} \tag{2-16}$$

An approach was made by Yang and Kim (Yang and Kim 1988) to correlate active nucleation site density with the measured statistical boiling surface parameters, such as cavity size and cone angle distribution. From measurements using a scanning electron microscope and a differential interference contrast microscope, they concluded that the cavity size and cone angle could be fit by a Poisson and a normal distribution, respectively. The cavity radius follows a Poisson distribution,

$$f(r) = \lambda \exp(-\lambda r) \tag{2-17}$$

The cone angle follows a normal distribution,

$$f(\beta) = \frac{1}{\sqrt{2\pi} s} \exp\left[-\left(\beta - \overline{\beta}\right)^2 / \left(2 s^2\right)\right] \tag{2-18}$$

in which, r and λ are cavity radius and it's statistical parameter, respectively. β, $\overline{\beta}$ and s are the half cone angle, its mean value and standard deviation, respectively. Following the gas entrapment criteria proposed by Bankoff (Bankoff 1958), Yang and Kim proposed that the active nucleation site density could be determined as,

$$N_a = \overline{N_n}\int_0^{\theta/2} f(\beta)d\beta \int_{R_c}^{R_s} f(r)dr \tag{2-19}$$

where, $\overline{N_n}$ is the average cavity density, which may only depend on heating surface material and finish. For a given surface condition, Yang and Kim further approximated equation (2-19) in the form of,

$$N_a \approx C\exp(-K/\Delta T_{sat}) \tag{2-20}$$

where, parameters *C* and *K* account for the surface conditions effect and liquid properties effect.

Similar work was later performed by Hibiki and Ishii (Hibiki and Ishii 2003), who suggested different cavity size and cone angle distribution functions other than Poisson and normal distributions. Based on Yang and Kim's (Yang and Kim 1988) data, the cavity size and cone angle distribution functions were expressed as,

$$f(r) = \frac{\lambda}{r^2}\exp\left(\frac{\lambda}{r}\right) \tag{2-21}$$

and,

$$f(\beta) = \frac{\beta}{\mu^2}\exp\left[-\beta^2/(2\mu^2)\right] \tag{2-22}$$

The active nucleation site density can be calculated from equation (2-19). The proposed model shows a maximum 60% error in comparison with experimental data over a wide range of flow conditions, 0~886 kg/m^{2}s of mass flux, 0.101~19.8 MPa of pressure, 5~90^o of contact angle, 1.0×10^4~1.51×10^{10} of nucleation site density.

Different cavity size and cone angle distributions were also proposed by Qi et al. (Qi et al. 2004). A gas nucleation technique was used to examine the active nucleation site density of water on brass and stainless steel surfaces. The surface profiles were examined by a Wyko NT1000 vertical scanning interferometer (VSI). It was found that the best fit to the cavity size distribution followed a Weibull distribution,

$$f(d) = \frac{\lambda}{\omega}\left(\frac{d}{\omega}\right)^{\lambda-1}\exp\left[-\left(\frac{d}{\omega}\right)^{\lambda}\right] \tag{2-23}$$

where, d is the cavity diameter. λ and ω are functions of the mean and standard deviation. The cavity half cone angles were best represented by the function,

$$g(\beta) = \frac{A\left(\frac{\pi}{2} - \beta\right)^2}{B + \left(\frac{\pi}{2} - \beta\right)^6} \tag{2-24}$$

where, A and B are constants empirically determined. The active nucleation sites were estimated by equation (2-19) proposed by Yang and Kim (Yang and Kim 1988). However, Qi's model did not give good agreement with nucleation site density data from the gas nucleation technique. The author stated that, "the statistical method for predicting nucleation site density on commercial heat transfer surfaces with randomly distributed cavities is not likely to be accurate using the current state-of-the-art in surface metrology technology".

Wang and Dhir (Wang and Dhir 1993a) proposed an empirical correlation to include the effect of static contact angle on active nucleation site density based on their water pool boiling data on vertical copper surfaces at atmospheric pressure. The original surface had a mirror finish and had a very small surface roughness value, around 0.02 μm. With different degrees of surface oxidization, the surface wettability changed. The static contact angles of the water-copper combination were measured ranging from 18˚ to 90˚. The active nucleation site density was correlated by Wang and Dhir as,

$$N_a\left(sites/cm^2\right) = 5.0\times10^5\left(1-\cos\theta\right)D_c^{-6.0} \tag{2-25}$$

where, θ is the static contact angle and D_c is the critical cavity size estimated from equation (2-2). All data with different contact angles could be correlated by equation (2-25) to within 60% error.

A model describing the effect of wettability on nucleation site density was also proposed by Wang and Dhir (Wang and Dhir 1993b). From a Helmholtz free energy analysis, a criterion for gas/vapor entrapment conditions in a uniform temperature field was developed,

$$\theta > \varphi_{\min} \tag{2-26}$$

where, θ is the static contact angle and φ_{min} is the minimum cavity side angle of a spherical, conical, or sinusoidal cavity. The required wall superheat was found not only to be a function of the cavity mouth size, but also a function of the cavity geometry,

$$\Delta T_w = \frac{4\sigma T_{sat}}{\rho_v h_{fg} D_c} K \tag{2-27}$$

in which, K is a parameter accounting for the cavity geometry. The proposed model for the active nucleation site density was expressed as,

$$N_a = P_{as} \cdot N_{as} \tag{2-28}$$

in which, N_{as} is the heating surface cumulative cavity density with cavity mouth side angle less than a specified reference value. P_{as} is a dimensionless parameter which is a function of contact angle and the specified reference value. The model was validated in comparison with water pool boiling experimental data with contact angles of 18^o, 35^o and 90^o, surface cavity sizes ranging from 2 to 20 μm.

Following the same technique used by Wang and Dhir (Wang and Dhir 1993a), Basu et al. (Basu et al. 2002) conducted the subcooled flow boiling experiments with water at atmospheric pressure on a flat copper surface and a nine-rod zircalloy-4 bundle, respectively. The static contact angle changed with surface oxidization levels. The active nucleation site density was found to be a function of both the static contact angle and the wall superheat,

$$N_a\left(sites/cm^2\right) = 0.34\left(1-\cos\theta\right)\Delta T_w{}^{2.0} \tag{2-29}$$

when $\Delta T_{w,ONB} < \Delta T_w < 15^o C$

and,

$$N_a\left(sites/cm^2\right) = 3.4\times 10^{-5}\left(1-\cos\theta\right)\Delta T_w{}^{5.3} \tag{2-30}$$

when $\Delta T_w \geq 15^o C$

in which, $\Delta T_{w,ONB}$ is the wall superheat corresponding the onset of nucleate boiling. Most of the experimental data with contact angles ranging from 30^o to 90^o were fit by the correlation to within 40% error. The correlation is valid over a wide range of flow boiling conditions:

186~886 kg/m^{2}s of mass flux, 2.8~26.5 of wall superheat, and 1~230 sites/cm^2 of nucleation site density.

Benjamin and Balakrishnan (Benjamin and Balakrishnan 1997) conducted experimental work to investigate nucleation site density in pool boiling with saturated pure liquid at low-to-moderate heat fluxes. Pool boiling on stainless steel and aluminum surfaces with different surface polishing levels was examined with combinations of several kinds of fluids, including distilled water, carbon tetrachloride, n-hexane, and acetone. It was found that the nucleation site density depended on: the surface micro-roughness, liquid surface tension, thermal/physical properties of heating surface and liquid, and the wall superheat. A correlation based on the wall superheat, ΔT_w, Prandtl number, Pr, a surface-liquid interaction parameter, γ, and a dimensionless surface roughness parameter, θ, was proposed,

$$N_a = 218.8\,\mathrm{Pr}^{1.63}\left(\frac{1}{\gamma}\right)\theta^{-0.4}\Delta T_w{}^3; \tag{2-31}$$

Prandtl number is defined as,

$$\mathrm{Pr} = \frac{C_{p,l}\mu_l}{k_l}; \tag{2-32}$$

the surface-liquid interaction parameter, γ, is defined as,

$$\gamma = \left(\frac{k_w\rho_w C_{p,w}}{k_l\rho_l C_{p,l}}\right)^{1/2}; \tag{2-33}$$

the dimensionless surface roughness, θ, is defined as,

$$\theta = 14.5 - 4.5\left(\frac{R_a P}{\sigma}\right) + 0.4\left(\frac{R_a P}{\sigma}\right)^2; \tag{2-34}$$

where, $C_{p,l}$, μ_l, k_l, ρ_l, and σ are: liquid specific heat, viscosity, thermal conductivity, density and surface tension, respectively. $C_{p,w}$, k_w, and ρ_w are: wall material specific heat, thermal conductivity and density, respectively, and P is the pressure.

Experiments of forced convection boiling were conducted by Zeng and Klausner (Zeng and Klausner 1993) to study the nucleation site density in forced convection boiling.

Refrigerant R113 was boiled on a horizontal 25 by 25 mm square transparent test section heated with nichrome wires. The nucleation site number density was optically measured by a Videk Megaplus CCD camera. Due to the difficulty of observation from a view normal to the heating surface, side view images were obtained. To study effects of different system parameters, the nucleation site number density was plotted against wall heat flux, mass flux, mean vapor velocity and liquid velocity, respectively. It was found that the mean vapor velocity, heat flux and system pressure have strong influences on the nucleation site number density. The experimental results also showed that the critical cavity radius, which normally has been used to predict the number density of nucleation sites in pool boiling, was an important but insufficient correlating parameter for flow boiling nucleation site number density. A question was raised by the author: what is the physical basis for the strong influence of the mean vapor velocity and the wall heat flux. A possible solution for this was also proposed that the mean vapor velocity could be a controlling parameter on the interfacial shear stress, and consequently on the bulk turbulence and boiling heat flux.

Gaertner (Gaertner 1963) experimentally examined the spatial distribution of boiling nucleation sites on a copper surface. In the experiment, water containing dissolved nickel salts was boiled with heat fluxes of 200,000; 294,000; and 317,000 BTU/hr-ft^2. By dividing the macro area into smaller regions, it was found that the distribution of the nucleation sites number, N, in each of the smaller regions was fitted well by a spatial Poisson distribution. Based on the observation that the distribution of nucleation sites satisfies the spatial Poisson distribution, it was also found that the probability of distances of nearest-neighbor nucleation sites falls between S and $S+dS$ is,

$$P(S) = 2\pi \overline{N} S e^{-\pi \overline{N} S^2} dS \tag{2-35}$$

where, $\overline{N}$ is the area-averaged nucleation sites number. It was also found that the average distance between nearest-neighbor sites is,

$$\overline{S} = \frac{1}{2} \overline{N}^{1/2} \tag{2-36}$$

The active nucleation site density in subcooled flow boiling of water at high heat flux at atmospheric pressure was examined by Del Valle M and Kenning (Del Valle M and Kenning 1985). The positions of active nucleation sites were recorded by photography at different levels of heat flux, such as 70%, 80%, 90% and 95% of critical heat flux. In general, they found nucleation site density increases with heat flux from their experimental observations. It was also found that some of the sites were deactivated at higher heat fluxex while re-activated at even higher heat fluxes. A very small number of bubbles were found to slide on the heating surface and most of them grew and collapsed at their original nucleation sites. By counting the number of nucleation sites in sub-domains, the nucleation sites were found to fit the spatial Poisson distribution very well. The authors also examined the distribution of nearest-neighbor distances. Differences between experimental observations and theoretical spatial Poisson distribution were noticed. It was found that the experimentally observed nearest-neighbor distances did not fall between zero and a certain minimum value. A cut-off Poisson distribution was then proposed by the authors. The cut-off distance was found to be about twice the maximum bubble radius. A possible reason was suggested by the authors that at high heat fluxes the formation of a bubble was inhibited by adjacent ones.

2.2 BUBBLE DYNAMICS

During a boiling process, energy from the heating surface is first transferred to superheated liquid layer adjacent to the wall, and the majority of the energy is then transferred to bubbles in the form of latent heat. The remaining energy is transferred to the bulk flow through single phase convection. Bubbles play an important role during the boiling process since, (1) size and number of bubbles directly determine the amount of latent heat transferred by bubbles, and (2) single phase forced convection is greatly enhanced by bubble motion through departure and lift-off. In this section, some fundamental bubble dynamics knowledge is presented from review of the literature.

Rayleigh (Rayleigh 1917) first derived the equation of motion for the radius of a bubble, R, in a non-viscous, incompressible liquid as a function of time,

$$R\ddot{R} + \frac{3}{2}\dot{R}^2 = \frac{P_v - P_\infty}{\rho_l} \tag{2-37}$$

Where: P_v and P_∞ are vapor pressure and liquid pressure in a far field, respectively, and ρ_l is the liquid density. An over dot denotes the differentiation with respect to time.

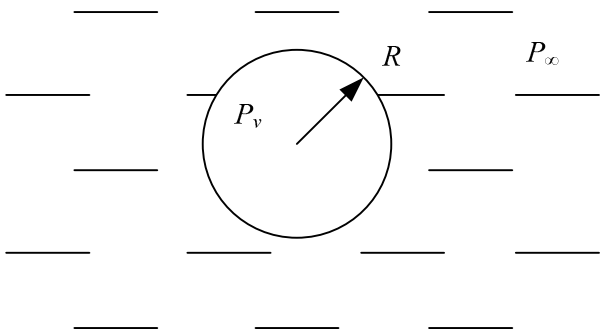

Figure 2.3, Bubble growth in incompressible liquid

A surface tension term was later added by Plesset and Zwick (Plesset and Zwick 1954) as,

$$R\ddot{R} + \frac{3}{2}\dot{R}^2 = \frac{P_v - P_\infty}{\rho_l} - \frac{2\sigma}{\rho_l R} \tag{2-38}$$

An asymptotic solution for the bubble growth was given by Plesset and Zwick (Plesset and Zwick 1952, 1954),

$$\frac{dR}{dt} = \frac{1}{2}\left(\frac{12\alpha_l}{\pi t}\right)^{1/2} \frac{\rho_l c_{p,l}\left(T_\infty - T_{sat}\right)}{\rho_v h_{fg}} \tag{2-39}$$

Zuber (Zuber 1961) extended the bubble growth theory of Bosnjakovic and Jakob to include the effect of a non-uniform temperature field, and gave the bubble radius as,

$$R(t) = \frac{2b}{\sqrt{\pi}} Ja\sqrt{\alpha_l t} \tag{2-40}$$

where: b is a constant, and Ja is the Jacob number, defined as,

$$Ja = \frac{\rho_l c_{p,l}\left(T_w - T_s\right)}{\rho_v h_{fg}} \tag{2-41}$$

By comparing with the experimental data, the author suggested that the value of the constant b is from 1 to √3.

Mikic et al. (Mikic et al. 1970) later derived a closed form for bubble growth in both inertia controlled and diffusion controlled stages,

$$\frac{1}{A^2}\left(\frac{dR}{dt}\right)^2 + \frac{2\sqrt{t}}{B}\frac{dR}{dt} - 1 = 0 \tag{2-42}$$

where, constants A and B are defined as,

$$A = \left(b\frac{\Delta T h_{fg}\rho_v}{T_{sat}\rho_l}\right)^{1/2} \tag{2-43}$$

and,

$$B = \left(\frac{12}{\pi}Ja^2\alpha_l\right)^{1/2} \tag{2-44}$$

where,

$b = \frac{2}{3}$ for bubble growth in an infinite medium, and,

$b = \frac{\pi}{7}$ for bubble growth on a surface.

The non-dimensional bubble radius solution was given as,

$$R^+ = \frac{2}{3}\left[\left(t^+ + 1\right)^{\frac{3}{2}} - \left(t^+\right)^{\frac{3}{2}} - 1\right] \tag{2-45}$$

in which, the non-dimensional bubble radius and time are given by,

$$R^+ = \frac{R}{B^2 / A} \tag{2-46}$$

and,

$$t^+ = \frac{t}{B^2 / A^2} \tag{2-47}$$

It should be noted that, as $t^+ << 1$, the Mikic's solution simplifies to Rayleigh's solution; and as $t^+ >> 1$, it simplifies to Zuber's solution.

A numerical analysis was carried out by Mei et al. (Mei et al. 1995a) to study bubble growth in saturated heterogeneous boiling. In their model, energy is transferred from the heating surface to a superheated liquid microlayer beneath a growing bubble. Evaporation continuously takes place on the liquid-vapor interface to maintain the bubble growth. Partial difference equations were constructed based on this concept, and finite difference solutions were obtained for the bubble growth rate and for temperature fields in the microlayer and the heater. The parameters characterizing the bubble shape and microlayer wedge angle were determined by matching with experimental data. The predicted bubble growth rate showed good agreement with experimental data over a wide range of conditions. In a subsequent study by Mei et al. (Mei et al. 1995b), a systematic investigation of the dependence of the bubble growth rate and the thermal field of the microlayer and heater on four dimensionless governing parameters, i.e. Jacob number, Fourier number, thermal conductivity ratio, and thermal diffusivity ratio of liquid to solid, was conducted.

In pool boiling, bubble departure diameter refers to bubble diameter when a bubble leaves from the heating surface. While in flow boiling, bubble behavior is more complicated. It's normally observed that a bubble leaves the original nucleation site and then starts to slide on the heating surface as it reaches a certain size, which is referred as the departure diameter in flow boiling. The sliding bubble continues to grow by taking energy from the heating surface, and it eventually leaves the heating surface entering the bulk flow at a certain size, which is referred as the lift-off diameter in flow boiling. Thus, the bubble frequency is closely related to the bubble departure diameter, bubble growth rate and waiting time.

The bubble departure size has been studied experimentally and in analytically work. A correlation was proposed by Cole (Cole 1960) to relate the bubble frequency and departure diameter for water pool boiling,

$$f^2 D_d = \frac{4g(\rho_l - \rho_v)}{3C_d \rho_l} \tag{2-48}$$

where, f is the bubble frequency, and D_d is the bubble departure diameter. The coefficient C_d is a bubble drag coefficient, which is equal to 1 for water.

A correlation was later proposed by Cole and Shulman (Cole and Shulman 1966) to relate the bubble departure diameter with pressure,

$$Bo^{1/2} = \frac{1000}{P} \tag{2-49}$$

where, P is pressure in mmHg, and the Bond number, Bo, is defined as,

$$Bo = \frac{g(\rho_l - \rho_v)(2R_d)^2}{\sigma} \tag{2-50}$$

where, R_d is the bubble departure radius.

In a subsequent study, Cole (Cole 1967) proposed that,

$$Bo^{1/2} = 0.04Ja \tag{2-51}$$

where, Ja is the Jacob number, defined in equation (2-41).

An improved correlation was proposed by Cole and Rohsenow (Cole and Rohsenow 1968),

$$Bo^{1/2} = CJa_c^{5/4} \tag{2-52}$$

in which, constant $C = 1.5\times10^{-4}$ for water, and $C = 4.65\times10^{-4}$ for liquids other than water. The Jacob number, Ja_c, was modified by replacing wall temperature with critical temperature.

Klausner et al. (Klausner et al. 1993) proposed a model to predict bubble departure diameter in forced convection boiling on a horizontal heating surface. Bubble departure from its original nucleation site, sliding on heating surface and then lift-off were experimentally observed. The departure diameter was found not to be a constant value, but followed closely to a Gaussian distribution. Klausner's model later was improved by Zeng et al. (Zeng et al. 1993) for the prediction of bubble departure diameters in both pool and flow boiling on horizontal heating surfaces. In pool boiling, the bubble departure diameter is determined by a force balance in the y-direction (i.e., normal to the heating surface), as shown in Figure 2.4,

$$\sum F_y = F_{sy} + F_{duy} + F_b + F_{cp} + F_L = 0 \tag{2-53}$$

where, F_{sy} is the surface tension force; F_{duy} is the unsteady growth force; F_b is the buoyancy force; F_{cp} is the contact pressure force; and F_L is the lift force created by the wake of a preceding departed vapor bubble.

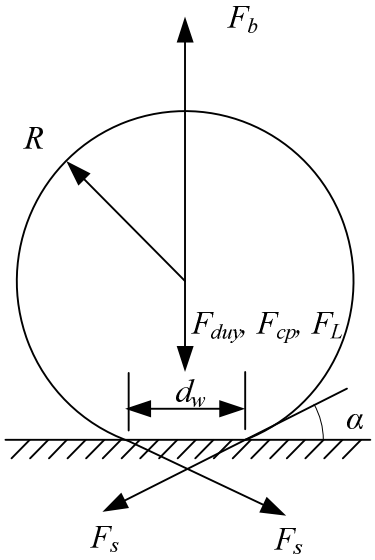

Figure 2.4, Bubble departure in pool boiling

The surface tension force in the y-direction is given by,

$$F_{sy} = F_s \sin\alpha = -\pi d_w \sigma \sin\alpha \tag{2-54}$$

where, d_w, σ, and α are contact diameter, surface tension and contact angle, respectively.

The unsteady growth force in the y-direction is given by,

$$F_{duy} = -\rho_l \pi R^2 \left(\frac{3}{2} C_s \dot{R}^2 + R\ddot{R} \right) \tag{2-55}$$

where, R is the bubble radius, and an over-dot denotes the differentiation with respect to time. As suggested by the authors, the bubble radius normally follows a power law with time and can be experimentally determined. Mikic's (Mikic et al. 1970) or Zuber's (Zuber 1961) model was suggested by the authors, if experimental data on bubble size were not available.

The buoyancy force is given by,

$$F_b = V_b(\rho_l - \rho_v)g = \frac{4}{3}\pi R^3(\rho_l - \rho_v)g \tag{2-56}$$

in which, V_b is the bubble volume, and g is the gravitational acceleration.

The contact pressure force is given by,

$$F_{cp} = \frac{\pi d_w^{\,2}}{4}\frac{2\sigma}{r_r} \tag{2-57}$$

in which, r_r is the radius of curvature at the base of the bubble. It's suggested that since $d_w/r_r << 1$ and therefore the contact pressure force can be neglected.

The lift force due to a preceding departed vapor bubble in pool boiling is roughly estimated as,

$$\frac{F_L}{\rho_l \dot{R}^2 R^2} \sim 2.86\times10^{-4} \tag{2-58}$$

As suggested by Zeng et al., this term can be neglected for most cases of practical interest.

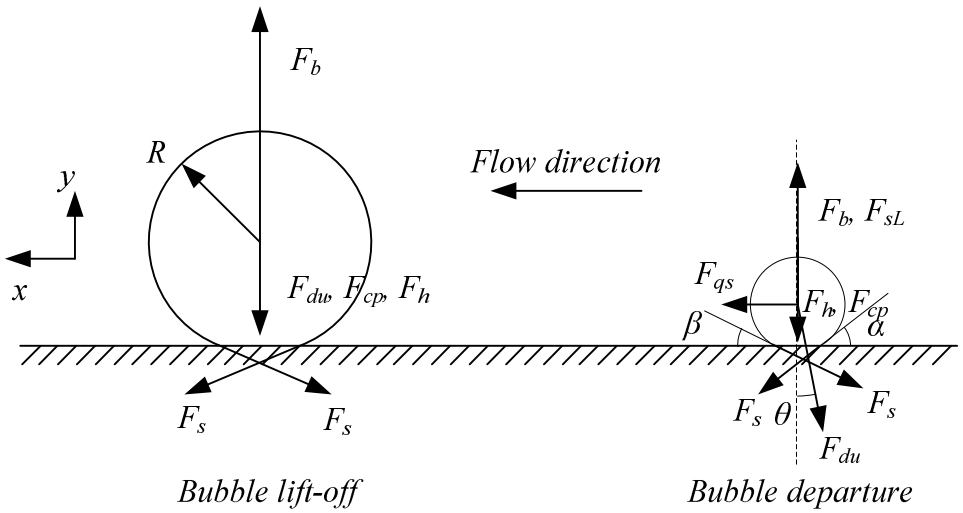

Figure 2.5, Bubble departure and lift-off in flow boiling.

In flow boiling, bubble departure size is determined by a force balance in both the x-direction (i.e., flow direction, parallel to the heating surface) and the y-direction (i.e., normal to the heating surface),

$$\sum F_x = F_{sx} + F_{qs} + F_{du}\sin\theta = 0 \tag{2-59}$$

$$\sum F_y = F_{sy} + F_{sL} + F_b + F_h + F_{cp} + F_{du}\cos\theta = 0 \tag{2-60}$$

in which, F_{sx} is the surface tension force component in the flow direction; F_{qs} is the quasi-steady drag force in the flow direction; $F_{du}sin\theta$ is the grow force component in the flow direction; F_{sy} is the surface tension component in the y-direction; F_{sL} is the shear lift force; F_b is the buoyancy force; F_h is the hydrodynamic force; F_{cp} is the contract pressure force; $F_{du}cos\theta$ is the unsteady growth force component in the y-direction; θ is the angle of inclination.

Surface tension terms are given by Klausner et al. (Klausner et al. 1993) as,

$$F_{sx} = -1.25 d_w \sigma \frac{\pi(\alpha - \beta)}{\pi^2 - (\alpha - \beta)^2} \tag{2-61}$$

and,

$$F_{sy} = -d_w \sigma \frac{\pi}{\alpha - \beta}\left[\cos\beta - \cos\alpha\right] \tag{2-62}$$

where, α and β are advancing contact angle and receding contact angle, respectively.

The quasi-steady drag force is given by,

$$F_{qs} = 6\pi\rho_l \Delta v R\left\{\frac{2}{3} + \left[\left(\frac{12}{\mathrm{Re}_b}\right)^n + 0.796^n\right]^{-1/n}\right\} \tag{2-63}$$

where, Δv is the velocity difference between the vapor bubble and the surrounding liquid; R is the bubble radius and Re_b is the bubble Reynolds number, which is defined as,

$$\mathrm{Re}_b = \frac{2\rho_l \Delta v R}{\mu_l} \tag{2-64}$$

The constant, n, is normally taken as 0.65.

The shear lift force is given by,

$$F_{sL} = \frac{1}{2}\rho_l \Delta v^2 \pi R^2 \left\{3.877 G_s^{1/2}\left[\mathrm{Re}_b^{\,2} + 0.014 G_s^{\,2}\right]^{1/4}\right\} \tag{2-65}$$

where,

$$G_s = \left|\frac{dv}{dy}\right| \frac{R}{\Delta v} \tag{2-66}$$

and y is the distance from the wall.

The hydrodynamic pressure force is given by,

$$F_h = \frac{9}{8}\rho_l \Delta v^2 \frac{\pi d_w^{\,2}}{4} \tag{2-67}$$

The unsteady growth force, F_{du}, buoyancy force, F_b, and contact pressure force, F_{cp}, are defined in equations (2-55), (2-56), and (2-57), respectively.

After bubble departure from its original site, it's assumed that the bubble slides with at the same velocity as the surrounding fluid, and therefore, both the velocity difference and angle of inclination are zero. The bubble lift-off size can be determined simply by the force balance in the y-direction,

$$\sum F_y = F_s + F_b + F_h + F_{cp} + F_{du} = 0 \tag{2-68}$$

Klausner (Klausner et al. 1993) and Zeng's (Zeng and Klausner 1993) models are so far the only mechanistic models based on analytical bubble force analysis, and they give fairly good agreement with experimental data.

In flow boiling processes, other than single bubble dynamics, multiple bubble dynamics is even more important. Many observations have shown that significant bubble interactions, such as bubble coalescence, nucleation site prohibition/activation are present in flow boiling. These strong interactions make flow boiling a highly nonlinear system. A review of boiling chaos has been provided by Shoji (Shoji 2004). At moderate heat flux, a sliding vapor bubble can coalesce with another bubble downstream to form a larger bubble. Experimental evidence shows that this larger bubble has a high chance to lift-off from the heating surface even it does not reach a normal lift-off size. At higher heat fluxes, nucleation site density is so high that the distance between two adjacent bubbles is about one bubble diameter. Then bubble coalescence can happen directly at their original sites without sliding. However, as the nearest distance between two bubbles becomes close to one bubble diameter, prohibiting bubble formation due to adjacent bubbles and it has been experimental observed in pool boiling. Little data were obtained for flow boiling bubble prohibition, but the mechanism may be applied for these conditions. This needs to be confirmed.

An experiment was carried out by Chekanov (Chekanov 1977) to study growth of bubbles on a heating surface and bubble recurrence rates. Based on experimental data, it was found that the greatest effect on bubble formations from adjacent bubbles was in the form of acoustic waves emitted by the growing bubble. This effect of was studied in terms of time intervals between bubble formation at one site and that at an adjacent site. The distribution of this time interval can be described by the theory of pulse processes,

$$g(\tau) = \left[\lambda^{\nu}\tau^{\nu-1}/\Gamma(\nu)\right]e^{-\lambda\nu} \tag{2-69}$$

where, g is the probability that the time interval is within τ and $\tau+d\tau$; λ is the reciprocal of the expected value of the time interval; v is a correlation parameter. Experimental results were obtained for both saturation and subcooled boiling of water at atmospheric pressure. The ratio of the distance between the two sites, r, to the bubble maximum diameter, D, was studied. Experimental results showed that, when this distance was larger than three times the maximum bubble diameter, the correlation parameter $v < 1$. This means the formation of a bubble on one nucleation site promotes that on the other site. When this distance $r \sim< 3D$, the correlation parameter $v > 1$, which indicates that the formation of a bubble on one nucleation site inhibits that on the other site. When the distance is much larger than the bubble diameter, the correlation parameter v is close to 1 and there is no interaction between them. It was also proposed by the author that, the first heat transfer crisis during boiling heat transfer occurred when the distance between nucleation sites was equal to the correlation radius, which is about three times the maximum bubble diameter.

Theoretical analyses and experiments were conducted by Chai et al. (Chai et al. 2000) to analyze the interactions between active sites/bubbles. For nucleate boiling, the formation of a bubble on a nucleation site was idealized as a round continuous surface heat sink. The temperature variation induced by bubble growth was then analytically solved. The results showed that bubble size and heating surface material significantly influenced the temperature field inside the heating surface. This phenomenon was also experimentally explored in pool boiling on metal plates with various materials and thicknesses. Temperatures on several

adjacent sites were recorded by thermocouples. Different levels of thermal influence were found for different surface material and thickness combinations. It was experimentally found that, the thinner the plate and the smaller the plate thermal conductivity, the stronger were the observed thermal interactions. Both analytical and experimental work showed thermal conductivity played a critical role during thermal interactions. The study made by the author revealed a more reasonable mechanistic description of nucleate boiling than the classical linear approach. The classical linear approach is normally based on analysis of single bubble dynamics, nucleation site density and an assumed uniform wall superheat. A theoretical framework was then proposed by Chai (Chai 2004) to analyze interactions between bubbles and their self-organizing effect. Due to the difficulty of applying classical nonlinear partial differential equations to describe boiling systems, statistical mechanics, based on Lagrange's optimization, was used as an alternative method. This proposed method, although preliminary, provided a renewed theoretical effort to understand the underlying mechanisms of nucleate boiling.

It was observed by Judd and Lavdas (Judd and Lavdas 1980) that, bubble emission on a nucleation site was capable of either activating or deactivating the bubble emission on an adjacent nucleation site. A potential nucleation site can be activated when it's covered by a bubble formed on an adjacent site, while bubble formation can also be prohibited due to the growth of an adjacent bubble. The influence area, sometimes referred asthe energy extraction area of a bubble, was also studied. This area is normally expressed as K times the projected area of a bubble. The value of K was found to be sensitive to interactions between nucleation sites. When overlapping of bubbles is intensive the value of K approaches unity. By using the same theory of pulse processes adopted by Chekanov (Chekanov 1977), interactions between nucleation sites were experimentally studied by Calka and Judd (Calka and Judd 1985). The probability distribution function of elapsed time between bubble formations on two adjacent sites was plotted and fitted with a Gamma function. Compared to Chekanov's results, an opposite conclusion was drawn based on the analysis of experimental results. It was found that promotion of a bubble on an adjacent site occurred when $1/2 \leq S/D \leq 1$, where S is the

distance between two sites and D is the maximum bubble diameter. The author believed it was the result of a 'seeding' mechanism. Sites interaction behavior under different boiling conditions, such as bubble number density and bubble diameter, were also experimentally revealed by Judd and Chopra (Judd and Chopra 1993). Based on Judd's (Judd 1988) site-seeding concept, a simulation routine known as BOILSIM was developed by Mallozzi et al. (Mallozzi et al. 2000) to simulate the interaction process of nucleation sites. Good agreement was obtained compared with Chopra's experimental data (Judd and Chopra 1993).

An experiment was designed to statistically study the interaction between nucleation sites by Hardenberg et al. (Hardenberg et al. 2004). Spatial-temporal data of wall temperatures were obtained by liquid crystal thermography over a period of 1,930 seconds, during pool boiling of water. The experiment was conducted on a thin plate with non-uniformly distributed nucleation sites at a heat flux at 51 kW/m^2. Without the need of direct visual observation of bubbles, the phenomenon of nucleation sites interactions was identified from analysis of the spatial-temporal data of wall temperatures. The number of subsequent events, i.e., bubble formations on other sites during different delayed time intervals was plotted as a function of distance from the original site. It was found that there were no interactions for $S/R > 0.75$, while inhibitions occurred for $S/R < 0.25$, and promotion occurred for S/R values between 0.25 and 0.75, where S is the distance between two sites, and R is the bubble radius.

Surfaces with twin artificial nucleation sites were utilized to study nucleation sites interactions in pool boiling by Mosdof and Shoji (Mosdof and Shoji 2004). Temperatures of nucleation sites were recorded and a nonlinearity analysis was performed. It was found that thermal interactions between two sites decreased while hydrodynamic interactions increased bubble emission frequency. The nonlinearity analysis showed that, at around $S/D = 0.5$ and 2.5, interactions through the liquid, i.e. bubble coalescence and hydrodynamic interactions, promoted bubble departure. At around $S/D = 1.75$, thermal interactions inhibited bubble departure. The nonlinearity analysis on twin and triple artificial nucleation sites, which are activated by a laser, were presented by Mosdorf and Shoji (Mosdof and Shoji 2008).

Interactions between lasers activated nucleation sites were also experimentally studied by Golobič and Gjerkeš (Golobič and Gjerkeš 2001). In their study, interactions between two, three, and four simultaneously activated sites in various geometrical arrangements in pool boiling with saturated water were studied. In this kind of study, "natural occurrence" of boiling is sacrificed to some extent. However, it provides a chance to manually control parameters and direct observations can be made. For two laser activated sites with identical diameters and heat fluxes, the interaction did not occur until the distance between these two sites was in the order of one bubble size. These interactions occurred in the form of: (1) decreased frequencies on both sites, (2) one decreasing and the other increasing, or (3) irrespective of each other. Similar behaviors were also found for the interactions of three or four this kind of sites. It was also found in certain extreme cases with two sites that one site could completely deactivate the other. The heat transfer capability of these sites was studied in terms of latent heat carried by lift-off bubbles. However, it is known during boiling processes micro convection induced by bubble movement is an important contribution to boiling heat transfer. Therefore, the results provided in this study might be insufficient since the latent heat flux is not enough to account for the whole boiling process.

The behavior of near-wall bubbles in subcooled flow boiling has been visually investigated for water flow boiling in vertical, one-side heated, rectangular channels at atmospheric pressure by Chang et al. (Chang et al. 2002). A Kodak Ektapro 100 motion analyzer and a Nikon D1 digital camera were used to record bubble behaviors during subcooled flow boiling. It was observed that significant bubble coalescence was present for heat fluxes over ~40% of CHF (critical heat flux). At sufficiently high heat fluxes, three characteristic regions were identified, including, (1) a superheated liquid layer with very small bubbles attached on heated surfaces, (2) a flowing bubble layer containing vapor clots and small bubbles, and (3) a liquid core region. It was also visually confirmed that a liquid sublayer existed beneath coalesced bubbles, and that CHF occurred during the process of periodic formations of large vapor clots near the exit. As claimed by the author, these observations provided visual evidence for the liquid sublayer dryout critical heat flux models.

A digital photographic study of subcooled flow boiling with R134a was performed in a vertical rectangular channel by Bang et al. (Bang et al. 2004). In their study, a detailed observation of near wall bubble structure was obtained. The near wall regions included a vapor remnant, an interleaved liquid layer, and coalesced bubbles. It was also shown that critical heat fluxes were trigged by dryout of the near wall bubble layer beneath the vapor clots.

Bubble growth and condensation behaviors were experimentally investigated by Prodanovic et al. (Prodanovic et al. 2002) for subcooled flow boiling of water at pressures from 1.05 to 3 bar and bulk liquid velocities from 0.08 to 0.8 m/s. A high speed camera with 6000-8000 frames per second was used to capture bubble dynamics from the inception to final collapse. The bubble dynamics were found to vary in different boiling regimes: (1) A regime before ONB, with low heat flux and nucleation site density, where bubble detachment is rarely observed; (2) An isolated bubble regime, where bubbles detach from surfaces without much interactions with adjacent bubbles; (3) A regime with significant bubble coalescence, where bubble number density is very high and bubble coalescence occurs before bubble detachment. Aside from normal detachment, bubbles detach after merging or interacting with adjacent bubbles. An empirical correlation was proposed to correlate bubble size during growth and condensation against time based on experimental results.

2.3 HEAT FLUX PREDICTION

Flow boiling heat transfer has proved to be an efficient way of cooling in high heat flux removal applications, such as heat removal in nuclear reactor cores. Much work has been done to understand and to model flow boiling heat transfer. During the past decades, numerous empirical correlations were proposed to predict the boiling heat transfer rate. However, these correlations were normally limited to a certain range of applicability. In addition to empirical correlations, approaches were also made to build mechanism based models to explain and predict complex flow boiling phenomena.

Some of the empirical correlations were proposed at early years, such as by McAdams, Jens and Lottes, and Shah.

McAdams et al. (McAdams et al. 1949) first proposed a correlation for water flow boiling heat transfer as,

$$q = C\Delta T_s^{3.86} \tag{2-70}$$

in which, the constant, C, depends on the dissolved air content and is determined empirically.

Jens and Lottes (Jens and Lottes 1951) gave a correlation to relate wall superheat and system pressure to heat flux for water flow boiling,

$$\Delta T_s = 25q^{0.25}e^{-P/62} \tag{2-71}$$

in which, the wall heat flux, q'', is in MW/m^2 and pressure, P, is in bar.

Jens and Lottes' correlation was later improved by Thom et al. (Thom et al. 1965) to fit experimental data,

$$\Delta T_s = 25q^{0.6}e^{-P/87} \tag{2-72}$$

Thom's correlation is for subcooled or saturated flow boiling of water at pressure up to 200 bars under conditions where the nucleate boiling contribution is predominant over forced convection.

Wall heat flux during flow boiling is also normally expressed as a sum of two components, contribution from single phase convection heat transfer and contribution from boiling heat transfer,

$$q = q_{sp} + q_{bi} \tag{2-73}$$

in which, q_{sp} is the heat flux component from single phase convection, and q_{bi} is the component from boiling heat transfer.

Bowring (Bowring 1962) was the first one to identify different heat transfer mechanisms during flow boiling. It's proposed that wall heat flux, q, during flow boiling has three components, single phase convection, q_{sp}, evaporation, q_{ev}, and sensible heating of the bulk liquid filling the void created by departure of vapor bubble, q_{pump}. Thus,

$$q = q_{sp} + q_{ev} + q_{pump} = q_{sp} + (1+\varepsilon) q_{ev} \tag{2-74}$$

in which, $\varepsilon = q_{pump}/ q_{ev}$ is normally empirically determined. Single phase convection heat transfer can be estimated by,

$$q_{sp} = h_{sp}\left(T_w - T_{bulk}\right) \tag{2-75}$$

The evaporation term can be calculated by multiplying the latent heat carried by a single bubble, the bubble frequency and the active nucleation site density,

$$q_{ev} = \rho_v h_{fg} V_b f N_a \tag{2-76}$$

in which, V_b is the volume of a bubble; f is the bubble frequency and N_a is the active nucleation site density.

The ratio ε is empirically given by,

$$\varepsilon = \begin{cases} 1 + 3.2\dfrac{\rho_l c_{p,l} \Delta T_{sub}}{\rho_v h_{fg}} & 1 \le p \le 9.5 \\ 2.3 & 9.5 \le p \le 50 \\ 2.6 & p > 50 \end{cases} \tag{2-77}$$

in which, p is pressure in bar. Bowring's correlation has been verified in a wide range of flow boiling conditions, with pressures ranging from 11 to 136 bars, heat fluxes ranging from 30 to 160 W/cm^2 and liquid velocities ranging from 0.8 to 2.0 m/s.

Chen (Chen 1966) proposed a correlation to predict saturated flow boiling heat flux of water, and was also extended to subcooled flow boiling. For saturated water flow boiling,

$$q = h_{bi}\left(T_w - T_s\right) \tag{2-78}$$

$$h_{bi} = h_{FC} + h_{NB} \tag{2-79}$$

where,

$$h_{FC} = 0.023\left[\frac{G(1-x)D_h}{\mu_l}\right]^{0.8} \mathrm{Pr}_l^{\,0.4} \frac{k_l}{D_h} F \tag{2-80}$$

$$h_{NB} = 0.00122 \frac{k_l^{0.79} c_{p,l}^{0.45} \rho_l^{0.49} (T_w - T_s)^{0.24} (P_w - P_s)^{0.75}}{\sigma^{0.5} \mu_l^{0.29} h_{fg}^{0.24} \rho_v^{0.24}} S \tag{2-81}$$

where, the factor, F, is approximated by,

$$F = \begin{cases} 1, & if \ \frac{1}{X_{tt}} \le 0.1 \\ 2.35\left(\frac{1}{X_{tt}} + 0.213\right)^{0.736}, & if \ \frac{1}{X_{tt}} > 0.1 \end{cases} \tag{2-82}$$

the inverse Martinelli parameter is defined as,

$$\frac{1}{X_{tt}} = \left(\frac{x}{1-x}\right)^{0.9} \left(\frac{\mu_v}{\mu_l}\right)^{0.1} \left(\frac{\rho_l}{\rho_v}\right)^{0.5} \tag{2-83}$$

and, the suppression factor, S, is approximated by

$$S = \begin{cases} \frac{1}{1 + 0.12 \, \mathrm{Re}_{TP}^{1.14}}, & if \ \mathrm{Re}_{TP} \le 30 \\ \frac{1}{1 + 0.42 \, \mathrm{Re}_{TP}^{0.78}}, & if \ 30 < \mathrm{Re}_{TP} \le 70 \\ 0.1, & if \ \mathrm{Re}_{TP} > 70 \end{cases} \tag{2-84}$$

where,

$$\mathrm{Re}_{TP} = 10^{-4} \frac{G(1-x)D_h}{\mu_l} F^{1.25} \tag{2-85}$$

For subcooled flow boiling, equation (2-78) can be rewritten as,

$$q = h_{NB}(T_w - T_s) + h_{FC}(T_w - T_b) \tag{2-86}$$

in which, the nucleate boiling heat transfer coefficient, h_{NB}, can be calculated by equation (2-80). The suppression factor, S, can be calculated by equation (2-83) with a single phase Reynolds number. The single phase heat transfer coefficient, h_{FC}, can be calculated from equation (2-79) with factor F equal to 1.

A graphic alternative to Chen's correlation was proposed by Shah (Shah 1976) for saturated flow boiling. The ratio of the flow boiling heat transfer coefficient to the single

phase heat transfer coefficient, h_{TP}/h_{SP}, was plotted with the convection number, *Co*, the boiling number, *Bo*, and the Froude number, *Fr*. The convection number, *Co*, is defined as,

$$Co = \left(\frac{1-x}{x}\right)^{0.8}\left(\frac{\rho_v}{\rho_l}\right)^{0.5} \tag{2-87}$$

where, x is the mass vapor quality.

The boiling number, *Bo*, is defined as,

$$Bo = \frac{q}{Gh_{fg}} \tag{2-88}$$

The Froude number, *Fr*, is defined as,

$$Fr = \frac{G^2}{\rho_l g D} \tag{2-89}$$

Based on experimental data of water, refrigerants, alcohols etc., an empirical non-dimensional correlation was later proposed by Shah (Shah 1977) to predict subcooled flow boiling heat transfer in pipes and annuli. The correlation for fully developed flow boiling is given by,

$$\frac{h_{TP}}{h_{SP}} = f(Bo) \tag{2-90}$$

in which, *f(Bo)* is given by,

$$f(Bo) = \begin{cases} 230Bo^{C_1} & for\ Bo > 3.0\times10^{-5} \\ 1+46Bo^{C_1} & for\ Bo \le 3.0\times10^{-5} \end{cases} \tag{2-91}$$

A value of 0.5 is suggested by the author for the empirical constant, C_1. A similar study on saturated flow boiling is also provided by Shah (Shah 1982).

Kandlikar (Kandlikar 1990) proposed a general correlation for saturated two-phase flow boiling heat transfer inside horizontal and vertical tubes. Later, a flow boiling map for subcooled and saturated flow boiling of different fluids inside circular tubes was constructed by Kandlikar (Kandlikar 1991). A correlation for subcooled flow boiling was then proposed by Kandlikar (Kandlikar 1997, 1998). Correlations for saturated two-phase flow boiling heat

transfer were separately proposed for vertical and horizontal flows. A final form of the correlation for both conditions was then proposed as,

$$\frac{h_{TP}}{h_{lo}} = C_1 Co^{C_2} \left(25Fr_l\right)^{C_5} + C_3 Bo^{C_4} \left(25Fr_l\right)^{C_6} F_{fl} \tag{2-92}$$

where, constants, C_1, C_2, C_3, C_4, C_5 and C_6 were empirically determined. The convection number, Co, boiling number, Bo, and Froude number with all flow as liquid, Fr_l, could be calculated by equations (2-87), (2-88), and (2-89), respectively. F_{fl} is a constant depending on type of fluid. h_{lo} is the single phase convection heat transfer coefficient assuming all mass flow as liquid only.

The correlation for subcooled flow boiling was proposed as,

$$\frac{h_{TP}}{h_{lo}} = 1058.0 Bo^{0.7} F_{fl} \tag{2-93}$$

and,

$$q = h_{TP}\left(T_w - T_s\right) \tag{2-94}$$

where, h_{SP} is the single phase convection heat transfer coefficient, calculated from,

$$Nu_{lo} = Nu_{lo,cp}\left(\frac{\mu_b}{\mu_w}\right) \tag{2-95}$$

where, μ_b and μ_w are fluid dynamic viscosities corresponding bulk temperature and wall temperature, respectively. The $Nu_{lo,cp}$ is the Nusselt number with constant properties, given by Petukhov and Popov (Petukhov and Popov 1963) for $0.5 \le Pr \le 2000$ and $10^4 \le Re_{lo} \le 5\times10^6$,

$$Nu_{lo} = \frac{\mathrm{Re}_{lo}\,\mathrm{Pr}\left(f/2\right)}{\left[1.07 + 12.7\left(\mathrm{Pr}^{2/3} - 1\right)\left(f/2\right)^{0.5}\right]} \tag{2-96}$$

and by Gnielinski (Gnielinski 1976) for $0.5 \le Pr \le 2000$ and $2300 \le Re_{lo} \le 5\times10^4$,

$$Nu_{lo} = \frac{\left(\mathrm{Re}_{lo} - 1000\right)\mathrm{Pr}\left(f/2\right)}{\left[1.07 + 12.7\left(\mathrm{Pr}^{2/3} - 1\right)\left(f/2\right)^{0.5}\right]} \tag{2-97}$$

where, f is the friction factor given by,

$$f = \left[1.58\ln\left(\mathrm{Re}_{lo}\right) - 3.28\right]^{-2} \tag{2-98}$$

Combining the definition of h_{TP}, and the boiling number, Bo, the final form for the subcooled flow boiling heat flux can be derived as,

$$q = \left[1058.0\left(Gh_{fg}\right)^{-0.7} F_{fl} h_{lo}\left(T_w - T_s\right)\right]^{1/0.3} \tag{2-99}$$

Liu and Winterton (Liu and Winterton 1989) proposed a general correlation for both saturated and subcooled flow boiling in tubes and annuli based on a nucleate pool boiling equation. The flow boiling flux is basically calculated from a single phase convection component and a nucleate pool boiling component as suggested by Kutateladze (Kutateladze 1961). The correction factors, F and S, are from an original idea that the single phase convection is enhanced while the boiling heat transfer is suppressed due to the presence of vapor bubbles. The flow boiling heat transfer correlation then is given by,

$$q_{saturated} = \sqrt{\left(Fh_{SP}\right)^2 + \left(Sh_{pool}\right)^2}\left(T_w - T_s\right) \tag{2-100}$$

and,

$$q_{subcooled} = \sqrt{\left[Fh_{SP}\left(T_w - T_b\right)\right]^2 + \left[Sh_{pool}\left(T_w - T_s\right)\right]^2} \tag{2-101}$$

where, the enhancement fact F and suppression factor S are given by,

$$F = \left[1 + x\,\mathrm{Pr}_l\left(\frac{\rho_l}{\rho_v} - 1\right)\right]^{0.35} \tag{2-102}$$

$$S = \left[1 + 0.055F^{0.1}\,\mathrm{Re}_l^{\,0.16}\right]^{-1} \tag{2-103}$$

where, x is the mass vapor quality. Pr_l and Re_l are the liquid Prandtl number and Reynolds number, respectively.

The single phase convection heat transfer coefficient is given by the Dittus-Boelter correlation (Dittus and Boelter 1930),

$$h_{SP} = 0.023\frac{k_l}{d}\mathrm{Re}_l^{\,0.8}\,\mathrm{Pr}_l^{\,0.4} \tag{2-104}$$

The pool boiling heat transfer coefficient is given by Cooper's correlation (Cooper 1984),

$$h_{pool} = 55 p_r^{0.12} q^{2/3} \left(-\log_{10} p_r\right)^{-0.55} M^{-0.5} \quad (2\text{-}105)$$

where, p_r is the reduced pressure, which is the ratio of the pressure to the critical pressure. M is the molecular weight.

In most of the modeling work on predicting heat transfer rate, the wall heat flux is calculated from different components, such as single phase convection, bubble latent heat contribution and transient conduction to bulk flow after bubble departure from heating surface. This includes work of Kenning and Del Valle M (Kenning and Del Valle M 1981), Del Valle M and Kenning (Del Valle M and Kenning 1985), Sateesh et al. (Sateesh et al. 2005), Basu et al. (Basu et al. 2005), Podowski and Podowski (Podowski and Podowski 2009).

Kenning and Del Valle M (Kenning and Del Valle M 1981) proposed a heat transfer model for fully developed nucleate pool boiling. For isolated pool boiling with small nucleation site density, the heat transfer rate can be expressed as the sum of two components, single phase convection and boiling components,

$$q = q_{bi} + q_c\left(1-\alpha\right) \quad (2\text{-}106)$$

where, q_{bi} is the contribution from boiling, q_c is the contribution from single phase convection and α is the nominal fraction of wall affected by boiling. The contribution from boiling can be estimated from so-called '*quenching theory*': the heating wall is cooled by the bulk liquid which fills the vacancy created by a departed bubble. The wall quenching can be modeled as transient conduction from the wall to a semi-infinite liquid. A time-averaged quenching flux is given by,

$$q_1 = 2\left(\frac{k_l \rho_l c_{p,l} f}{\pi}\right)^{1/2} \Delta T \quad (2\text{-}107)$$

in which, k_l, ρ_l and $c_{p,l}$ are liquid thermal conductivity, density and specific heat, respectively. f is the bubble frequency; ΔT is the temperature difference between the wall and the bulk liquid. The boiling component then can be calculated from,

$$q_{bi} = q_1 \alpha \quad (2\text{-}108)$$

and

$$\alpha = nKA = nK\left(\pi R_m{}^2\right) \tag{2-109}$$

where, n is the nucleation site density; A is the bubble projection area, which is a function of the maximum bubble radius, R_m. The parameter, K, is normally assumed as a constant in a range of $2 \le K \le 5$, which is experimentally determined. As heat flux increases, the nucleation site density can be very high, so that bubble affected areas can overlap and therefore a certain area can be quenched m times during an average bubble period, $1/f$. The total wall heat flux can be expressed as,

$$q = q_1 \alpha \sum_{m=1}^{\infty} \frac{q_m}{q_1} \frac{y_m}{m} + q_c \left(1 - \alpha \sum_{m=1}^{\infty} \frac{y_m}{m}\right) \tag{2-110}$$

where, y_m is the fraction of area of influence quenched by m sites; q_m is the time-averaged quenching flux for m sites. By assuming that adjacent sites have the same frequency and quenching events are randomly distributed, as given by,

$$\frac{q_m}{q_1} = \frac{2^{m-1} m!}{1 \cdot 3 \cdot \ldots \cdot (2m-3)(2m-1)} \tag{2-111}$$

Three types of nucleation sites distributions, e.g., regular triangular distribution, random distribution (spatial Poisson distribution) and modified random distribution (modified spatial Poisson distribution), were examined. Based on the calculated results, the author suggested that the effect of nucleation sites distribution was not significant, while correlations for bubble size and frequency could be critical for predicting the heat flux.

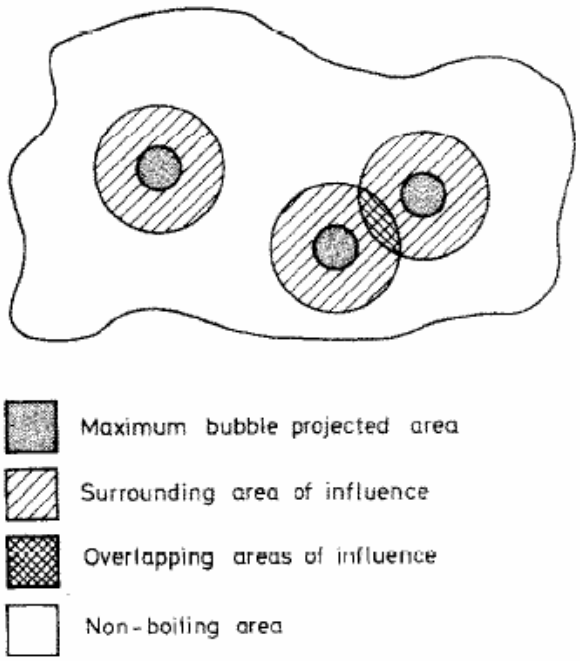

Figure 2.6. A schematic drawing of heat transfer zones in pool boiling (Del Valle M and Kenning 1985).

Del Valle M and Kenning (Del Valle M and Kenning 1985) then proposed a theoretical heat transfer model for subcooled flow boiling based on an experimental investigation of subcooled flow boiling of water at atmospheric pressure on stainless steel. In this experiment, bubble size, frequency and nucleation sites distribution were examined. In terms of heat transfer, the heated wall is divided into four zones as shown in Figure 2.6: (1) maximum bubble projected area, where microlayer evaporation and transient conduction dominate; (2) surrounding areas of influence, where transient conduction dominates; (3) overlapping areas of influence, where enhanced transient conduction dominates; and (4) non-boiling area, where single phase forced convection dominates. The only unspecified quantity in the theoretical model is the factor K, which is the ratio of the bubble influenced area to the bubble projected area. The value of K was adjusted to make the model calculated heat flux match the measured flux. Itwas found that the value of K varied from 5.8 to 7.5. The microlayer evaporation heat transfer was found to be only 2-3% of the total heat flux. Single phase convection accounted for around 10% and it decreased to 5% as the boiling area increased at higher heat flux. This model sheds some light on how to quantify flow boiling

heat transfer components, however, the sliding of bubbles was not considered in the model and an empirical parameter *K* was adjusted to match the model predicted heat flux and experimentally measured value.

Sateesh et al. (Sateesh et al. 2005) studied the effect of bubbles sliding on the heating surface on pool boiling heat transfer. The model considered different heat transfer mechanisms, than during pool boiling, involving bubble sliding, such as; latent heat transfer due to microlayer evaporation, transient conduction due to thermal boundary reformation, natural convection and heat transfer due to bubbles sliding. The latent heat transfer due to microlayer evaporation of a stationary bubble (i.e., before its sliding) is given by,

$$q_{me} = \left(\frac{1}{6} \pi {d_d}^3 \rho_v \right) h_{fg} N_a f \tag{2-112}$$

where: d_d is bubble departure diameter; N_a is active nucleation site density; and f is bubble frequency. The transient conduction heat transfer due to bubble departure from its original site is given by,

$$q_{tc} = 2\sqrt{\frac{k_l \rho_l c_{p,l}}{\pi t_w}} \Delta T \left(N_a K \frac{\pi {d_d}^2}{4} \right) t_w f \tag{2-113}$$

Where: t_w is the waiting time; K is the ratio of bubble influence area to its projected area; and a value of 1.8 is suggested. Some detailed work on the influence of sliding bubble on forced boiling heat transfer can be found in Yan et al. (Yan et al. 1997), Thorncroft and Klausner (Thorncroft and Klausner 1999), and Donnelly et al. (Donnelly et al. 2009). The microlayer evaporation due to a sliding bubble can be simply calculated as,

$$q_{mes} = \left[\frac{1}{6} \pi \left({d_l}^3 - {d_d}^3 \right) \rho_v \right] h_{fg} N_a f \tag{2-114}$$

where, d_l is the bubble lift-off diameter. The transient conduction heat transfer due to a sliding bubble is given by,

$$q_{tcs} = 2\sqrt{\frac{k_l \rho_l c_{p,l}}{\pi t_w}} \Delta T N_a t_w f \int_{t_d}^{t_l} K d(t) U_b(t) dt \tag{2-115}$$

where, t_d is the bubble departure time; t_l is the bubble lift-off time; $d(t)$ is the bubble diameter at time t; and $U_b(t)$ is the bubble velocity at time t. The area fraction of natural convection is determined by the area which is not influenced by either a stationary bubble or a sliding bubble, as given by,

$$A_{nc} = 1 - A_1 - A_2 - A_4 \tag{2-116}$$

where, A_1 is the stationary bubble influenced area, given by,

$$A_1 = \frac{3}{4} N_a K \frac{\pi d_d^{\,2}}{4} + \frac{1}{4} N_a \frac{\pi d_d^{\,2}}{4} \tag{2-117}$$

by assuming that the waiting time is three times the growth time.

A_2 is the sliding bubble projected area, given by,

$$A_2 = n_s \frac{\pi\left(\frac{d_d + d_l}{2}\right)^2}{4} \tag{2-118}$$

where, n_s is the number density of sliding bubbles.

A_4 is the transient conduction area of sliding bubbles, given by,

$$A_4 = \frac{3}{4}\left[n_b l_s K\left(\frac{d_d + d_l}{2}\right) - A_2 \right] \tag{2-119}$$

The single phase convection heat transfer is then calculated as,

$$q_{nc} = h_{nc} A_{nc} \Delta T \tag{2-120}$$

The total heat flux is calculated as,

$$q_{total} = (q_{me} + q_{tc}) x_{st} + (q_{mes} + q_{tcs}) x_s + q_{nc} \tag{2-121}$$

where, $x_{st} = 1$, $x_s = 1$, when, $R = \dfrac{1}{n_b \pi d_d^{\,2}/4} > 1$

and, $x_{st} = R$, $x_s = 0$, when $R \le 1$.

However, the values of x_{st} and x_s have to be adjusted or corrected when comparing the model with existing experimental data.

Basu et al. (Basu et al. 2005) proposed a mechanistic wall heat flux partitioning model for subcooled flow boiling. It's proposed that all of the energy from the heating surface is first transferred into the superheated liquid layer adjacent to the wall. A fraction of this energy generates vapor bubbles while the rest contributesto sensible heating of the bulk liquid. Thus, the total heat flux can be expressed as a sum of two components, forced convection and transient conduction,

$$q = q_{fc} + q_{tc} \tag{2-122}$$

The model is only applicable for subcooled flow boiling heat transfer prediction in the region downstream of the onset of significant voids (OSV). The two heat flux components were modeled for two cases, 1) bubble sliding at relatively low heat flux and 2) bubbles merging without sliding at higher heat flux. In case of flow boiling with bubble sliding, the transient conduction component is given by,

$$q_{tc} = \frac{1}{t_w + t_g}\int_0^t \frac{k_l}{\sqrt{\pi\alpha_l t}}\left(\Delta T_w + \Delta T_{sub}\right)A_{sl}R_f N_a dt \tag{2-123}$$

where, t_w and t_g are bubble waiting time and growth time, respectively. A_{sl} is the area swept by a sliding bubble, given as $A_{sl} = Cdl$, in which C is the ratio of bubble base area to bubble projected area. d is the bubble average diameter, equal to $(d_d+d_l)/2$. l is the sliding distance. $R_f N_a$ represents the number of bubbles sliding per unit area. $t = t^*$ when $t^* < (t_w + t_g)$ and $t = (t_w + t_g)$ when $t^* \geq (t_w + t_g)$. t^* is given by,

$$t^* = \left(\frac{k_l}{\bar{h}_{fc}}\right)^2 \frac{1}{\pi\alpha_l} \tag{2-124}$$

where, $\bar{h}_{fc}$ is the enhanced single phase convection heat transfer coefficient,

The single-phase convection heat transfer component is given by,

$$q_{fc} = \bar{h}_{fc}\left(\Delta T_w + \Delta T_{sub}\right)\left[1 - A_{sl}R_f N_a\right] + \bar{h}_{fc}\left(\Delta T_w + \Delta T_{sub}\right)A_{sl}R_f N_a\left(1 - \frac{t^*}{t_w + t_g}\right) \tag{2-125}$$

In case of high wall superheat and wall heat flux, bubbles tend to merge with each other before sliding. At any given moment, the whole surface area is experiencing an

enhanced forced convection or transient conduction. The two heat flux components are given by,

When $t^* \le t_w$,

$$q_{tc} = \frac{1}{t_w + t_g}\int_0^{t^*} \frac{k_l}{\sqrt{\pi\alpha_l t}}\left(\Delta T_w + \Delta T_{sub}\right)dt \tag{2-126}$$

$$q_{fc} = \bar{h}_{fc}\left(\Delta T_w + \Delta T_{sub}\right)\frac{t_w - t^*}{t_w + t_g} + \bar{h}_{fc}\left(\Delta T_w + \Delta T_{sub}\right)\left[1 - A_b N_a\right]\frac{t_g}{t_w + t_g} \tag{2-127}$$

where, A_b is the bubble base area, $A_b = \pi(Cs)^2/4$, and s is the average distance between adjacent nucleation sites.

When $t^* > t_w$,

$$q_{tc} = \frac{1}{t_w + t_g}\left[\int_0^{t_w} \frac{k_l}{\sqrt{\pi\alpha_l t}}\left(\Delta T_w + \Delta T_{sub}\right)dt + \int_{t_w}^{t} \frac{k_l}{\sqrt{\pi\alpha_l t}}\left(\Delta T_w + \Delta T_{sub}\right)\left[1 - A_b N_a\right]dt\right] \tag{2-128}$$

where $t = t_w + t_g$, if $t^* \ge t_w + t_g$, otherwise $t = t^*$.

$$q_{fc} = \bar{h}_{fc}\left(\Delta T_w + \Delta T_{sub}\right)\left[1 - A_b N_a\right]\frac{t_w + t_g - t^*}{t_w + t_g} \tag{2-129}$$

if $t_w < t < t_w + t_g$, otherwise, $q_{fc} = 0$.

The effect of heating surface materials on pool boiling heat transfer has been studied by many different researchers. The impact of heating wall thermal properties on the boiling process was first investigated by Bonilla and Perry (Bonilla and Perry 1941). Differences were found between boiling of ethanol on different heating surfaces, such as copper, gold and chromium electroplated surfaces. Berenson (Berenson 1962) experimentally examined the pool boiling of n-pentane on surfaces with different materials, surface roughness, and cleanliness. Different heat transfer coefficients were observed for boiling on wires made of different materials (Farber and Scorah 1968). Bliss et al. (Bliss et al. 1969) conducted tests of nucleate boiling on a stainless steel tube and also the same stainless steel tube coated with different materials, such copper, zinc, tin, nickel, cadmium and chromium. It was found

nucleate boiling heat transfer showed significant differences for different coatings. For example, the heat transfer coefficient between copper and zinc coatings had a difference in the range of 200 to 300 percent.

A method was proposed by Rohsenow (Rohsenow 1952) based on a logical explanation of the mechanism of heat transfer associated with the boiling process to correlate heat transfer data for nucleate pool boiling. A correlation was proposed to fit a wide range of data of water pool boiling on a platinum wire,

$$\frac{c_l T_x}{h_{fg}} = C_{sf}\left(\frac{q/A}{\mu_l h_{fg}}\sqrt{\frac{g_0\sigma}{g(\rho_l-\rho_v)}}\right)^{0.33}\left(\frac{c_l\mu_l}{k_l}\right)^{1.7} \tag{2-131}$$

in which: c_l, k_l, and μ_l are specific heat, thermal conductivity, and dynamic viscosity of saturated liquid, respectively; T_x is wall superheat; h_{fg} is latent heat of evaporation; g and g_0 are the acceleration of gravity and a conversion factor, respectively; and ρ_l, ρ_v and σ are liquid density, vapor density and surface tension, respectively. A constant, C_{sf}, was proposed to account for liquid-surface combination effects. It was found for the water-platinum combination, that the value of C_{sf} is 0.013 with a spread of data of approximately ±20%. The values of the constant, C_{sf}, were also obtained for other fluid-surface combinations. For benzene-chromium, ethyl alcohol-chromium, n-pentane-chromium and water-brass combinations, the values of the constant, C_{sf}, were found to be 0.010, 0.0027, 0.015 and 0.0060, respectively.

Recent experimental work done by Jabardo et al. (Jabardo et al. 2009) tested the roughness and surface material effects on nucleate boiling heat transfer from cylindrical surfaces to refrigerants such as R134a and R123. Pool nucleate boiling data were obtained for both refrigerants on copper, brass and stainless steel surfaces. The heat transfer coefficient was correlated with wall heat flux in the form of,

$$h = Cq^m \tag{2-132}$$

in which, m is a constant taking account effect of materials. A slight difference on values of m was found between copper and brass surfaces. However, the value of m for stainless steel

surfaces was found to be significantly lower than the other two surfaces, indicating lower boiling heat transfer coefficients.

A lot of research has been done in the past to investigate the heating surface material effects on the nucleate boiling heat transfer. However, most was focused on pool boiling while similar studies for flow boiling conditions is lacking. More importantly, due to limitations of experimental observations and measurement methodologies, most of the early research was mainly based on empirical means to correlate experimental data. Mechanism behind the material effect was not fully understood.

2.4 SUMMARY

The main objective of current thesis is to study subcooled flow boiling on both copper and stainless steel surfaces from both microscopic and macroscopic points of view. This chapter of literature review, therefore, has been main focused on three major topics related to the subcooled flow boiling process, such as boiling capacity, nucleation site activation, number density and its distribution, and bubble dynamics. The literature review presented in this chapter covers a wide range of researches done in the past to understand the flow boiling phenomenon. These researches efforts are including experimental measurements and observations, analytical and theoretical works, model developments, empirical and semi-empirical correlations, developments on new technologies, etc.

CHAPTER 3

EXPERIMENTAL SETUP

In this chapter, the experimental facility and measurement techniques used in this subcooled flow boiling experimental study are introduced. The major components of the experimental facility include a refrigerant loop and an electrically heated test section. Instruments include thermocouples, pressure transducers, flow meters, etc. They are used to measure quantities such as temperature, pressure, mass flow rate, etc. Most of the signals are collected by a data acquisition system, which includes an HP 75000 serial B data acquisition equipment and a personal computer (PC). A high-speed digital camera with high resolution is used to record bubble and nucleation site images.

3.1 SUBCOOLED FLOW BOILING EXPERIMENTAL TEST APPARATUS

The subcooled flow boiling experimental test apparatus consists of a refrigerant loop, two commercial water cooled chiller systems which control the temperature of the sub-loops and the electrically heated test section. A schematic diagram of the flow boiling test apparatus is shown in Figure 3.1. The details of these components are described in the following sections.

3.1.1 Refrigerant loop

The refrigerant loop is designed to supply a pure, uncontaminated coolant source to the test section at the desired pressure, inlet temperature, and mass flow rate. A typical and widely used refrigerant, R134a, is chosen as the working fluid for its relatively low critical pressure, saturation temperature, and latent heat. A list of the physical and thermal properties is given in Table 3.1.

A liquid reservoir is used to store refrigerant and to stabilize the system pressure. A gear pump, manufactured by Micro-Pump ®, is installed in the loop to drive the coolant flow

and to provide a variable range of mass flow rates, up to 4 LPM (liter per minute). The mass flow rate controlled by adjusting the electrical voltage applied through a variac to the pump. An electric pre-heater, which provides different inlet subcooling levels to the test section, is installed upstream of the test section. The pre-heater consists of three copper tubes 1.8 meters in length and 9.525 mm in outer diameter and assembled in a serpentine shape. The outside of the tubes is wrapped with twelve electrical heating stripes with variable powers. Ten of these twelve stripes are controlled by 4 switches and provide constant power, while the othe two provide a different power level controlled by a 115 Volt variac. The rectangle test section is heated by electric power from the bottom side. The test section has three quartz windows installed on the remaining sides, which enable direct observations of the flow boiling process. One cooling sub-loop is installed immediately downstream of the test section. It cools the refrigerant exiting from the test section, which is especially important for a flow boiling experiment to maintain a constant system pressure. Another cooling sub-loop is installed immediately upstream of the gear pump and downstream of the liquid reservoir, which ensures there is no refrigerant vapor entering the pump. The working fluid for these two cooling sub-loops is R-12, which is then cooled in two commercial water chillers.

3.1.2 Test section

An exploded view of the test section assembly is shown in Figure 3.2. The rectangular copper heating block, 12.7 mm by 107.95 mm (width by length), is installed in the middle of a straight horizontal rectangular stainless steel flow channel. The dimensions of the flow channel are 1 m by 12.7 mm by 12.7 mm (length by width by height). The entrance length, which is measured from the entrance of the straight flow channel to the leading edge of the test section heating surface, is 490 mm. The ratio of entrance length to the flow channel hydraulic diameter is calculated as 38.58. This is much larger than the recommended entrance length ratio values of ~19 to ~24, calculated from experimental conditions investigated, such as system pressures ranging from 400 kPa to 800 kPa and liquid velocities ranging from

0.1m/s to 0.3m/s. The value of the required entrance length to hydraulic diameter ratio is evaluated by (Sanchayan and Pijush 2005, 425) as,

$$\frac{L_e}{D_h} \approx 4.4(\mathrm{Re})^{1/6} \qquad (3\text{-}1)$$

The test section is heated by seven cartridge heaters, which provide a maximum total power of 750×7=5050W. These seven heaters are divided into three groups with a 2/3/2 pattern, each of which can be turned on and off independently. The electric power level is controlled by an auto-transformer and measured by voltmeter and ammeter instruments in the power circuit. Each of these seven cartridge heaters contains one continuous 76.2 mm long heated section. All heaters have an INCOLOY sheath to enhance the heat conduction from heaters to copper base block. To obtain a uniform heat flux and temperature profile close to the heating surface, it's recommended to turn on either all of these 7 cartridge heaters or the center 3 ones. A numerical study by using FLUENT® shows that with the center 3 cartridge heaters turned on, a nearly identical temperature profile can be obtained compared to the 7 cartridge heaters turned on condition.

During the experiments, the critical heat flux condition can be achieved. The film boiling phenomenon normally takes place at the post-CHF stage, which gives a much smaller heat transfer coefficient compared to nucleate boiling heat transfer. To avoid an accident scenario with burn-out or components damage, the electric power applied on the heating block has to be shut off promptly. The maximum temperature the INCOLOY sheath can with stand is approximately 800ºC, while the silicone rubber O-ring which seals the gap between the flow channel and the heating block can only sustain temperatures lower than 250 ºC. To assure there is no accidental scenario, a transient heat transfer simulation was carried out with FLUENT® to calculate the temperature profile inside the copper base block and heating block at the post-CHF stage. Conservative boundary conditions were assigned, i.e., the heat transfer coefficient from the heating block to fluid side drops to zero, and heat can only be removed by natural convection and radiation heat transfer at surfaces exposed to air. 100 seconds of post CHF transient heat transfer simulation has been done with FLUENT® to predict the

temperature profiles in the heating blocks. The simulation obtained a maximum critical heat flux in 800kPa pressure, of around $6.0\times10^5 W/m^2$. The temperature profile is shown in Figure 3.3. The simulation results show that, at 100 seconds after CHF occurs, the temperature at the O-ring is around 169 ºC, and the maximum temperature on the INCOLOY sheath is around 196 ºC. This simulation result ensures that when CHF occurs, there will be enough time to turn off the heaters.

Two heating blocks with copper and stainless steel heating surfaces were employed separately to study subcooled flow boiling performance for materials with different thermal properties. Copper was selected as the base material for both the heating block and the base block to reduce the overall temperature magnitude in the blocks due to its very high thermal conductivity, ~400W/m·K. The heating block with a copper heating surface was machined from a pure copper block. To make a heating block with stainless steel heating surface, a 1 mm thick stainless steel strip was attached onto the copper block using silver solder. The stainless steel layer thickness was selected so as not to significantly increase the overall temperature magnitude due to its fairly poor thermal conductivity, ~15W/m·K. However, the stainless steel layer has to be thick enough to represent the material's boiling heat transfer characteristics, or more specifically, the local temperature disturbance caused by bubble wouldn't penetrate to the copper base material.

To measure the heating surface wall temperature and heat flux, eight type-K thermocouples were installed in the copper heating block. The heat flux can be calculated from the temperature gradient in the copper heating block, and the wall temperature can be calculated from the temperatures measured at the thermocouples located very close to the heater wall, with a distance correction applied. The detailed test section dimensions and locations of thermocouples are shown in Figure 3.4.

3.2 INSTRUMENTATION AND MEASUREMENTS

The signals recorded during the flow boiling heat transfer experiment include directly measured quantities, such as temperature, pressure, mass flow rate, electric voltage and current, etc. Quantities calculated from the directly measured quantities, such as power and heat flux are also recorded. An array of instruments, such as thermocouples and pressure transducers, is employed to measure these quantities. A data acquisition system for temperature, pressure and mass flow rate signals includes an HP 75000 serial B data acquisition equipment and a PC. In addition, a high-speed digital camera was used to observe the small scale bubble dynamics, which were recorded in a second PC.

Types K and T thermocouples are used for temperature measurements. All thermocouples are calibrated using an ice bath reference and are considered valid from 5 ºC to 100 ºC with an uncertainly of ±0.1 ºC. The working fluid inlet and outlet temperatures are directly measured with thermocouples inserted in the flow channel. Eight thermocouples were installed in the heater block, so that the heat flux then can be calculated from the temperature gradient inside the heating block. The uncertainty for heat flux measurements is estimated to be ±3%, given the maximum temperature measurement error of 0.75%. The heating surface wall temperature can be calculated from temperatures measured at locations immediately beneath the surface by compensating the temperature difference due to the distance from the wall surface to the thermocouples. The saturation temperature is calculated from the measured system pressure. The bulk temperature, T_b, is an average value of inlet and outlet temperatures.

Two BEC strain-gage type pressure transducers are installed before the pre-heater inlet and the test section inlet. Both transducers are calibrated using a dead weight tester with an uncertainly of ±900Pa with a range of 0-300psi (0-2100kPa).

The liquid mass flow rate is measured by a model D12 mass flow meter (inertial flow meter or Coriolis flow meter) manufactured by Micro-Motion. A pair of U-shaped tubes in the flow meter vibrates as fluid flows by, and a current which depends on the frequency of vibration is delivered to the data acquisition system.

A Photron FASTCAM Ultima 1024 high-speed digital camera is used to record the boiling phenomena in the test section. The camera can acquire images at a rate up to 12000 frames per second (fps) using an intensive back-lit source, with various magnifications controlled by a set of micro lenses, shown in table 3.2. The images and videos were stored in a computer in digital format through an IEEE 1394 fire wire connection. The resolutions of the camera range from 2.60 *μm/pixel* to 16.73 *μm/pixel*, depending on the lenses magnification selected. In order to achieve the highest possible resolution and best fidelity, the camera is mounted on a 65mm XYZ linear stage and the focal length of the lens is fixed at a constant value, which is about 5 cm. The XYZ linear stage provides a smooth and stable camera positioning function with travel distance of 30/30/45(X/Y/Z) mm, and sensitivity of 0.1 mm. The camera is calibrated by comparing the size of an object in the image and its real size which is measured with a micrometer. The uncertainly of the image is estimated to be 1 *pixel* and therefore the error depends on the image size and the lens magnification selected.

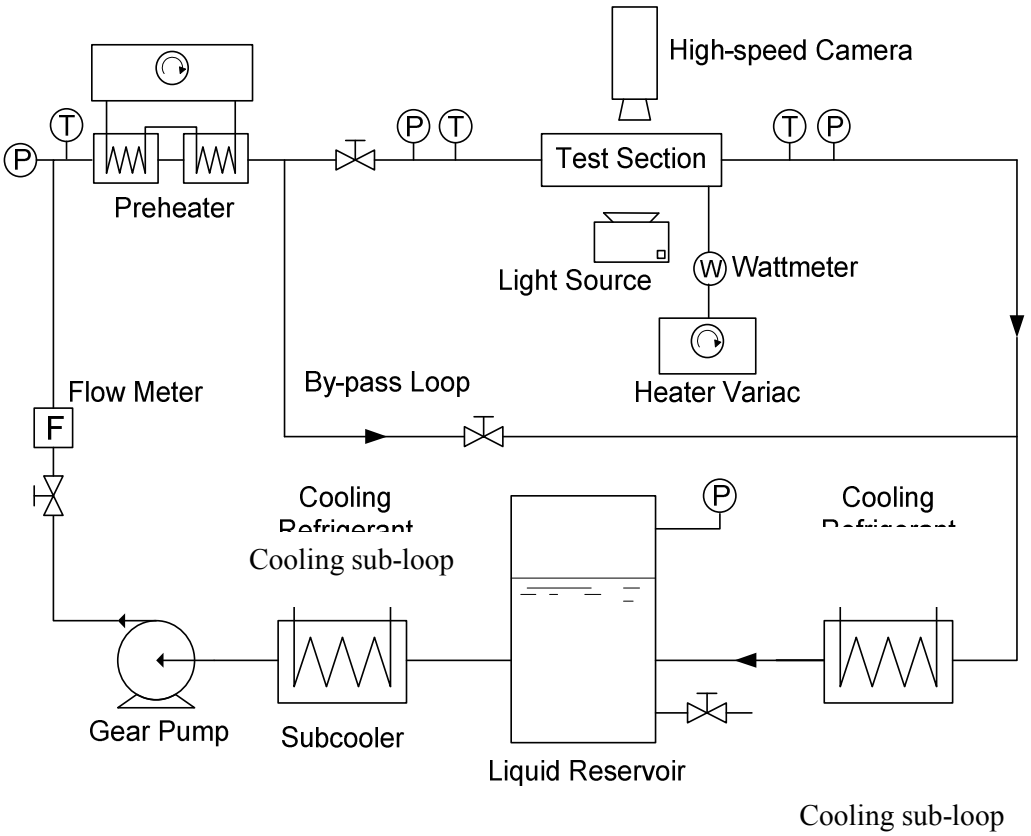

Figure 3.1 Schematic diagram of the flow boiling test apparatus

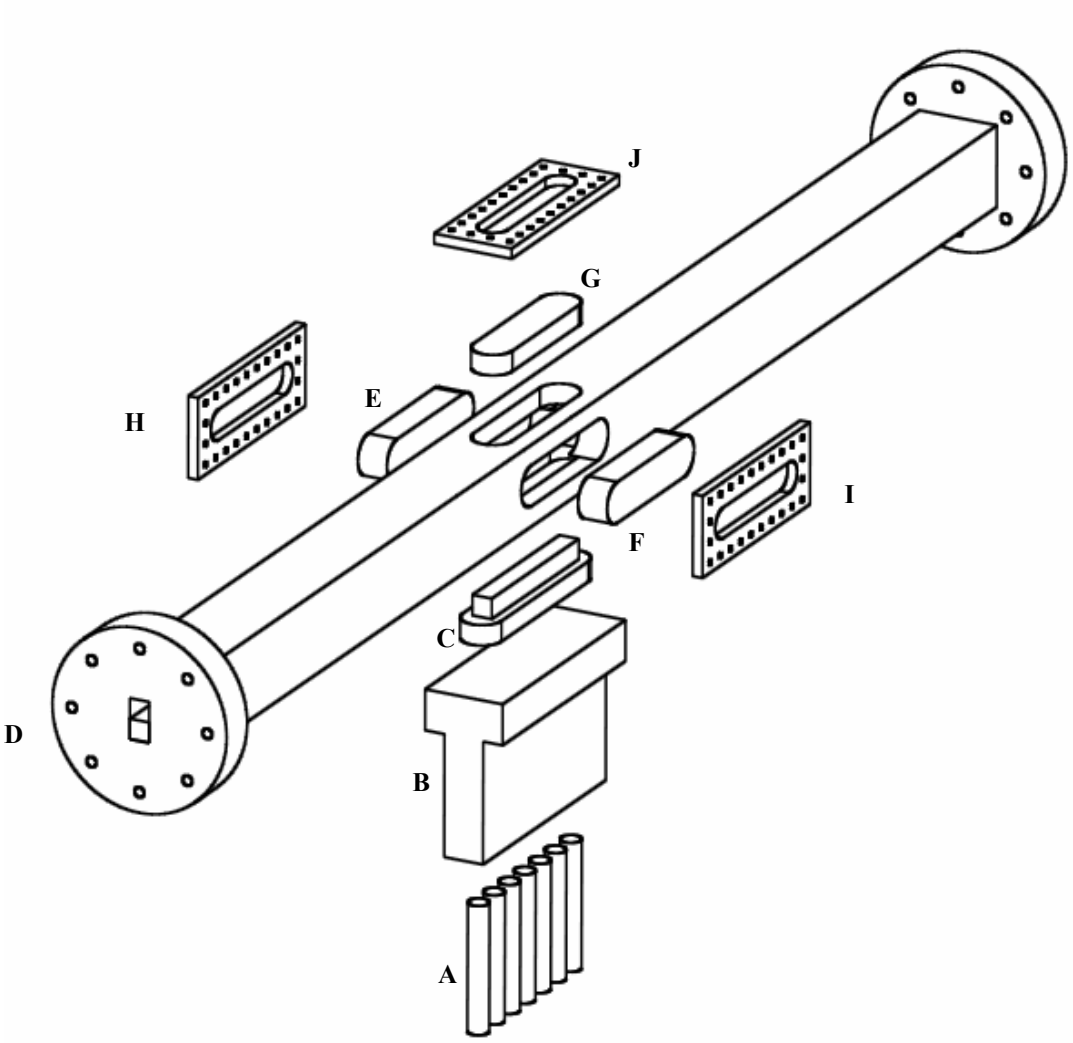

A – Cartridge heaters

B – Copper base block

C – Heating block

D – Stainless steel flow channel

E – Rear quartz window

F – Front quartz window

G – Top quartz window

H – Rear stainless steel window mounting

I – Front stainless steel window mounting

J – Top stainless steel window mounting

Figure 3.2. An exploded view of the test section assembly

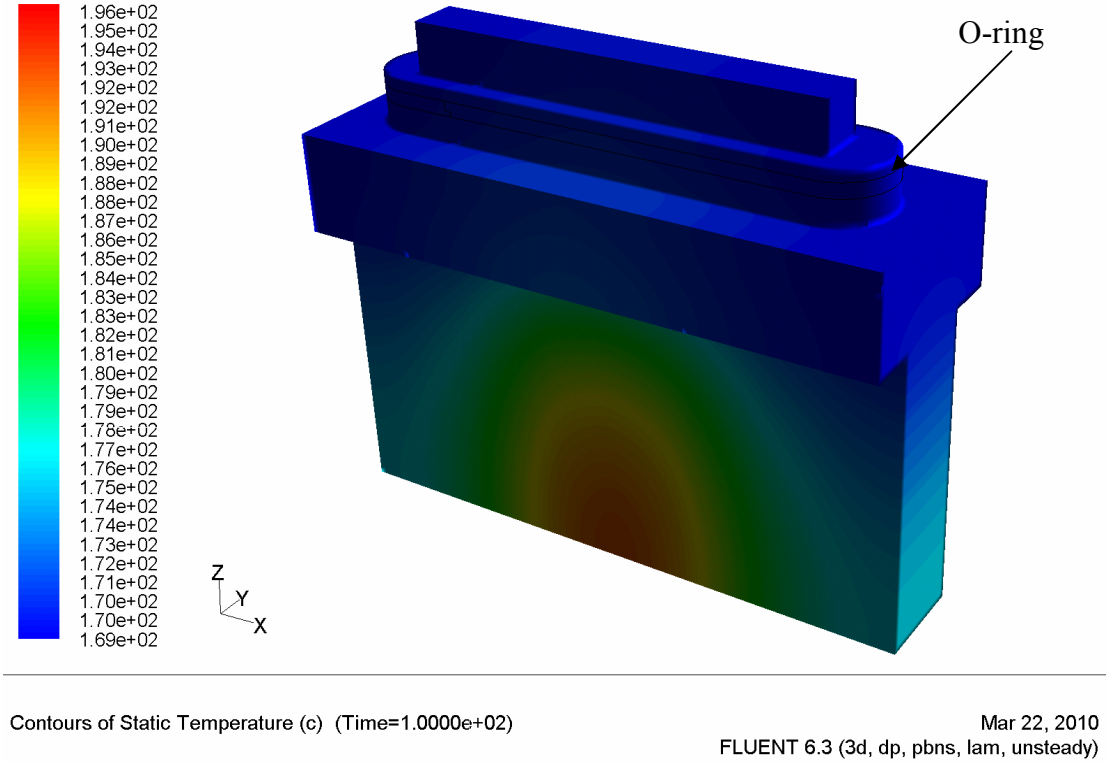

Figure 3.3. Temperature profile on heating block walls at 100 seconds after critical heat flux occurring with power on.

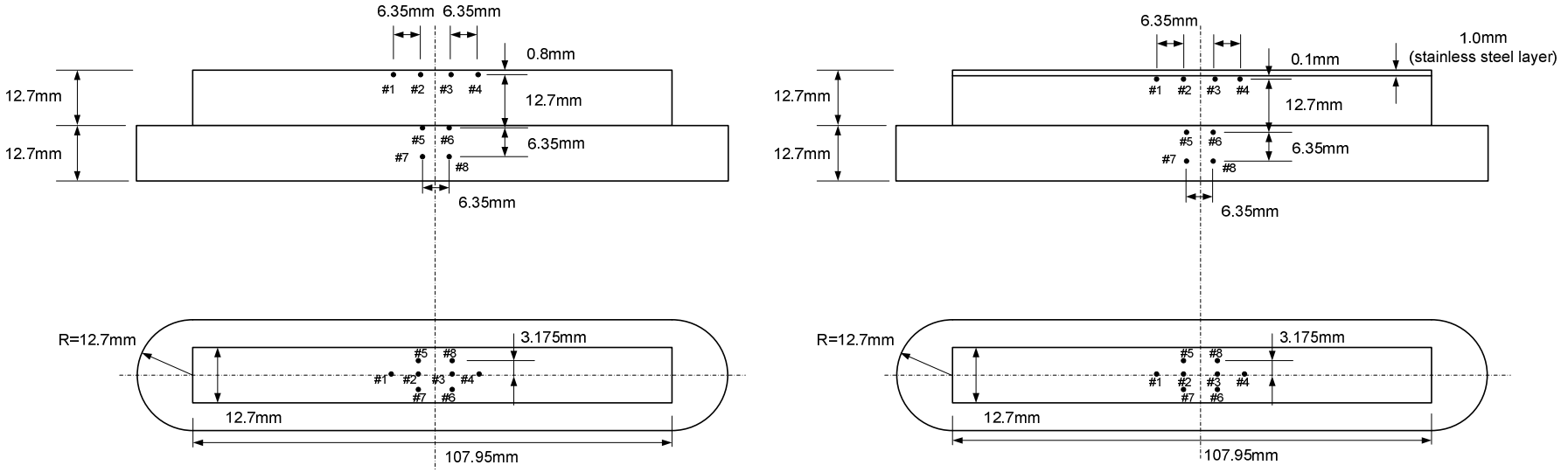

(# numbering of thermocouples)

(a) Pure copper test section

(b) Copper test section coated with stainless steel layer

Figure 3.4. Schematic drawings of test sections and locations of thermocouples.

Table 3.1. Physical and thermal properties of R134a at different pressures.

P (MPa)	T_{sat} (K)	T_{sat} (ºC)	ρ_l (kg/m3)	ρ_v (kg/m3)	k_l (W/m·K)	$C_{p,l}$ (J/kg·K)	h_{fg} (J/kg)	σ (N/m)
0.20	263.07	-10.08	1327.40	10.012	9.653E-02	1315.4	206.02	1.303E-02
0.25	268.87	-4.28	1308.80	12.394	9.392E-02	1329.7	201.81	1.218E-02
0.30	273.82	0.67	1292.60	14.770	9.172E-02	1342.9	198.10	1.146E-02
0.35	278.18	5.03	1278.00	17.147	8.979E-02	1355.2	194.72	1.084E-02
0.40	282.08	8.93	1264.70	19.529	8.808E-02	1367	191.61	1.029E-02
0.45	285.63	12.48	1252.30	21.918	8.654E-02	1378.4	188.70	9.791E-03
0.50	288.88	15.73	1240.80	24.317	8.513E-02	1389.4	185.97	9.340E-03
0.55	291.90	18.75	1229.90	26.729	8.382E-02	1400.2	183.37	8.925E-03
0.60	294.72	21.57	1219.50	29.155	8.261E-02	1410.9	180.89	8.542E-03
0.65	297.37	24.22	1209.70	31.596	8.147E-02	1421.4	178.51	8.186E-03
0.70	299.86	26.71	1200.20	34.054	8.040E-02	1431.8	176.21	7.852E-03
0.75	302.23	29.08	1191.10	36.530	7.939E-02	1442.3	173.98	7.539E-03
0.80	304.48	31.33	1182.20	39.025	7.842E-02	1452.7	171.81	7.243E-03
0.85	306.62	33.47	1173.70	41.541	7.751E-02	1463.1	169.71	6.963E-03
0.90	308.68	35.53	1165.40	44.078	7.663E-02	1473.6	167.65	6.698E-03
0.95	310.65	37.50	1157.20	46.638	7.579E-02	1484.2	165.63	6.445E-03
1.00	312.54	39.39	1149.30	49.222	7.498E-02	1494.8	163.66	6.204E-03
1.05	314.36	41.21	1141.60	51.831	7.420E-02	1505.6	161.73	5.974E-03
1.10	316.12	42.97	1134.00	54.465	7.345E-02	1516.5	159.82	5.754E-03
1.15	317.82	44.67	1126.50	57.126	7.272E-02	1527.6	157.95	5.543E-03
1.20	319.46	46.31	1119.20	59.815	7.201E-02	1538.8	156.09	5.340E-03

Table 3.2 Camera magnifications and corresponding length/pixel ratios

Magnification Index	μm/pixel	pixel/mm
3	16.73	59.76
4	12.93	77.33
5	10.34	96.67
6	8.62	116.00
7	7.29	137.09
0.58	4.52	221.46
1	2.60	384.91

CHAPTER 4

EXPERIMENTAL RESULTS

To understand subcooled flow boiling heat transfer, experimental work has been pursued in this study and the experimental results obtained are presented in this chapter. The experimental results include three major parts, subcooled flow boiling performance from a macroscopic point of view, nucleation site density and bubble dynamics from a microscopic point of view. Flow boiling heat flux and heat transfer coefficients have been experimentally measured on both copper and stainless steel surfaces under different experimental conditions, such as pressure, flow rate and inlet subcooling. In terms of heat flux and heat transfer coefficient, significant differences are found between copper and stainless steel heating surfaces. To explain the different flow boiling performances on these two heating surfaces, a high-speed digital camera was utilized. Nucleation site densities and bubble dynamics have been visually observed and measured under different experimental conditions. These two quantities are believed to be key parameters in determining flow boiling heat flux.

4.1 NUCLEATION SITE DENSITY AND DISTRIBUTION

4.1.1 Nucleation site density

The importance of active nucleation site density was realized in early stages of boiling heat transfer study. Both analytical and experimental work has been done to understand the nucleation site activation criteria, nucleation site density and its distribution. Some early analytical work on nucleation site activation was provided by Bankoff (Bankoff 1958), Griffith (Griffith and Wallis 1960) and Hsu (Hsu 1962). Salt deposition (Gaertner and Westwater 1963), gas bubble nucleation (Eddington and Kenning 1978), direct visualization (Wang and Dhir 1993a) and liquid crystal thermography (Hardenberg et al. 2004) have been used to measure the nucleation site densities in pool boiling. In general, it's more difficult to

measure this in flow boiling. Firstly, at low to moderate wall heat fluxes, bubbles tend to slide on the heating surface before lifting-off. By counting number of bubbles from still boiling images does not provide accurate nucleation site densities. Experimental evidence shows there are normally several sliding bubbles released from a same nucleation site, so the nucleation site density can be greatly overestimated by counting bubble numbers. Secondly, at relatively higher heat fluxes, intense bubble coalescence takes place such that adjacent bubbles tend to merge into big bubbles or vapor patches. The vapor volume fraction in the bulk flow is also significantly larger compared to lower heat flux conditions. When using direct visualization techniques, both effects lead to undesired light reflection and therefore blurred images. A multiple image ensemble method was used by Zeng and Klausner (Zeng and Klausner 1993) to count nucleation site density from digital images taken from a side view. This, however, creates more uncertainty as bubbles at different depths of field collapse together on the image.

In flow boiling with R134a, vapor bubbles have very short lifespan, in the magnitude of milliseconds. They are also very small, in the magnitude of tens of microns. To accurately measure the quantities of interest, such as bubble size and growth rate, advanced technology is required. A Photron FASTCAM Ultima 1024 high-speed digital camera with high magnification was used in this study to record high frequency boiling images. To acquire more accurate nucleation site density measurements, a normal view of the heating surface is preferred rather than a side view, in which bubbles at different depths of field produce overlapping images and are difficult to be distinguished from each other. However, the disadvantage of a normal view is that a back-lighting source cannot be applied and therefore the image quality is not as good as a side view in terms of brightness and contrast. To obtain bubble images in a view normal to the heating surface, a quartz window was installed on the top side of the flow channel and the high-speed digital camera was mounted above the test section. Two light sources were provided from above the test section through the same quartz window where bubble images were taken. Bubble images on the heating surface were recorded at high frequencies, 1000/2000 fps, for time periods of several seconds. Normally,

for each experimental condition, a set of several thousands of images were obtained for data analysis. Recorded image sets can be loaded into a computer program implemented by Visual C++ ® to be displayed frame by frame, either automatically or manually. Every single active nucleation site can be manually identified and their coordinates recorded. Measurement errors mainly come from nucleation sites not always being activated. Due to random characteristics of boiling, not all nucleation sites are constantly activated. It's been observed that some sites can be randomly activated or deactivated. At high heat fluxes the error is estimated to be relatively large since nucleation sites are more crowded and this activation/deactivation process occurs more frequently. The measurement error was estimated to be approximately 10% by counting the sites that are not constantly activated. Figure 4.1 shows a typical bubbles image obtained for R134a in flow boiling on the copper surface. Locations of active nucleation sites are listed in Table 4.1 and shown in Figure 4.2.

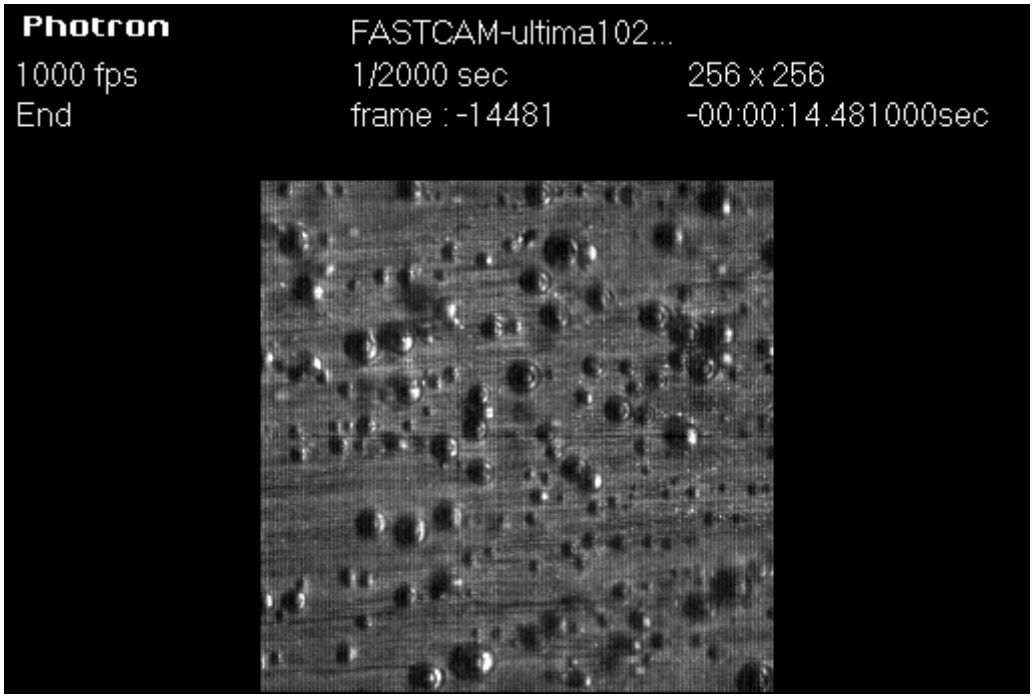

Figure 4.1. A typical bubble image from a set of bubble images at high camera frame speed to identify active nucleation sites locations. Experimental conditions: 606kPa, ΔT_w=9.23ºC. Image taken conditions: magnification index 3, 1000 fps, 1/2000 second of shutter time. Other information: 256 by 256 pixels of image size, frame number, 13616, real time, 13.616 seconds.

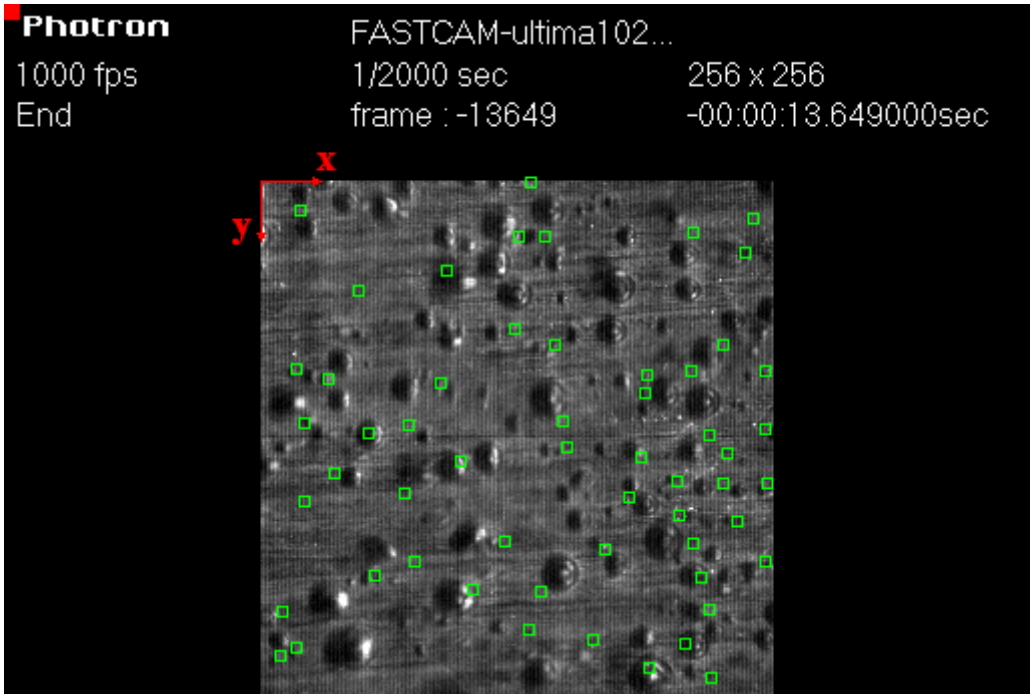

Figure 4.2. Nucleation sites (green squares) identified from bubble images shown in Figure 4.1.

Table 4.1. Numbering and coordinates of nucleation sites for the bubble images in Figures 4.1. and 4.2.

Number of nucleation sites: 54									
site #	x (pixel)	y (pixel)	x (mm)	y (mm)	site #	x (pixel)	y (pixel)	x (mm)	y (mm)
1	153	133	2.560	2.225	28	246	19	4.116	0.318
2	238	170	3.982	2.844	29	216	26	3.614	0.435
3	134	224	2.242	3.748	30	242	36	4.049	0.602
4	100	140	1.673	2.342	31	215	95	3.597	1.589
5	54	126	0.903	2.108	32	231	82	3.865	1.372
6	90	101	1.506	1.690	33	74	122	1.238	2.041
7	34	99	0.569	1.656	34	37	146	0.619	2.443
8	127	74	2.125	1.238	35	166	229	2.777	3.831
9	142	28	2.376	0.468	36	253	151	4.233	2.526
10	129	28	2.158	0.468	37	252	124	4.216	2.075
11	147	82	2.459	1.372	38	224	127	3.748	2.125
12	192	106	3.212	1.773	39	193	97	3.229	1.623
13	216	181	3.614	3.028	40	252	95	4.216	1.589
14	224	214	3.748	3.580	41	135	1	2.259	0.017
15	225	248	3.764	4.149	42	20	15	0.335	0.251
16	194	243	3.246	4.065	43	93	45	1.556	0.753
17	212	231	3.547	3.865	44	22	160	0.368	2.677
18	252	190	4.216	3.179	45	209	167	3.497	2.794
19	208	150	3.480	2.510	46	184	158	3.078	2.643
20	57	197	0.954	3.296	47	77	190	1.288	3.179
21	106	204	1.773	3.413	48	151	120	2.526	2.008
22	122	180	2.041	3.011	49	231	151	3.865	2.526
23	18	233	0.301	3.898	50	233	136	3.898	2.275
24	10	237	0.167	3.965	51	220	198	3.681	3.313
25	11	215	0.184	3.597	52	172	184	2.878	3.078
26	18	94	0.301	1.573	53	22	121	0.368	2.024
27	190	138	3.179	2.309	54	49	55	0.820	0.920

Nucleation site densities were measured on both copper and stainless steel surfaces for different ranges of experimental conditions; system pressures from 450kPa to 700kPa, wall superheats from 5.4ºC to 12.2ºC, and liquid velocities from 0.1m/s to 0.25m/s.

The nucleation site densities on the copper surface and the stainless steel surface are plotted against wall superheat in Figures 4.3 and 4.4, respectively. From these two plots, a clear linear trend is found at fixed pressures in a log-log scale. This trend shows a power law relationship, indicating that wall superheat is an important correlating parameter for flow boiling nucleation site density at a given pressure. However, for a given wall superheat, the nucleation site density changes dramatically from low pressure to high pressure. For example,

for wall superheat of 8.8ºC on the copper heating surface, the nucleation site density is 6.65×10^6 sites/m^2 at pressure of 700kPa, which is more than ten times larger than that at 500kPa, 5.45×10^5 sites/m^2. Experimental results suggest that, although wall superheat is an important correlating parameter, by itself it is insufficient to correlate the nucleation site density. To account for the pressure's effect, a new parameter needs to be introduced. As suggested by Griffith and Wallis (Griffith and Wallis 1960), the critical cavity diameter, D_c,

$$D_c = \frac{4\sigma T_{sat}}{\rho_g h_{fg} \Delta T_W} \tag{4-1}$$

can be used as a criterion for bubbles initiation. Griffith's study suggested that at a certain wall superheat, cavities with mouth sizes smaller than the critical cavity size, given by equation (4-1), cannot be activated. The critical cavity diameter, D_c, was later used by different researchers (Mikic and Rohsenow 1969, Bier et al. 1978, Cornwell and Brown 1978, Wang and Dhir 1993a, etc.) to correlate with active nucleation site density. For the current study, nucleation site densities for both copper and stainless surfaces are plotted in Figures 4.5 and 4.6, respectively, as a function of critical cavity diameter. Both Figures 4.5 and 4.6 show that, in log-log plots all nucleation site density data are approximately collapsed to a single straight line for given heating surfaces. For the copper heating surface, the measured nucleation site density data were correlated as,

$$N_a = 4.3558\times10^{-33} D_c^{-5.7975} \tag{4-2}$$

with most of the data within a ±25% deviation. For the stainless steel heating surface, the measured nucleation site density data were correlated as,

$$N_a = 5.2634\times10^{-23} D_c^{-4.3703} \tag{4-3}$$

with most of the data within a ±50% deviation. However, a trend can be found in both Figures 4.5 and 4.6 that, for a given D_c nucleation site densities were lower for higher pressures, which is clearer for the stainless steel surface. This trend indicates that the critical cavity size is still not the single parameter which ultimately correlates with the nucleation site density. Wang and Dhir (Wang and Dhir 1993a) concluded from their research that surface wettability

played an important role in activation nucleation sites. In their study, water pool boiling experiments were carried out at atmospheric pressure and the wettability changed due to different surface oxidation levels. The active nucleation site density was correlated with critical cavity size and contact angle. Wang and Dhir had experimentally found that for given conditions, surfaces with lower wettability, and therefore larger contact angle, tended to have more nucleation sites. For R134a used in the current study, surface tension is smaller at higher pressure, which normally gives a larger contact angle (Wu et al. 2007). If Wang and Dhir's theory is true, the nucleation site density should be higher at higher pressures since it has a lower wettability. Experimental results obtained in the current study, however, contradict with Wang and Dhir's findings. The contradiction indicates that the Wang and Dhir theory of surface wettability may not be applied to scenarios where pressure, instead of surface conditions, is the root cause of wettability changes.

Based on Griffith's theory, Hsu (Hsu 1962) proposed that nucleation sites could only be effective in a certain sizes range. The maximum and minimum effective cavity sizes are two roots of the quadratic equation, given in (2-3). The range of effective cavity sizes can be estimated as the difference between the maximum and minimum effective cavity sizes,

$$D_{c,\max} - D_{c,\min} = \frac{2\delta}{C_1}\sqrt{\left(1 - \frac{D_c C_3}{\delta} - \frac{\Delta T_{sub}}{\Delta T_{sub} + \Delta T_w}\right)^2 - \left(\frac{D_c C_3}{\delta}\right)^2} \qquad (4\text{-}4)$$

in which, C_1 and C_3 are constants. D_c, ΔT_{sub}, ΔT_w and δ are critical cavity diameter, bulk subcooling, wall superheat and thickness of liquid thermal layer, respectively. For a given D_c, the corresponding wall superheat at low pressure is higher from equation (2-2). Also, if ΔT_{sub}, and δ are given the same, there's a wider range of effective cavity sizes at lower pressures than that at higher pressures from equation (4-4). This explains the observed results that at a given D_c, the nucleation site density is higher at lower pressures.

Nucleation site densities for both copper and stainless steel surfaces are plotted against the wall heat flux in Figures 4.7 and 4.8, respectively. These figures show that the

relationship between nucleation site density and wall heat flux can also be approximated by a power law function. For the copper surface, an approximate correlation is obtained as,

$$N_a = 2.8031\times10^{-7}\left(q''\right)^{2.8193} \tag{4-5}$$

or,

$$q'' = 210.93N_a^{\,0.3547} \tag{4-6}$$

with most of the data within an approximate ±25% deviation. For the stainless steel surface, the measured nucleation site density data can be correlated with wall heat flux as,

$$N_a = 2.7231\times10^{-9}\left(q''\right)^{3.2863} \tag{4-7}$$

or

$$q'' = 403.92N_a^{\,0.3043} \tag{4-8}$$

with most of the data within an approximate ±50% deviation. A similar relationship between wall heat flux and nucleation site density was also obtained by Gaertner and Westwater (Gaertner and Westwater 1963), Wang and Dhir (Wang and Dhir 1993a), where the heat flux was found to be approximately proportional to the square root of the nucleation site density.

Heating surface materials used in the current study include copper and stainless steel, which have sharply different thermal conductivities and thermal diffusivities. For example, at 100ºC, the thermal conductivities of copper and stainless steel are 400 and 16.2 W/m·K, respectively, and the thermal diffusivities are $1.16\times10^{-4}$and 4.05×10^{-6}m^2/s, respectively. To examine the nucleation site density on heating surfaces with different thermal diffusivity, the measured data for both copper and stainless steel heating surfaces are plotted against critical cavity size and wall heat flux in Figures 4.9 and 4.10, respectively. As discussed above, nucleation site density can be correlated with critical cavity size with a power function. However, in Figure 4.9, nucleation site density data of these two materials do not merge into a single line, and the copper surface has a lower nucleation site density for the same critical cavity size (or the same wall superheat if pressure is fixed). It can also be observed that the curve for copper has a slope larger than for stainless steel. Eventually, at a smaller critical

cavity size (or high wall superheat), the copper heating surface will have a higher nucleation site density. This trend agrees with boiling performance measurements that, at higher wall superheat, the wall heat flux is higher for the copper surface. (Details of flow boiling performance on both surfaces will be discussed in later sections). However, due to experimental limitations on direct observation, the nucleation site density data at higher wall superheat are not available. Figure 4.10 shows nucleation site density data on both copper and stainless steel heating surfaces against the wall heat flux. The stainless steel surface shows a slightly higher nucleation site density at relatively higher heat flux. Nevertheless, most of the measured data from these two heating surfaces collapse onto a single line. This is so far the best correlating parameter for comparing wall superheat and critical cavity diameter, with nucleation site density data. As shown in Figure 4.10, nucleation site density data can be correlated with wall heat flux as,

$$N_a = 7.7137 \times 10^{-9} \left(q''\right)^{3.1767} \tag{4-9}$$

or,

$$q'' = 357.94 N_a^{\ 0.3148} \tag{4-10}$$

with most of the data located within a ±60% deviation. The result indicates that boiling heat transfer capability is mainly determined by fluid properties. To transport a certain amount of energy, a certain number of bubbles have to be generated. However, this conclusion may only stand for materials on which a fluid shows similar wettability, such as the combination of R134a on copper or stainless steel surfaces. The contact angles of R134a on copper and stainless steel surfaces show almost identical behavior. This has been experimentally observed and will be discussed in later sections. Experimental evidence (Phan et al. 2009a and 2009b) shows that on heating surfaces with greatly different surface wettabilities, the bubble dynamics and boiling behaviors also have significantly different characteristics. On a hydrophobic surface, bubbles tend to initiate at a relatively lower wall superheat. Also due to poor liquid wettability, bubbles tend not to detach from the heating surface while they coalesce with adjacent bubbles. On the contrary, on a hydrophilic surface, bubbles tend to

form into a spherical shape with relatively larger radii and lower departure frequencies. Wang and Dhir's study (Wang and Dhir 1993a) shows that, on heating surfaces made of the same material but with different wettability, the surface with higher wettability has a lower nucleation site density.

In this study, experimental results show that the nucleation site density can be correlated with wall superheat in a power law relation for a given pressure on a specific heating surface material, and the nucleation site density is higher for a higher pressure. To eliminate the pressure effect, the critical cavity diameter and the wall heat flux are used to correlate with the nucleation site density as suggested by Griffith. Nucleation site density data obtained at different pressures correlates well with critical cavity size or wall heat flux with power law relations. Compared to the critical cavity diameter, the wall heat flux shows better correlation behavior with nucleation site density on both heating surfaces. However, it has to be noticed that, the good correlation between nucleation site density and wall heat flux may only hold for materials which have similar surface wettabilities, such as the combination of R134a and a copper or stainless steel surfaces.

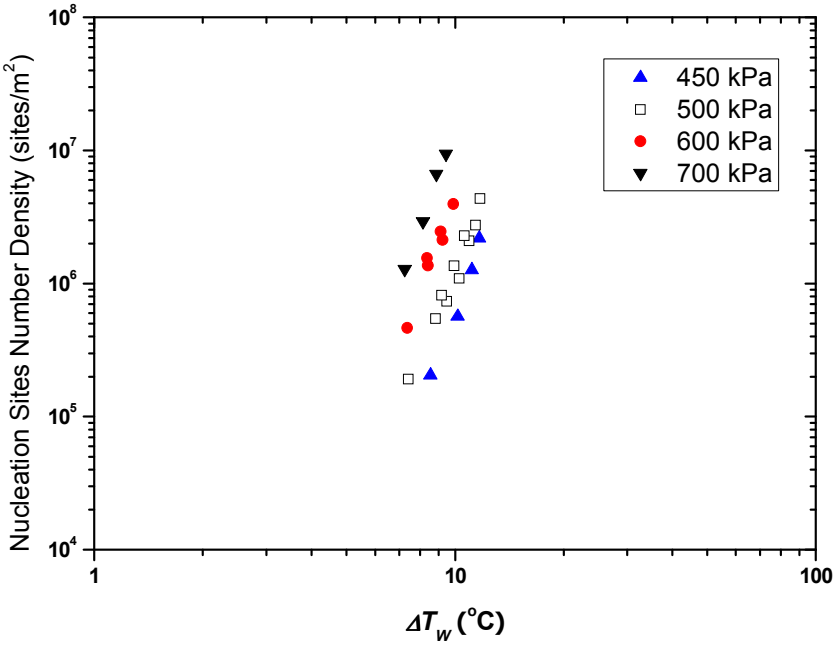

Figure 4.3. Nucleation site density against wall superheat for copper heating surface at different system pressures.

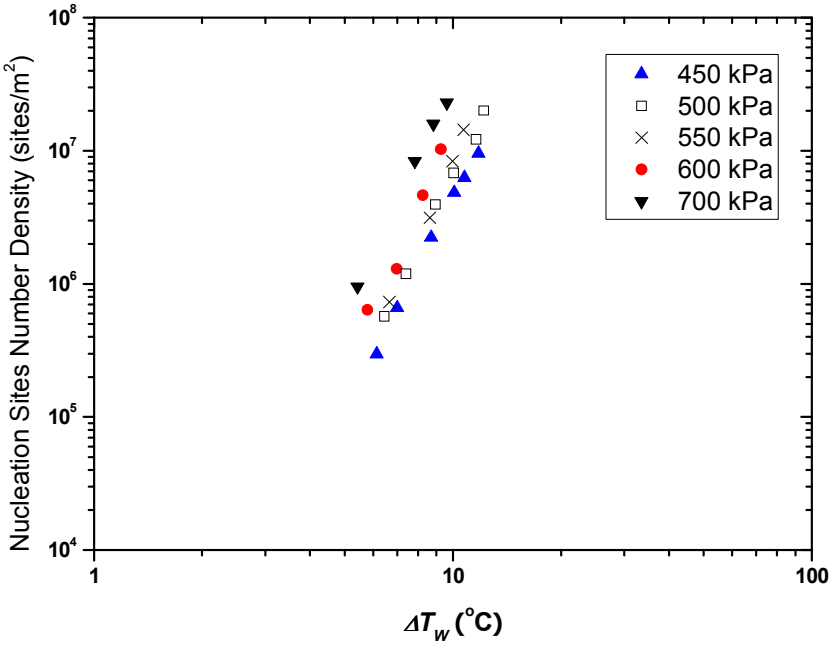

Figure 4.4. Nucleation site density against wall superheat for the stainless steel heating surface at different system pressures.

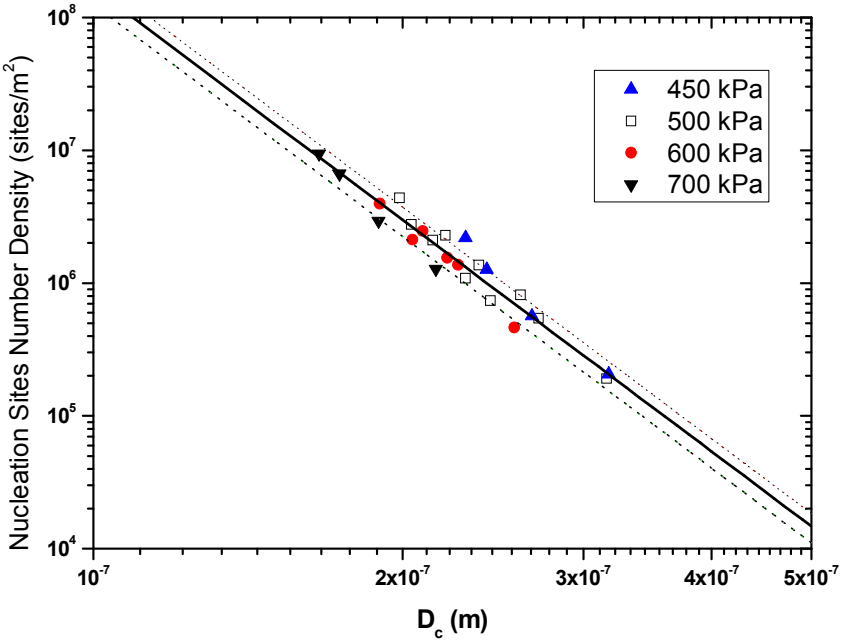

Figure 4.5. Nucleation site density against critical cavity diameter for the copper heating surface at different system pressures.

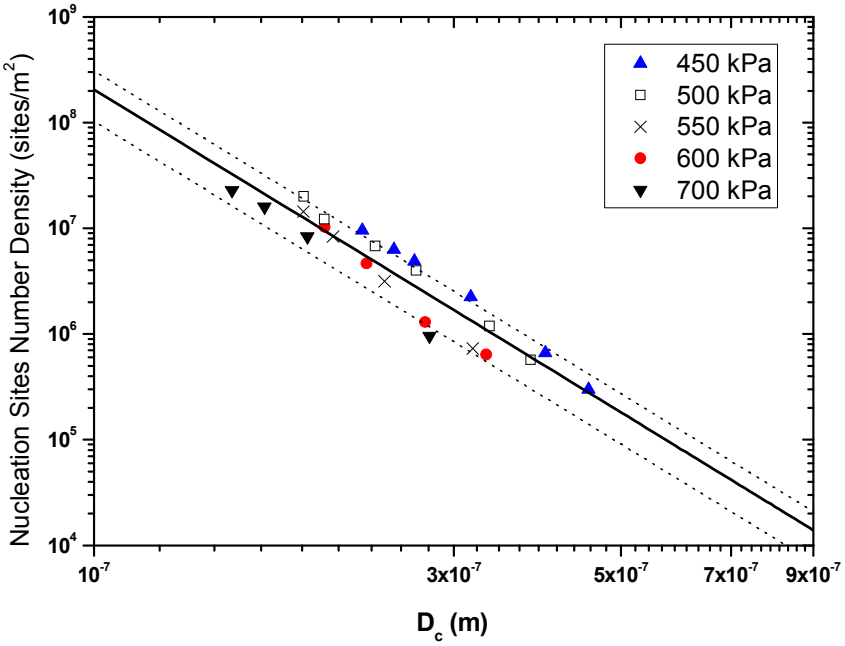

Figure 4.6. Nucleation site density against critical cavity diameter for the stainless steel heating surface at different system pressures.

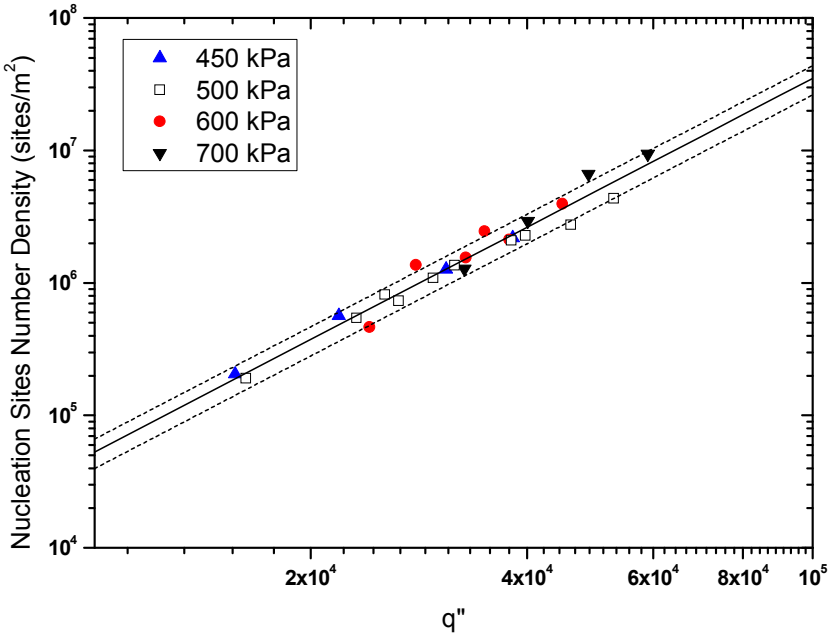

Figure 4.7. Nucleation site density against wall heat flux for the copper heating surface at different system pressures.

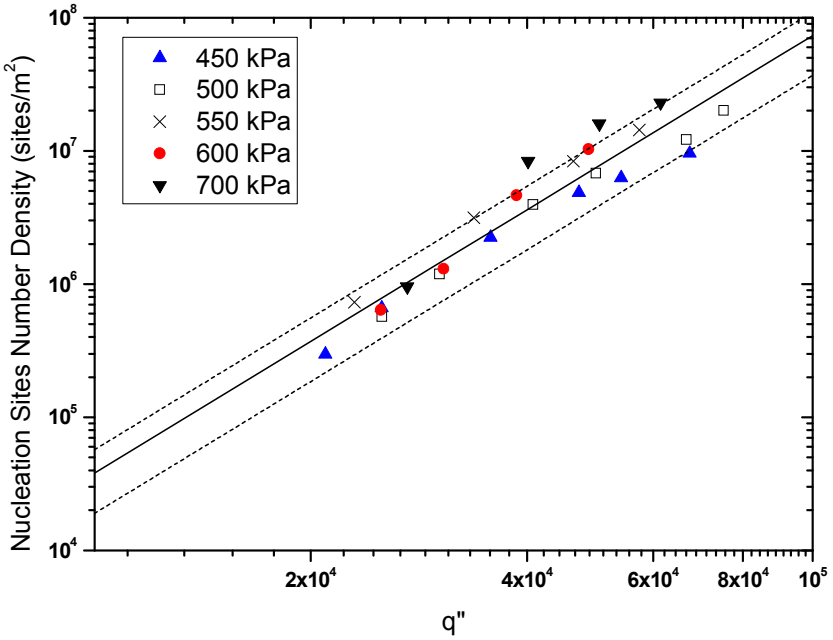

Figure 4.8. Nucleation site density against wall heat flux for stainless steel heating surface at different system pressures.

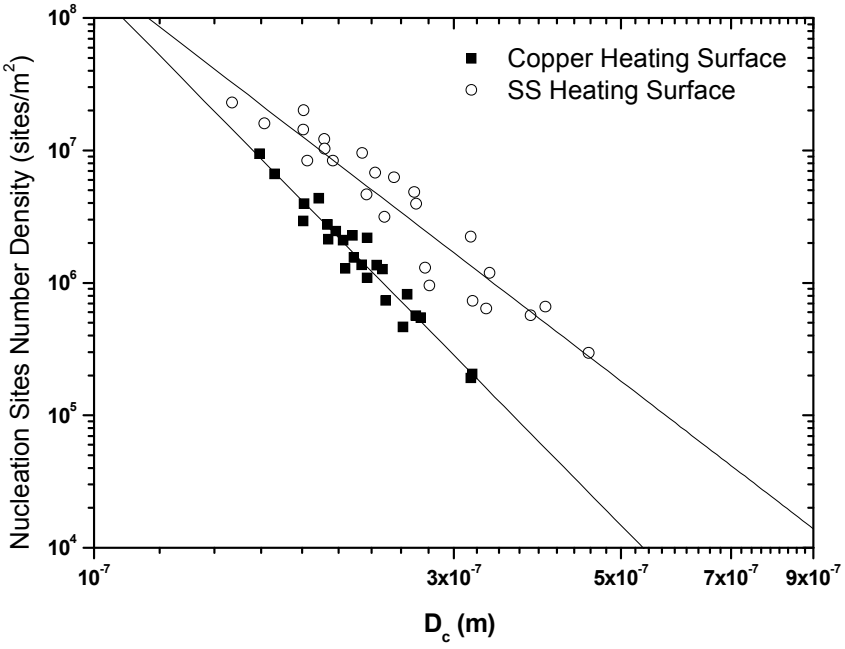

Figure 4.9. Nucleation site density against critical cavity diameter for both copper and stainless steel heating surfaces.

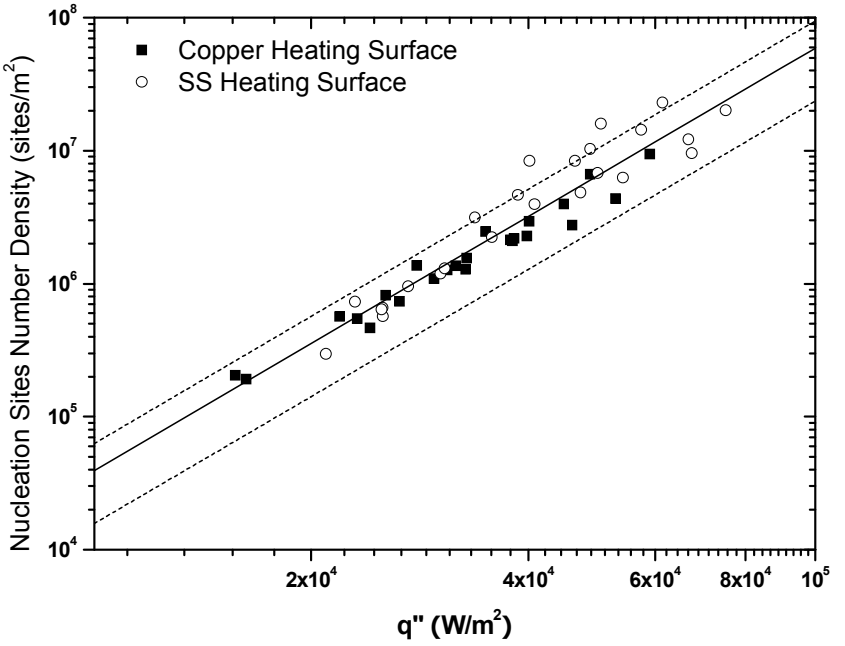

Figure 4.10. Nucleation site density against wall heat flux for both copper and stainless steel heating surfaces.

4.1.2 Nucleation site distribution

Early studies have shown that the nucleation site activation is mainly controlled by local wall superheat and surface characteristics, such as cavity size, shape and angle. Both heating surfaces used in the current study were polished with the same sandpaper (#600) and were then naturally oxidized by long time air exposure. It's expected that the cavities follow a spatial random distribution, and therefore the active nucleation sites follow a similar distribution. Nucleation site distribution data were obtained for both copper and stainless steel heating surfaces at different system pressures and wall superheat levels. The size of the observable domain, which was recorded by the high-speed digital camera, is in an area magnitude of several millimeters by several millimeters, depending on the camera magnification used. Normally the number of nucleation sites in such an observable domain is in the range of tens to hundred, depending on the wall superheat level. Figures 4.1 to 4.2 in the previous section have shown typical nucleation site distributions on the copper heating surface. Direct observation suggests that nucleation site distributions are fairly random and uniform. To statistically examine the nucleation site distribution, the domain is divided into identical sub-domains. Numbers of nucleation sites are counted in each of these sub-domains, schematically shown in Figure 4.11. The statistical probability density can be calculated as a fractional ratio of number of sub-domains having *Na* nucleation sites to the total number of sub-domains,

$$P(Na) = \frac{N(Na)}{N_{total}} \tag{4-11}$$

where, *N(Na)* is the number of sub-domains having *Na* nucleation sites, and N_{total} is the total number of sub-domains. In this study, to estimate the sites distribution, the observable domain is divided into 4×4 and 8×8 sub-domains. The estimated discrete probability densities are also compared with the discrete spatial Poisson distribution, defined as,

$$P(Na) = \frac{e^{-\overline{Na}}\left(\overline{Na}\right)^{Na}}{(Na)!} \tag{4-12}$$

where, $\overline{Na}$ is the average number of nucleation sites in a sub-domain. Figures 4.12 to 4.19 show typical distributions of nucleation sites on both copper and stainless steel surfaces, their corresponding discrete probability densities, and comparisons with the spatial Poisson distribution. The comparisons show that the calculated nucleation site distribution probability densities agree pretty well with the spatial Poisson distribution. However, there is a general trend that the calculated probability density for *Na* close to its average value, $\overline{Na}$, and is higher than that given by the spatial Poisson distribution. For example, as shown in Figure 4.13 for the copper heating surface with 10.94 ºC wall superheat at 500kPa, the average number of nucleation sites in a sub-domain are 4.8 and 1.2 for 4×4 and 8×8 patterns, respectively. The calculated probabilities from experimental data (*Na*=1 for 4×4 sub-domains, and *Na*=5 for 8×8 sub-domains) are both significantly larger than values given by the spatial Poisson distribution. This trend is observed for almost all conditions explored in the experiments. It indicates that the real nucleation site distribution observed during a flow boiling process is more uniform than the spatial Poisson distribution. To reveal more details of the distribution of nucleation sites, the distribution of the distance between two nearest adjacent nucleation sites, sometimes referred as 'nearest-neighbor distance', are examined. The distributions and their comparisons with the spatial Poisson distribution are shown in Figures 4.20 to 4.23. The distribution of the nearest-neighbor distance from the spatial Poisson distribution is given by,

$$P(S < S < S + ds) = 2\pi \overline{N} S e^{-\pi \overline{N} S^2} dS \tag{4-13}$$

with a mean value given by,

$$\overline{S} = \frac{1}{2} \overline{N}^{-1/2} \tag{4-14}$$

The most probable nearest-neighbor distance is given by,

$$S_{mp} = \frac{1}{\sqrt{2\pi}} \overline{N}^{-1/2} \tag{4-15}$$

From Figures 4.20 to 4.23, it can be found that the probability of the nearest-neighbor distance being located between 0 and a certain cut-off value is much smaller than that given by a Poisson spatial distribution. However, an opposite trend is found as the nearest-neighbor distance is close the mean distance value given by equation (4.14). These results lead to the same conclusion drawn previously: the real nucleation site distribution is more uniform than the Poisson spatial distribution. The observed nucleation site distribution phenomenon indicates there is a mechanism that nucleation sites are self-organized to cover as much heating area as possible to obtain a maximum boiling heat transfer capability. A possible reason for this self-organization behavior is nucleation site interactions. In general, nucleation site interactions can be divided into two major categories; fluid-side interactions and solid-side interactions. The fluid-side interactions include acoustic waves emitted by a growing bubble (Chekanov 1977), sites activation/deactivation by an adjacent bubble (Judd and Lavdas 1980), bubble coalescence (Mosdof and Shoji 2004), etc. The solid-side interaction is mainly thermal interactions between an active site and adjacent sites inside the solid heating surface. During a bubble growth, the local wall temperature near an active site drops dramatically due to liquid evaporation, serving as a heat sink. Consequently, in a certain bubble influence area, the wall temperature drops to a level which is lower than the required value to activate a bubble. This influence area is expected to be controlled by the thermal properties or, more specifically, the thermal diffusivity of the heating surface. If assuming a similar bubble behavior, a material with higher thermal diffusivity tends to have a larger influence area. The statistical behavior of the nearest-neighbor distance of both copper and stainless steel surfaces are compared in Figure 4.24, in terms of the coefficient of variance, which is defined as the ratio of standard deviation to the mean value. Figure 4.24 shows a trend that the nearest-neighbor distance on the copper surface generally has a smaller coefficient of variance, which indicates the nucleation site distribution is more uniform than that on the stainless steel surface. It can also be found from Figure 4.24 that the coefficient of variance tends to decrease as nucleation site density increases or, in other words, the distribution of sites is more uniform at higher nucleation site density.

As a summary, the nucleation site density has been experimentally studied and measured for both copper and stainless steel surfaces by high-speed visualization techniques with relatively low wall superheat, due to experimental limitations. The nucleation site density data were correlated with the wall superheat, critical cavity size and wall heat flux. All show good correlation with nucleation site density data. However, the wall superheat is not able to be correlated with the nucleation site density data for different system pressures. This then leads to a new correlating parameter, critical cavity size to account for the pressure effect. Again, the critical cavity size does not achieve success in correlating the data for both surfaces. The wall heat flux, however, shows a good correlation with the nucleation site density data for both surfaces. The measured nucleation site density data are also compared with a Poisson spatial distribution. The measured data show good agreement with the Poisson spatial distribution by counting nucleation site numbers in sub-domains. However, the comparison of the distribution of nearest-neighbor distance indicates the real nucleation site has a more uniform distribution than the Poisson spatial distribution. In addition, the copper surface has a more uniform distribution than the stainless steel surface, which may be explained by the nucleation sites thermal interactions.

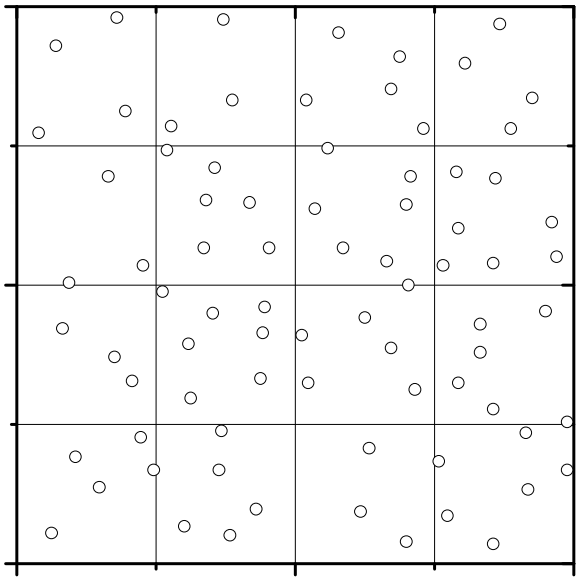

Figure 4.11. A typical nucleation sites distribution on the copper surface.

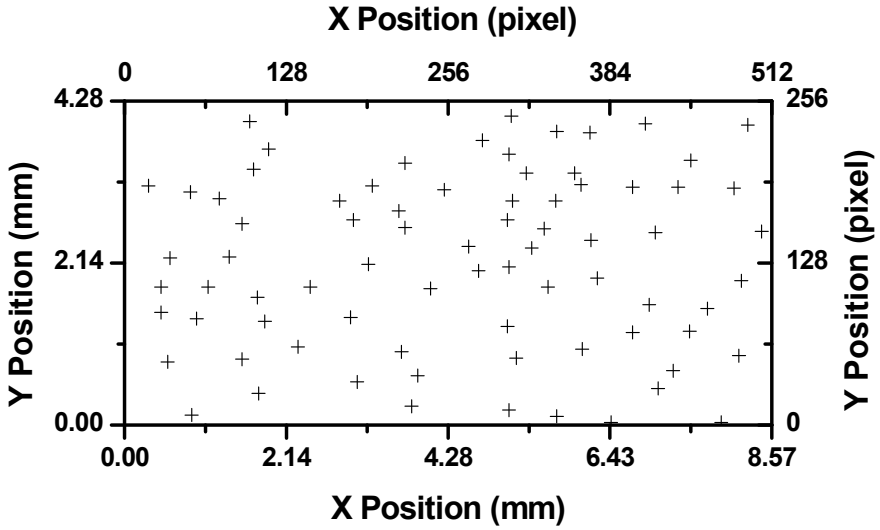

Figure 4.12. Nucleation sites on the copper surface at pressure of 500 kPa and wall superheat of 10.94 ºC.

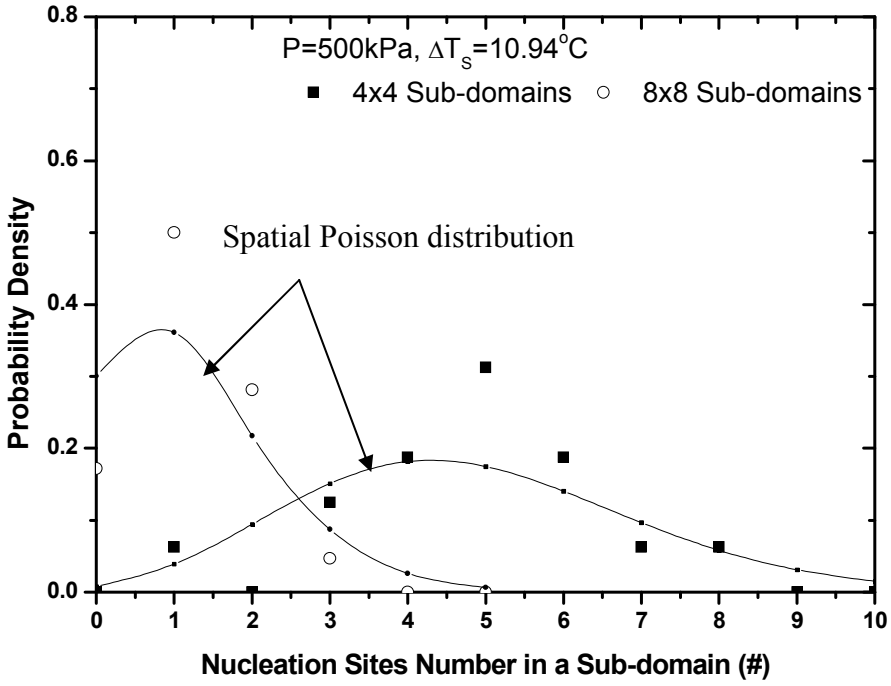

Figure 4.13. The discrete probability density of nucleation sites distribution on a copper surface at pressure of 500 kPa and wall superheat of 10.94 ºC, and its comparison with the spatial Poisson distribution.

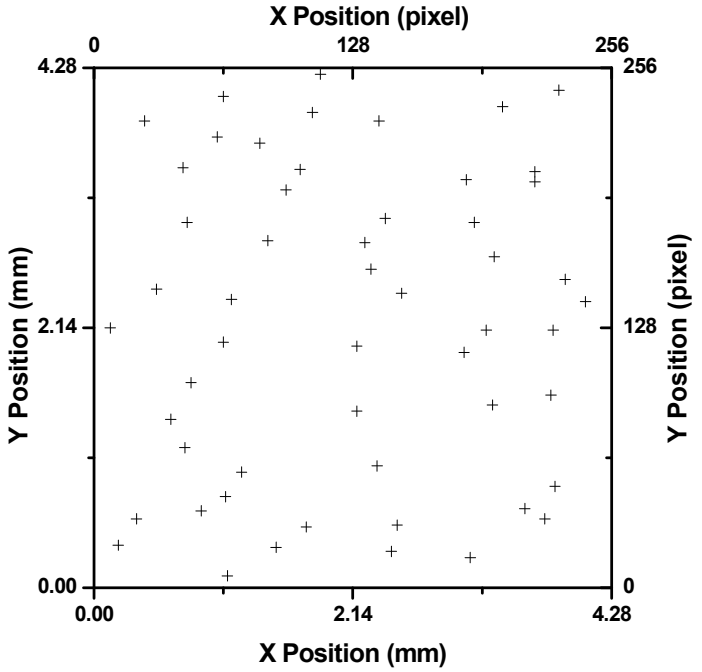

Figure 4.14. Nucleation sites on the copper surface at pressure of 700 kPa and wall superheat of 8.15 ºC

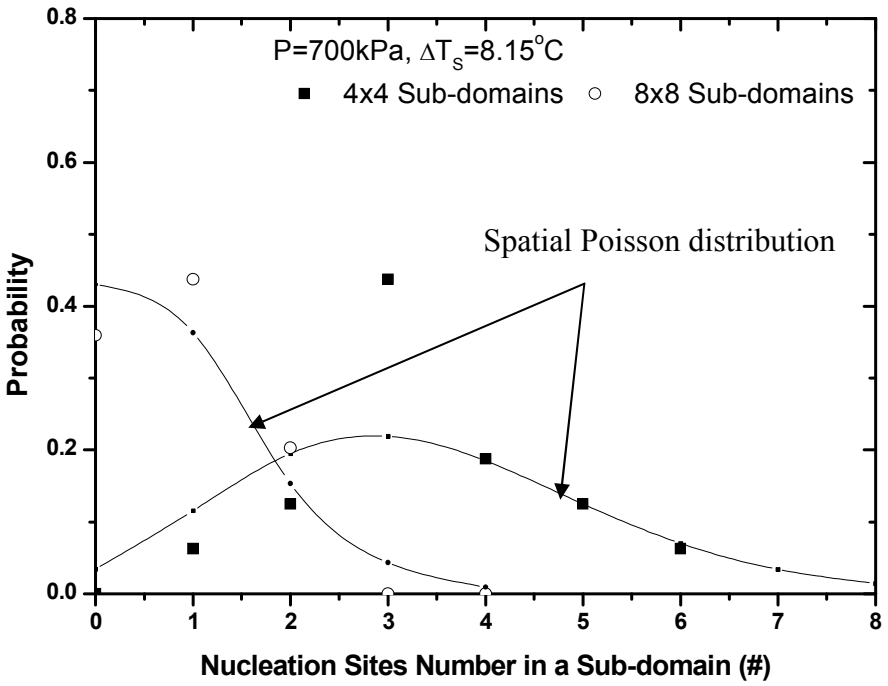

Figure 4.15. The discrete probability density of nucleation sites distribution on the copper surface at pressure of 700 kPa and wall superheat of 8.15 ºC, and its comparison with the spatial Poisson distribution.

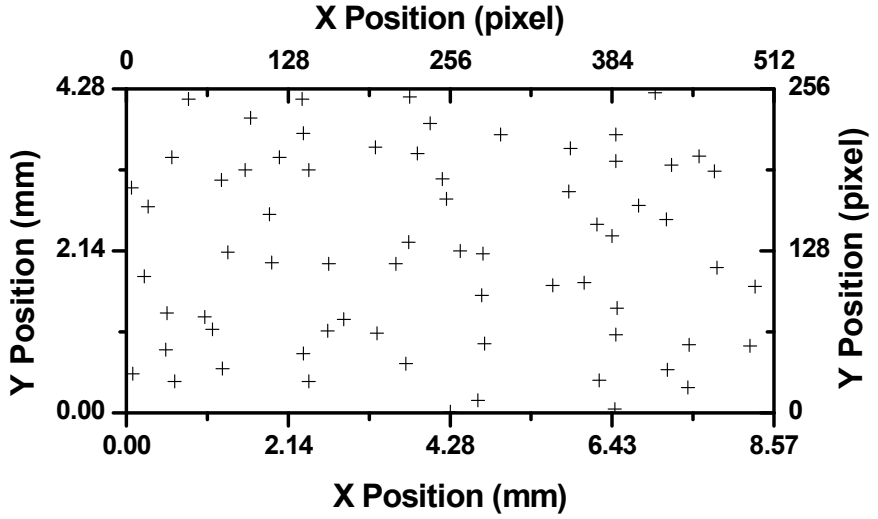

Figure 4.16. Nucleation sites on the stainless steel surface at pressure of 450 kPa and wall superheat of 10.09 ºC.

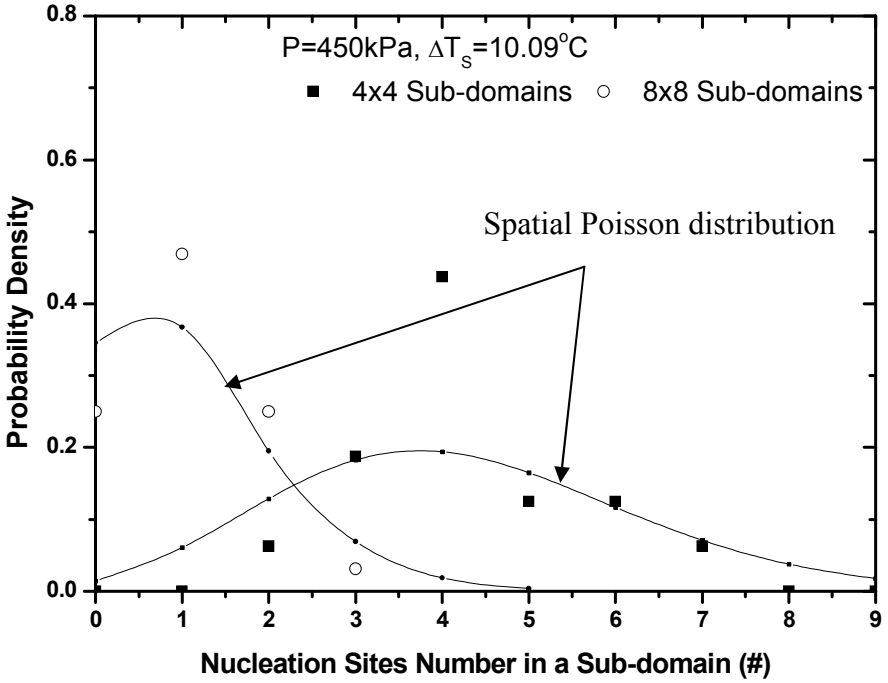

Figure 4.17. The discrete probability density distribution of nucleation sites on the stainless steel surface at pressure of 450 kPa and wall superheat of 10.09 ºC, and its comparison with the spatial Poisson distribution.

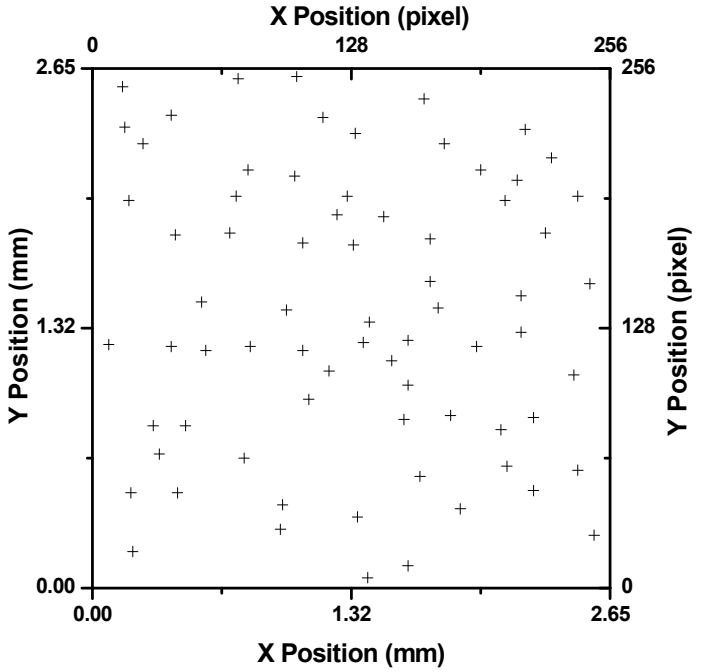

Figure 4.18. Nucleation sites on the stainless steel surface at pressure of 600 kPa and wall superheat of 9.26 ºC.

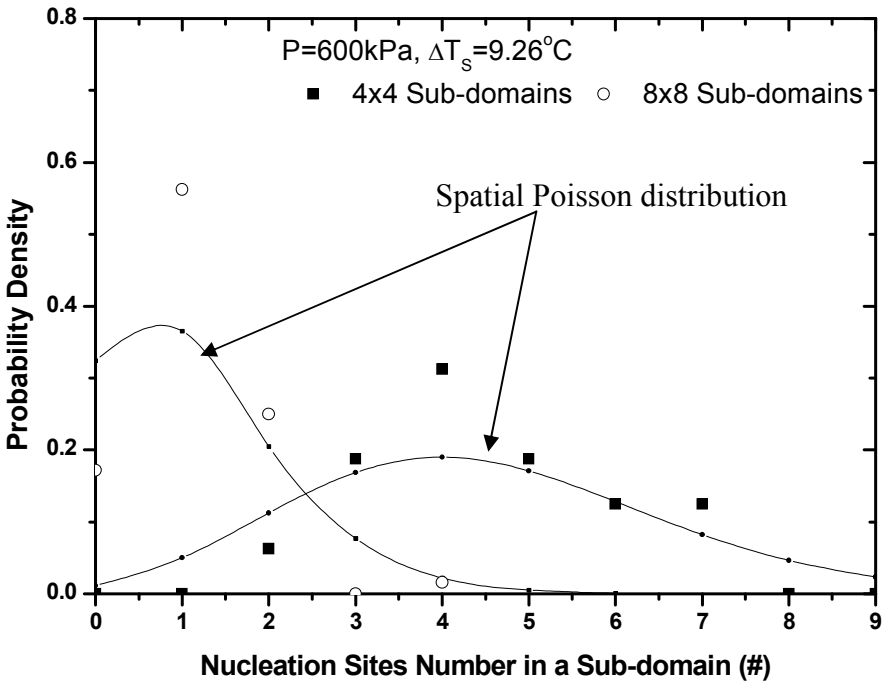

Figure 4.19. The discrete probability density of nucleation sites distribution on the stainless steel surface at pressure of 600 kPa and wall superheat of 9.26 ºC, and its comparison with the spatial Poisson distribution.

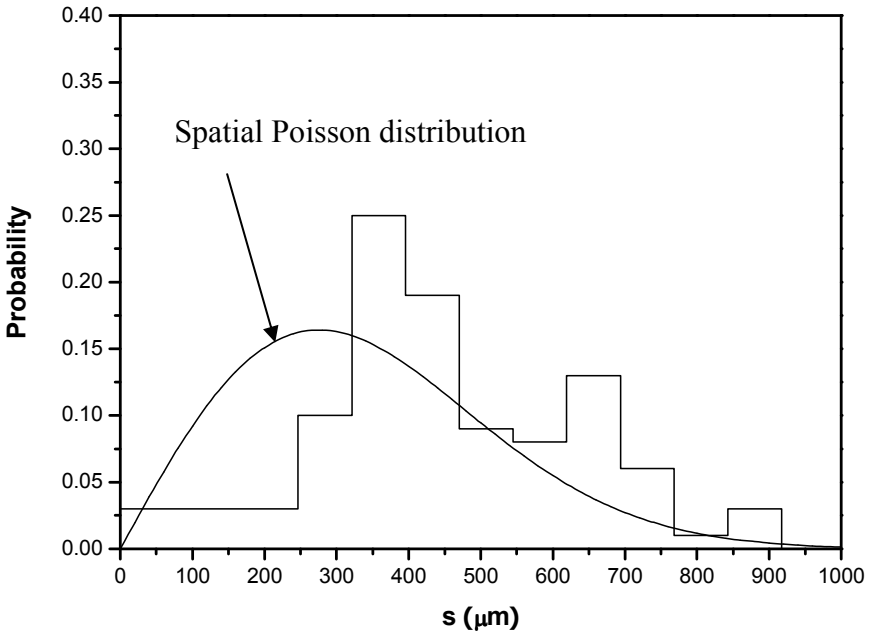

Figure 4.20. The probability density of nearest-neighbor nucleation sites distance and its comparison with the spatial Poisson distribution, on the copper surface, pressure of 500 kPa and wall superheat at 10.94 ºC.

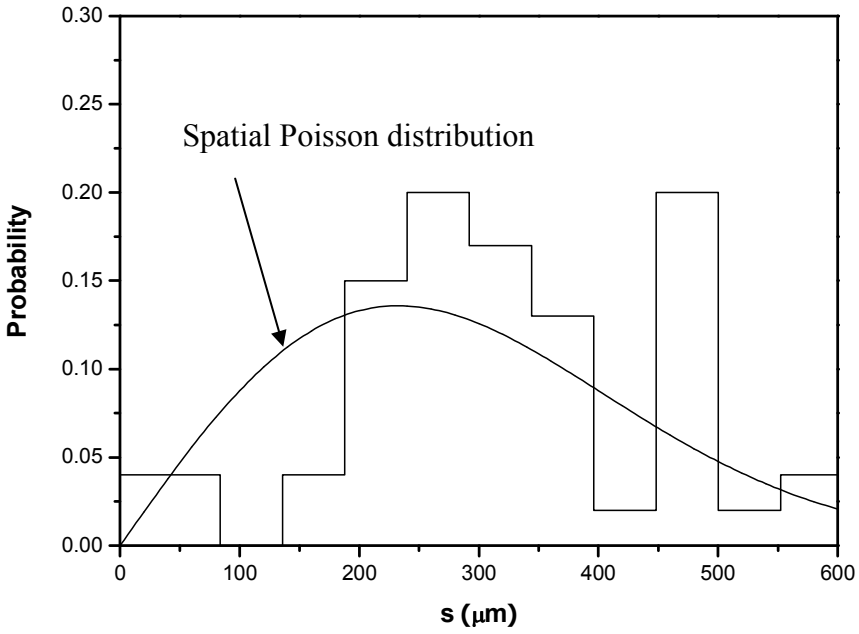

Figure 4.21. The probability density of nearest-neighbor nucleation sites distance and its comparison with the spatial Poisson distribution, on the copper surface, pressure of 700 kPa and wall superheat at 8.15 ºC.

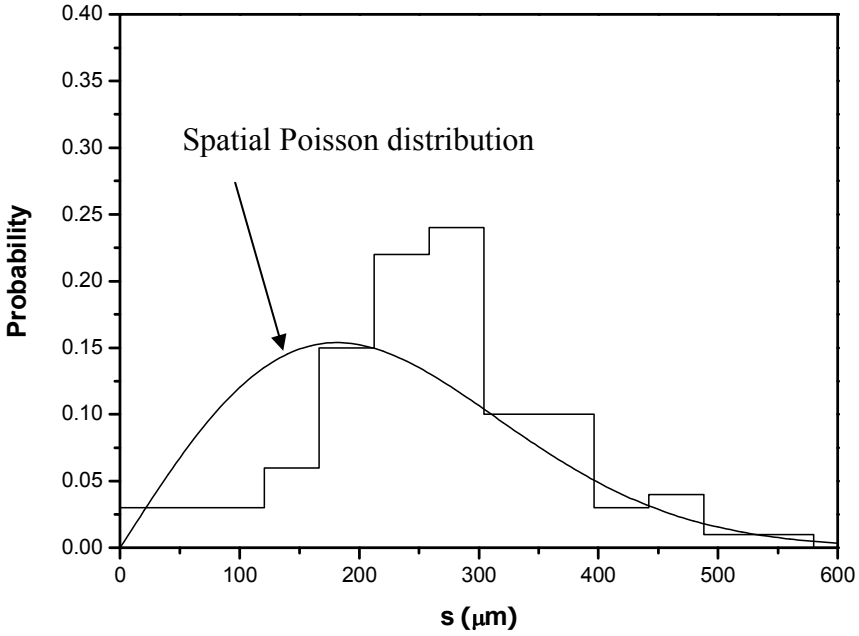

Figure 4.22. The probability density of nearest-neighbor nucleation sites distance and its comparison with the spatial Poisson distribution, on the stainless steel surface, pressure of 450 kPa and wall superheat at 10.09 ºC.

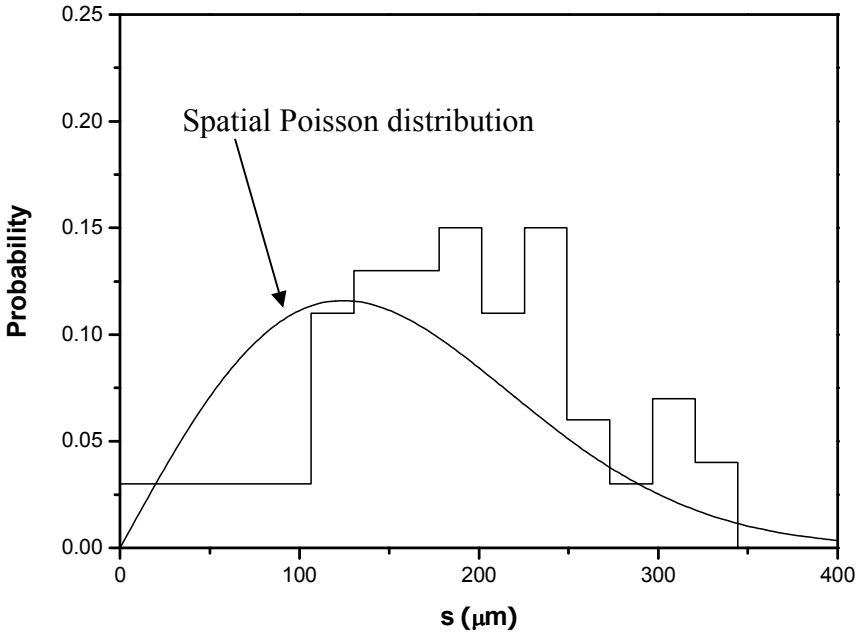

Figure 4.23. The probability density of nearest-neighbor nucleation sites distance and its comparison with the spatial Poisson distribution, on the stainless steel surface, pressure of 600 kPa and wall superheat at 9.26 ºC.

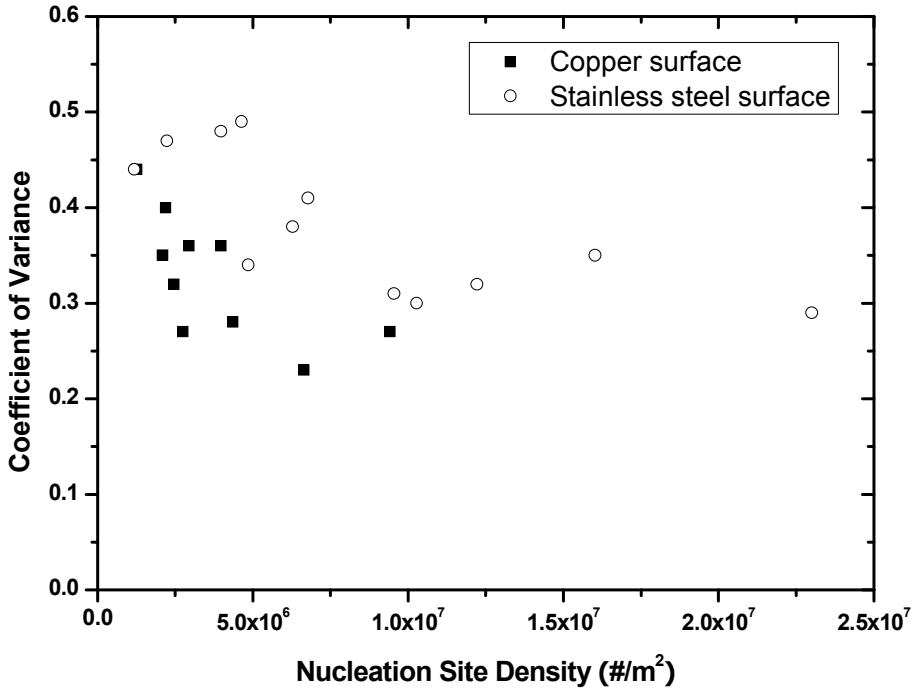

Figure 4.24. Coefficient of variance of the measured nearest-neighbor nucleation sites distance for both copper and stainless steel surfaces.

4.2 BUBBLE DYNAMICS

Bubble dynamics is a wide topic in boiling processes, especially in flow boiling due to its complexity and nonlinearity. In flow boiling, during the lifespan of a vapor bubble, it starts from an embryo and then grows into an active nucleation site. After reaching a certain size, it departs and then slides from the original site. A sliding bubble generally coalesces with a bubble downstream and lifts-off into the bulk flow. If heat fluxes are low, a sliding bubble may not have a chance to coalesce before it lifts-off. On the contrary, bubbles coalescence can happen before a bubble starts to slide due to high bubble number density. There are also intense interactions between bubbles and nucleation sites. A nucleation site can be activated or deactivated by an adjacent bubble or bubbles sliding from upstream, which occasionally cover the site. Bubble contact angle, or surface wettability has also been proved

to have significant impact on bubble behaviors and consequently boiling heat transfer. A high-speed digital camera was used to visually study the bubble dynamics during the current flow boiling experiments. However, due to the stochastic nature of fluid flow and boiling heat transfer, scattered data are expected.

4.2.1 Contact angle and bubble shape

In the current study, the same working fluid, R134a was boiled on two different heating surfaces at different system pressures. As is generally known, contact angle has an effect on bubble behavior and even nucleation site density. This then leads to a different boiling performance on different heating surface materials. It's generally accepted that heating surfaces with different surface wettabilities, such as hydrophobic and hydrophilic surfaces, have distinctive bubble dynamics and boiling performances. In the current study, a copper and a stainless steel surface are not expected to have significantly different values of surface wettability. However, to examine the potential effect of wettability, the contact angles of R134a on both copper and stainless steel surfaces, and also at different system pressures, were studied.

Contact angle is generally affected by the solid-liquid combination, system pressure and surface roughness. Like most liquids, R134a vapor-liquid surface tension decreases with pressure. For example, the surface tension at 700kPa is around 30% lower than that at 400kPa. In addition, wettabilities of the heating surface materials studied, copper and stainless steel, have potential impact on the contact angle. To avoid surface roughness effect on boiling heat transfer, both heating surfaces were prepared with the same surface finish, e.g., polished by identical #600 sand papers and then long air exposure time to have similar oxidation level.

Theoretically, the contact angle between liquid-vapor interfaces and an ideally flat solid surface can be calculated from a force balance at the solid-liquid-vapor three-phase line provided by Young's equation, shown in Figure 4.25 ,

$$\cos\theta = \frac{\sigma_{sv} - \sigma_{sl}}{\sigma_{lv}} \qquad (4\text{-}16)$$

in which, σ_{sv}, σ_{sl} and σ_{lv} are solid-vapor surface, solid-liquid surface, and liquid-vapor surface tensions, respectively. Young's equation, however, requires the knowledge of solid-vapor and solid-liquid surface tensions, which are difficult to measure and normally unavailable. In equation (4-16), R134a liquid-vapor surface tension data are available for different pressures. However, without knowing the other two parameters, the prediction of the contact angle is not achievable by using Young's equation. Recent research (Wu et al. 2007) shows that the contact angle – pressure relation can be made explicit and that the contact angle normally increases with pressure, which has been experimentally proved. Another recent study (Vadgama and Harris 2007), however, shows that the pressure has a minor effect on the contact angle of R134a-copper surface combination. This experimental work has been done to specifically study the pressure effect on the contact angle of R134a on both aluminum and copper surfaces at different system pressures. Saturation temperature tested ranged from 0 ºC to 80 ºC, which corresponds to pressures from 0.3 MPa to 2.6 MPa. The contact angles were measured to be in the range of 5.1º to 6.5º, and there's no clear trend that the contact angle increases with pressure.

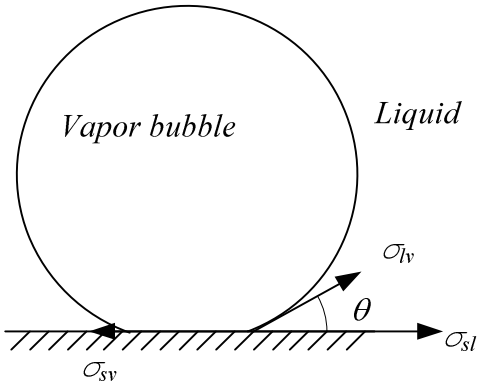

Figure 4.25. Schematic drawing of a bubble on heating surface.

With respect to contact angle, flow boiling has a distinct behavior which pool boiling does not have. For pool boiling, contact angle is normally treated as a constant value along the bubble-solid contact line due to the symmetry of stationary bubbles. In flow boiling,

before a bubble departs from its original site, it tends to be tilted with an inclination angle due to the relative velocity between the bubble and its surrounding fluid. The inclination level is determined by a force balance between the liquid drag force and the surface tension force. Thus, the contact angle of a bubble along the bubble-solid contact line is no longer a constant value. If a bubble is observed from a side view, perpendicular to the flow direction, contact angles can be observed to be different on the upstream and downstream sides of the bubble. The side facing the incoming flow has a larger contact angle, which is so-called advancing contact angle. The smaller one on the other side is called receding contact angle. After bubble departure, it tends to slide on the heating surface, traveling a certain distance before it lifts-off into the bulk flow or merges with a bubble downstream. During bubble sliding, the relative velocity between a sliding bubble and its surrounding liquid becomes much smaller and experimental evidence shows that the inclination angle is very small and can normally be negligible. The contact angle is a constant value along the bubble-solid contact line, so there's no net surface tension force in the flow direction.

Contact angles were measured during this study for both copper and stainless steel heating surfaces at different system pressures, ranging from 400kPa to 800kPa. The bulk liquid velocity tested was in the range of 0.05 m/s to 0.25 m/s. Figures 4.26 and 4.27 show typical bubble images taken from the copper and the stainless steel heating surfaces, respectively. On both surfaces, bubbles exhibit spherical shapes or ellipsoidal shapes close to spherical. Contact angles were obtained by measuring the angle between a tangent line of the bubble profile and the flat surface at the contact point. Figures 4.26 and 4.27 show that there is no significant difference in bubble shapes and contact angles between these two surfaces. However, it was found that the bubbles on the copper surface had a more spherical shape, as compared with that on the stainless steel surface. Contact angles at different pressures are plotted in Figure 4.28 for both surfaces. Both pressure and surface material do not show significant impacts on the contact angle. Contact angles on the copper surface were measured to range from 34º to 40º, with an average value of 38.4º. Contact angles on the stainless steel surface have slightly larger values, in the range of 40º to 44º, with an average value of 41.4º.

Bubble inclination angle was also visually examined from the images. It was found that the advancing contact angle and receding contact angle are nearly equal, indicating a fairly small inclination angle. As discussed above, the incline angle is a result of a force balance between the fluid drag force and the surface tension force. The fluid drag force is proportional to the local liquid velocity relative to the bubble. For a small bubble size in the magnitude of tens microns, the local liquid velocity is calculated to be very small so that the observed inclination angle is very small.

As a summary, bubble images studies showed that there was no significant difference between the copper heating and the stainless steel heating surfaces in terms of contact angle and bubble shape. Also, even the liquid-vapor surface tension changes with pressure, it was found that the system pressure did not have a significant impact on the contact angle. Bubble inclination angle was found to be fairly small.

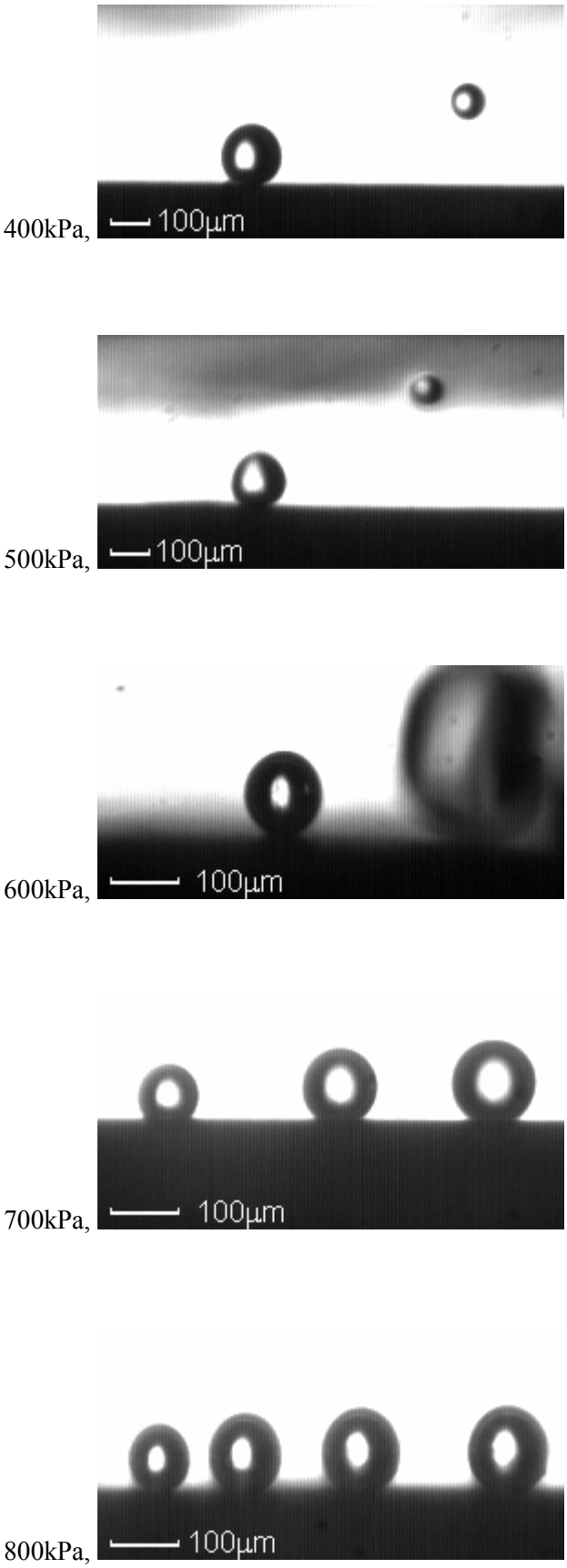

Figure 4.26. Typical bubble images on the copper surface at pressures from 400 to 800 kPa.

400kPa, 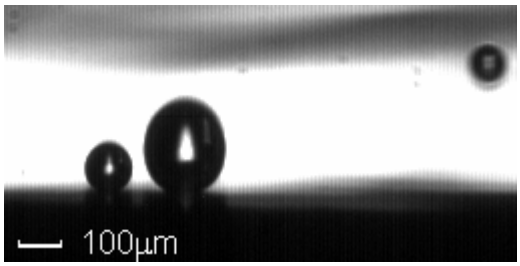

500kPa, 

600kPa, 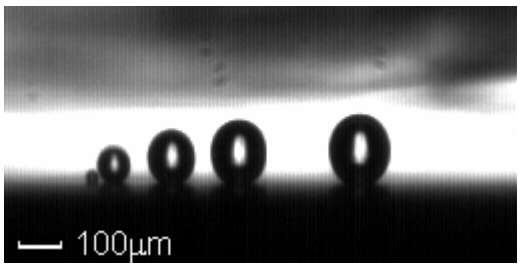

700kPa, 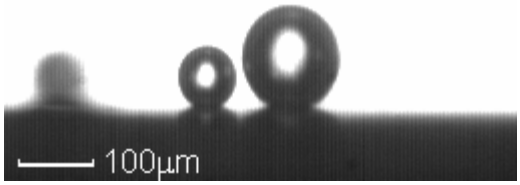

800kPa, 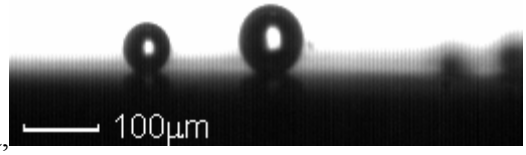

Figure 4.27. Typical bubble images on the stainless steel surface at pressures from 400 to 800 kPa.

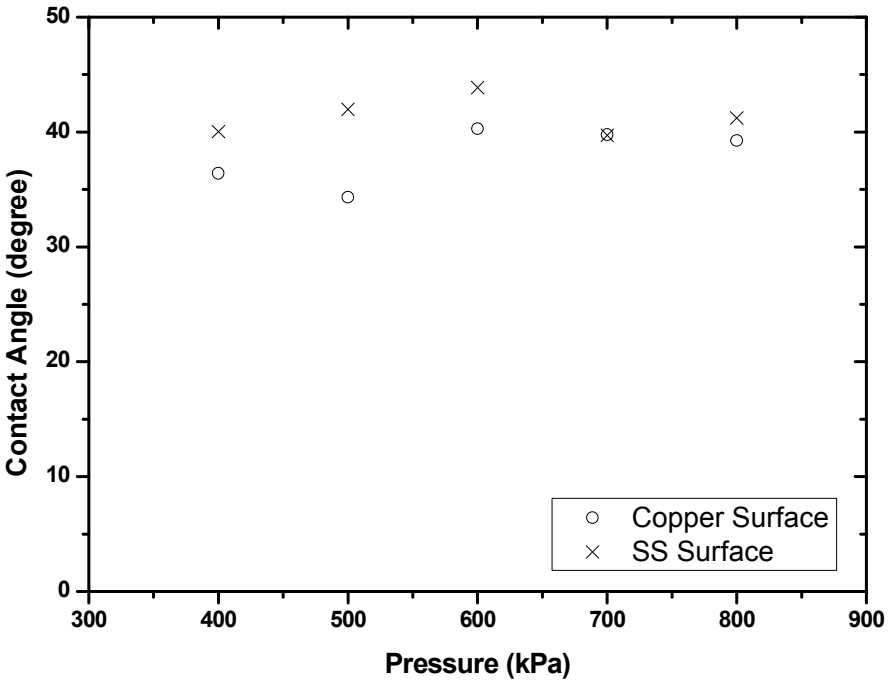

Figure 4.28. Bubble contact angles of both copper and stainless steel surfaces at different pressures.

4.2.2 Bubble growth rate and departure size

In flow boiling, the overall heat transfer consists of three major components, latent heat carried by vapor bubbles, transient conduction due to quenching effect on heating surface after bubble leaving, and single phase convection in areas without bubbles covering. A large portion of heat is transferred from the heating surface to the working fluid in the form of latent heat. Vapor bubbles serve as important media to transfer energy to the bulk flow as they carry latent heat and agitate the flow. Transient conduction is highly connected with bubble formation and departure. After bubble departure from its original site, bulk fluid with lower temperature fills the vacancy created by bubble departure, which was described as a "quenching" mechanism. The single phase convection is generally a small component compared to latent heat and transient conduction transfers. Especially in fully developed flow boiling regime, where most of the heating surface area is covered by bubbles, and leads to

diminished single phase convection. In flow boiling, bubble growth rate, departure diameter and waiting time are dominant parameters in determining how fast energy is transferred to the bulk flow.

Bubble growth has been studied by several researchers, including Rayleigh (Rayleigh 1917), Plesset and Zwick (Plesset and Zwick 1954), Zuber (Zuber 1961) and Mikic et al. (Mikic et al. 1970). Mikic concluded that, bubble growth normally experiences two stages, a very short inertia controlled stage at bubble initiation and a diffusion controlled stage thereafter. The bubble growth rate was visually measured in the current study. For R134a boiling with wall superheat in the magnitude of ten degrees, the inertia controlled stage is estimated to be much less than 1×10^{-9} seconds, which was not able to be captured by the high-speed camera used. All bubble images captured by the camera were considered to be in the thermal diffusion controlled stage. For bubbles in this stage, bubble radii have been observed to be proportional to $t^{1/2}$,

$$R_b \sim Ct^{1/2} \tag{4-17}$$

where, R_b is bubble radius, C is a constant and t is time.

Figure 4.29 and 4.30 show typical bubble images during growth on both copper and stainless steel heating surfaces, respectively. Figure 4.29 displays a growing bubble (bubble-1) on the copper heating surface with a wall superheat of 8.8 ºC, a system pressure of 400kPa and an average bulk liquid velocity at 0.09m/s. Figure 4.30 displays a growing bubble (bubble-2) on the stainless steel heating surface with a wall superheat of 7.3 ºC, a system pressure at 400kPa and an average bulk liquid velocity at 0.20m/s. The bubble radius was measured at each time step and plotted against the time in Figures 4.31 and 4.32 for bubble-1 and bubble-2, respectively. Zuber's model prediction wasalso plotted to compare with the experimental data. Zuber's model gives that,

$$R(t) = \frac{2b}{\sqrt{\pi}} Ja\sqrt{\alpha_l t} \tag{4-18}$$

where, b is a constant and Ja is the Jacob number. By comparing his experimental data with it, Zuber suggested the value of constant b to lie between 1 and √3. Comparisons for both bubbles indicate that the experimental data agrees well with Zuber's model with constant b equal to 1. To compare bubble growth rate for both copper and stainless steel heating surfaces, the bubble growth experimental data were fitted in the form of,

$$R(t) = C_b \frac{2b}{\sqrt{\pi}} Ja\sqrt{\alpha_l t} \tag{4-19}$$

using the least square method. In equation (4-19), C_b is an experimentally determined constant. The values of C_b for both heating surfaces at different system pressures are plotted in Figure 4.33. It was that most values of C_b are located between 0.75 and 1.25. The average values of C_b are 0.99 and 0.98 for the copper and the stainless steel surfaces, respectively. In addition, there's no significant difference on C_b found between these two surfaces. This indicates that Zuber's model is suitable for predicting bubble growth rates under flow boiling conditions for both surfaces. In Zuber's model, the bubble growth rate is only a function of liquid/vapor thermal properties and wall superheat. More importantly, the fact that Zuber's model works for two heating surfaces with widely different thermal conductivities and thermal diffusivities indicates that heating surface thermal properties do not play important roles in bubble growth rate.

The bubble waiting time can be estimated by counting the frame numbers between a departure bubble and a subsequent new embryo. From bubble images, most of the bubble waiting time was found to be within one frame interval at 4000 fps camera speed. The bubble's life time before departures normally lasts tens of frames, and the bubble waiting time is only a minor portion of a bubble's lifespan. It is noted that the bubble waiting time was measured at low wall superheat. The bubble waiting time for high wall superheat level is not available due to the limitation of the technology for reasons mentioned in the beginning of this chapter. Many researches (Han and Griffith, 1967; Podowski et. al., 1997; Basu et. al., 2005) have studied the bubble waiting time, and concluded that the bubble waiting time decreases with increasing wall superheat. Therefore, the bubble waiting time at higher wall

superheats is expected to be even smaller than that at low wall superheats. As a summary, the bubble frequency is largely determined by how fast a bubble grows and its departure size, while the bubble waiting time may be safely neglected.

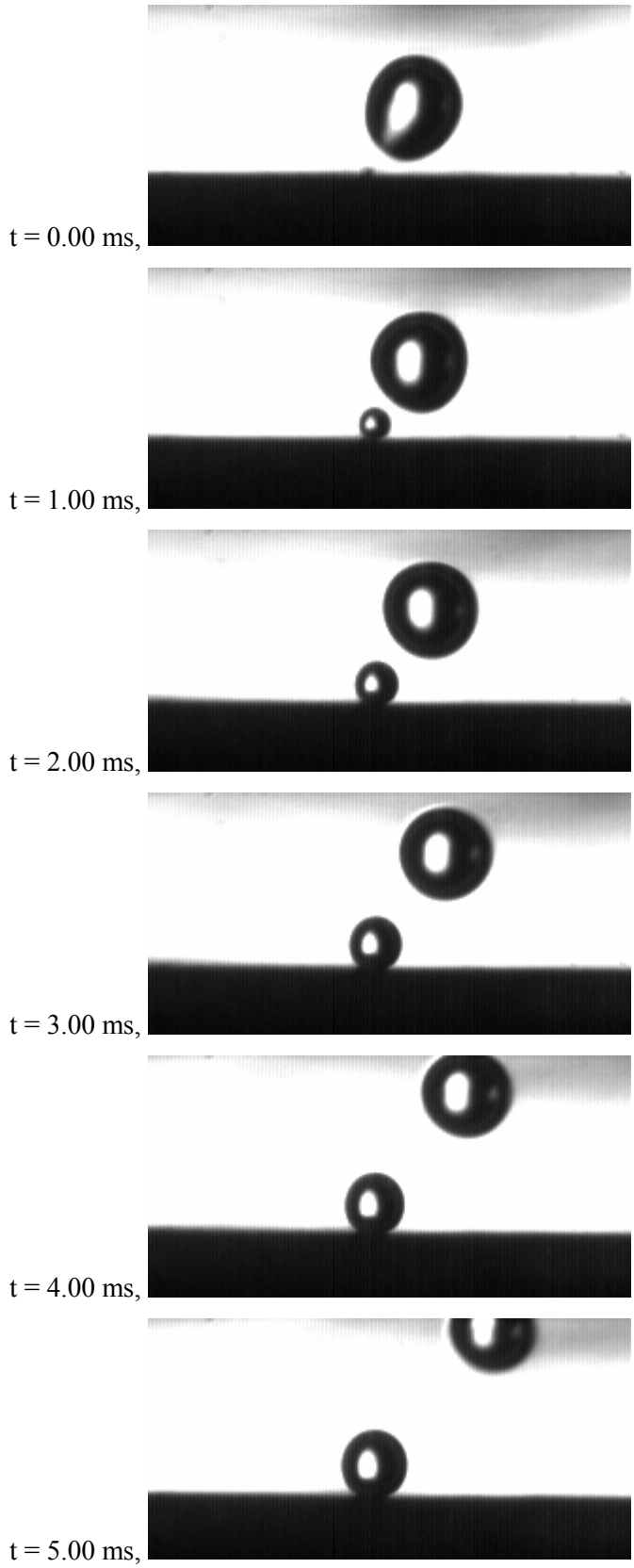

Figure 4.29. Typical bubble (bubble-1) growth images on the copper surface, 4000 fps, 400 kPa pressure, 8.8 ºC wall superheat, 0.09 m/s bulk flow velocity. Some frames have been omitted.

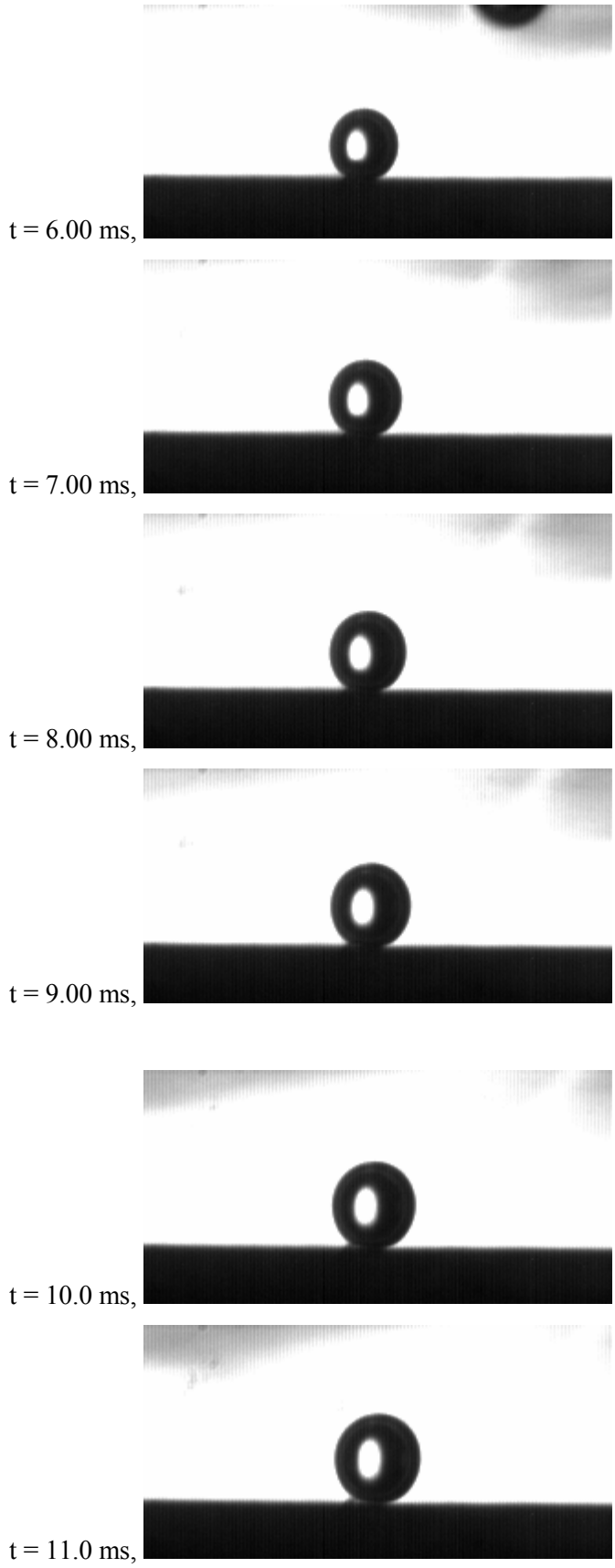

Figure 4.29. Typical bubble (bubble-1) growth images on the copper surface, 4000 fps, 400 kPa pressure, 8.8 ºC wall superheat, 0.09 m/s bulk flow velocity. Some frames have been omitted. (Continued)

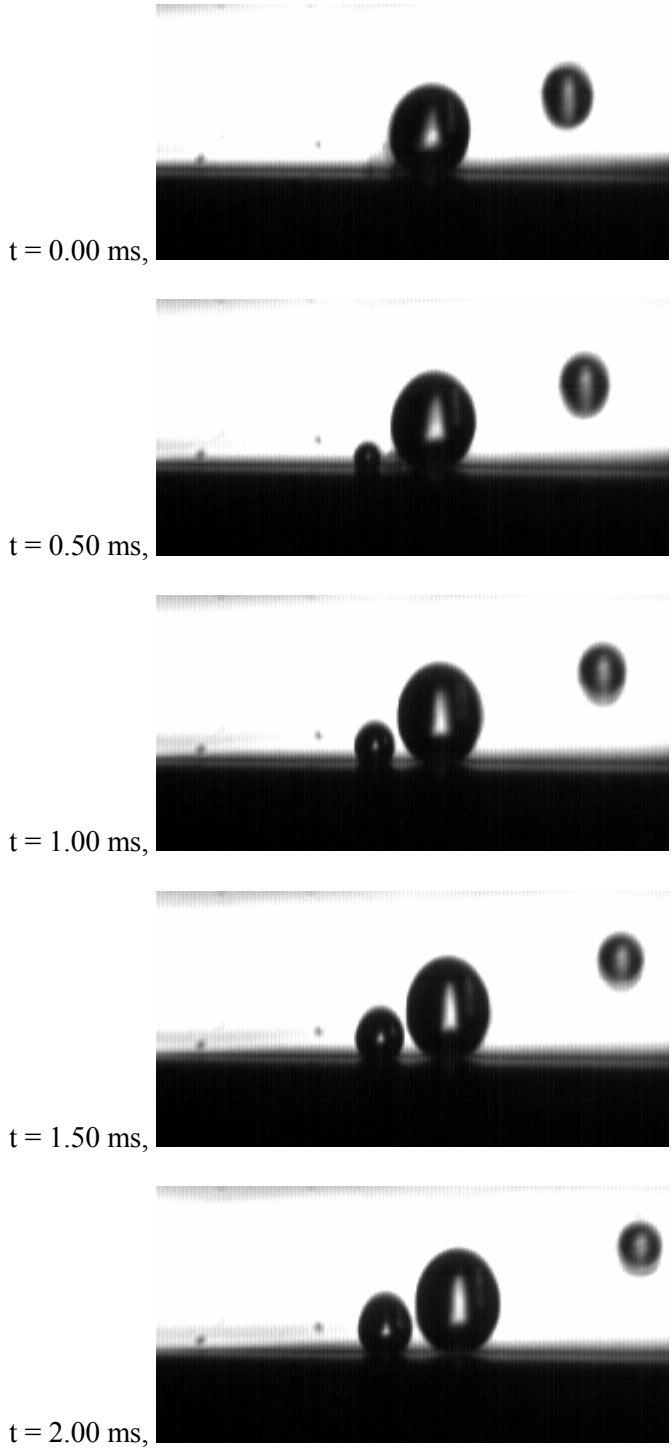

Figure 4.30. Typical bubble (bubble-2) growth images on a stainless steel surface, 2000 fps, 400 kPa pressure, 7.3 ºC wall superheat, 0.20 m/s bulk flow velocity. Some frames have been omitted.

t = 2.50 ms, 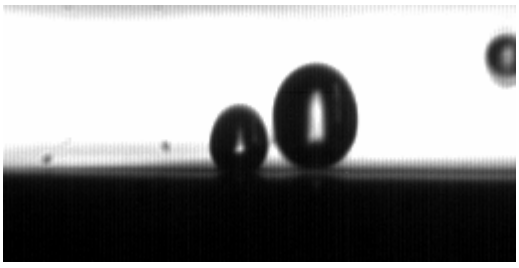

t = 3.00 ms, 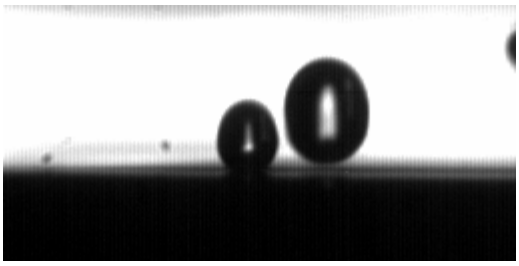

t = 3.50 ms, 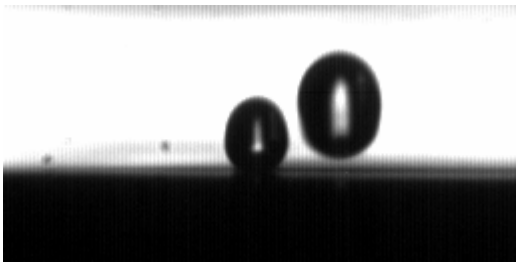

t = 4.00 ms, 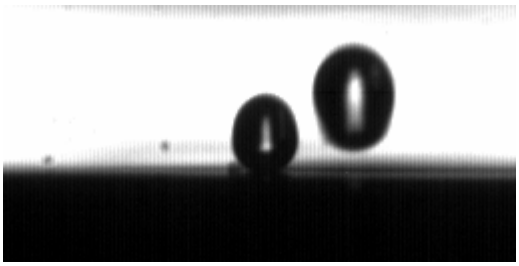

t = 4.50 ms, 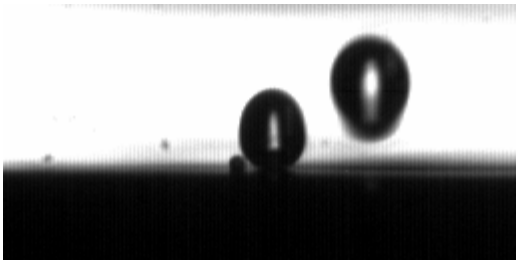

Figure 4.30. Typical bubble (bubble-2) growth images on a stainless steel surface, 2000 fps, 400 kPa pressure, 7.3 ºC wall superheat, 0.20 m/s bulk flow velocity. Some frames have been omitted. (Continued)

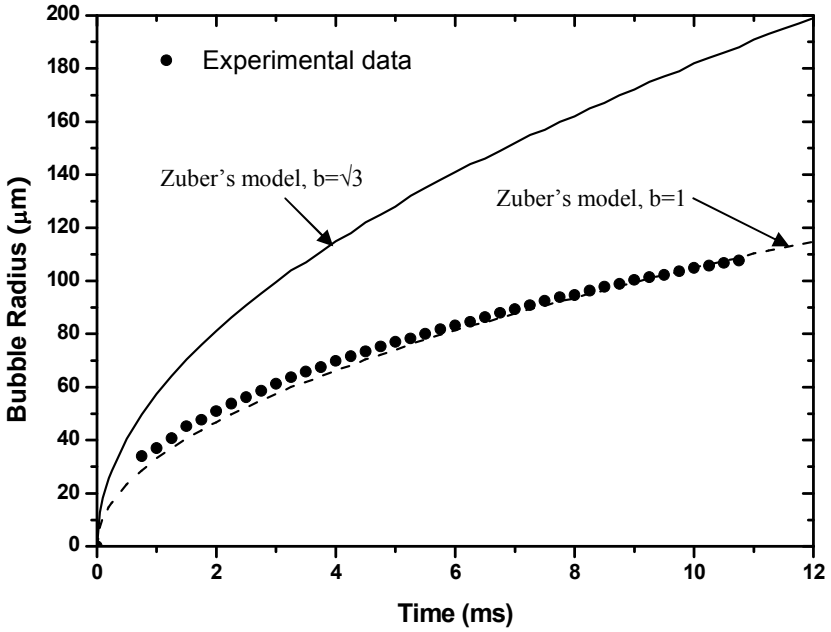

Figure 4.31. The growth rate of bubble-1on the copper heating surface (shown in Figure 4.29) and its comparison with Zuber's model.

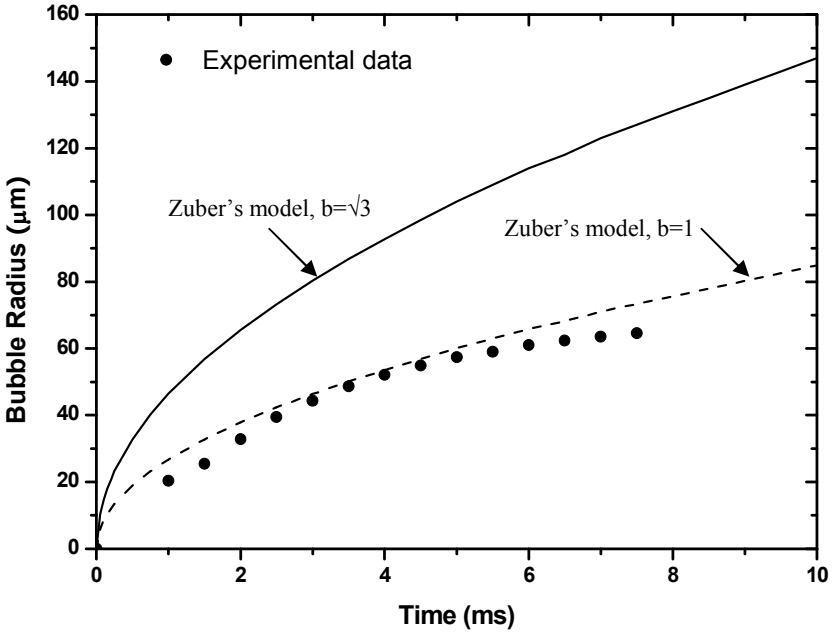

Figure 4.32. The growth rate of bubble-2 on the stainless steel surface (shown in Figure 4.30) and its comparison with Zuber's model.

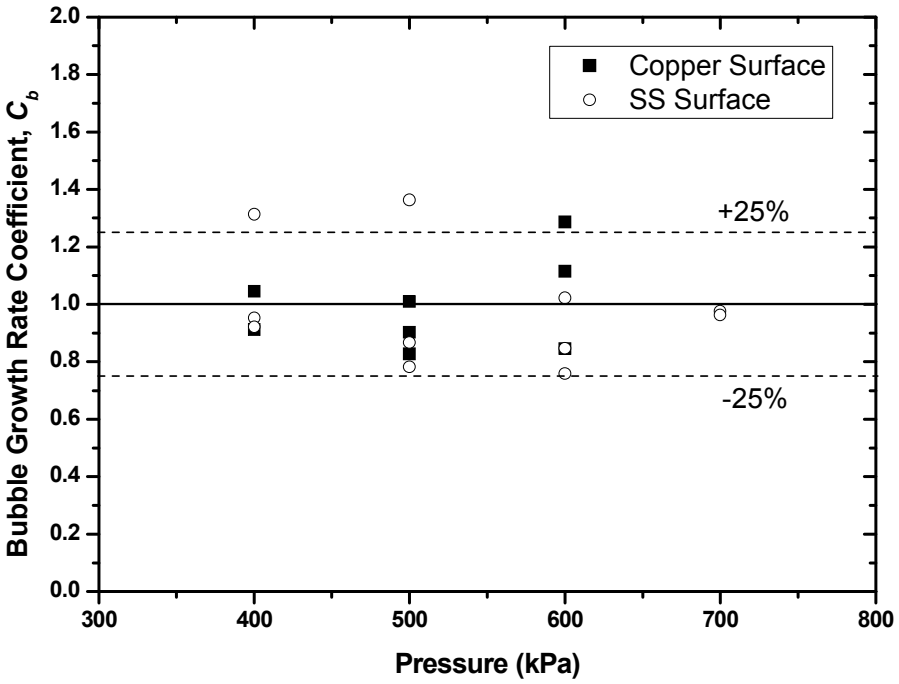

Figure 4.33. Bubble growth rate coefficient for both copper and stainless steel surfaces at different pressures.

As discussed above, bubble departure size largely determines how much energy a bubble is able to carry and also the bubble frequency. A model has been proposed by Zeng et. al. (Zeng et. al. 1993) to predict bubble departure size by a force balance in the flow direction. Major forces acting on a stationary bubble before its departure include fluid drag force, surface tension force and bubble growth force. As suggested by Klausner et al. (Klausner et al., 1993), the fluid drag force is proportional to bubble size and the relative velocity between a stationary bubble and its surrounding fluid. In some previous research, surface tension force was treated as negligible by noting that the bubble-solid contact diameter is much smaller than the bubble diameter. However, in the current study, the surface roughness was estimated to be in the magnitude of 10 microns. The bubble-solid contact diameter is assumed to have a similar value as the surface roughness. Bubble diameters observed had a same order of magnitude as the contact diameter. In this case, the surface tension force has to be considered

in the force balance. As suggested by Zeng et al., the bubble growth force is determined by bubble size, bubble growth rate and its time derivative. As discussed in the previous section, for a given working fluid the bubble growth rate is only a function of wall superheat. This suggests that the bubble departure size is mainly controlled by fluid properties, wall superheat level and the fluid velocity. However, the wall superheat level investigated in this study was only in a small range due to experimental limitations. As a result, the bulk velocity is expected to have a dominant effect on the bubble departure size under the experimental conditions investigated in this study. Figure 4.34 shows bubble departure sizes of both copper and stainless steel heating surfaces at different system pressures. It can be clearly seen that the bubble departure size decreases quickly with bulk liquid velocity. This is because the drag force is proportional to the liquid velocity. The effect of system pressure on bubble departure size is also shown in Figure 4.34. The bubble departure size is observed to be smaller at higher system pressures. From the comparison between these two heating surfaces in Figure 4.34, the heating surface materials have no apparent effect on bubble departure size. This again proves that the bubble dynamics is mainly controlled by liquid thermal properties and not heating surface material thermal properties.

In summary, bubble dynamics was experimentally investigated in this section. Bubble dynamics, covers a very wide range of topics, including bubble contact angle, bubble shape, bubble size and growth rate, waiting time, activation and deactivation, etc. Not all of them are quantifiable due to their complex physics and non-linear behaviors, and also experimental limitations on observations and measurements. In this study, some important parameters, which are directly related to boiling heat transfer, were experimentally measured. Contact angles were measured for both heating surfaces at different system pressures. System pressure was found to have no apparent effect on contact angle. The stainless surface has a slightly larger contact angle than the copper surface. The bubble growth rate was estimated by measuring bubble size at different times. Zuber's model fits the experimental data very well. Most of the bubble growth rate data were found to agree with Zuber's model within a ±25% error. Again, the heating surface material does not display a significant effect on the bubble

growth rate. The bubble waiting time was found to be negligible compared to bubble lifetime for both heating surfaces. With respect to bubble departure size, both average liquid bulk velocity and system pressure showed significant effects. Bubble departure sizes were found to be smaller at high bulk velocities and high system pressures. The comparison of bubble departure sizes between these two heating surfaces indicated heating surface material has only a minor effect. As a summary, copper and stainless steel heating surfaces were investigated in the current study with the same working fluid, R134a. Both surfaces had a same surface finishing and also showed similar wettability. By comparing bubble parameters, it was found that bubble dynamics is mostly controlled by liquid thermal and hydraulic conditions, while the heating surface thermal properties have little effect.

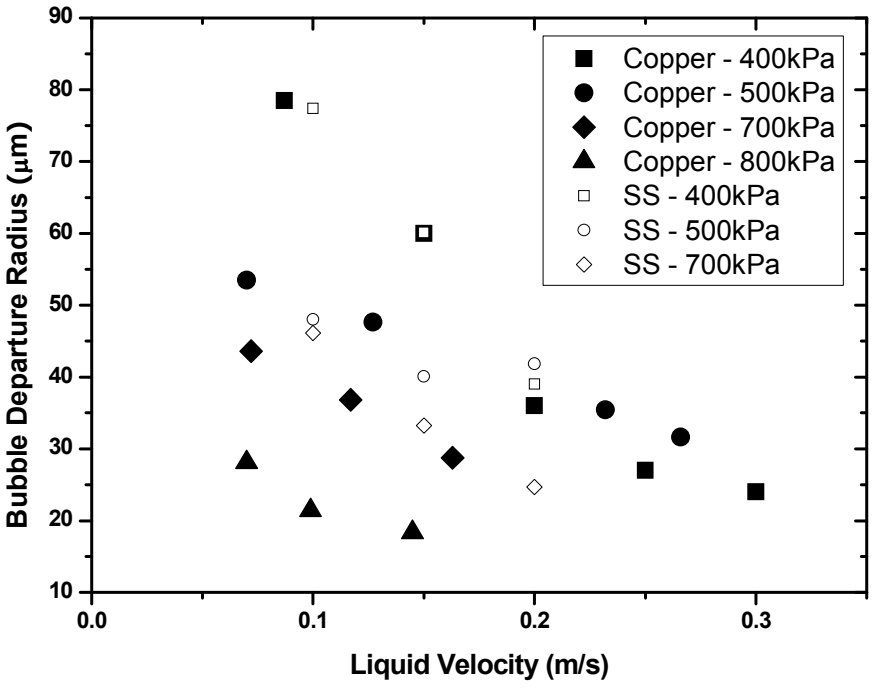

Figure 4.34. Bubble departure sizes on both copper and stainless steel surfaces at different pressures and bulk liquid velocities.

4.3 FLOW BOILING HEAT TRANSFER

The boiling heat transfer performances of the two heating surface materials, with R134a coolant, have been tested under various conditions, including system pressure, flow velocity, inlet subcooling level, etc. The system pressures were experimentally explored over a range from 400kPa to 800kPa. The average bulk velocity was varied over a range from 0.1 m/s to 0.2m/s, which corresponds to mass fluxes of around 120 kg/m^{2}s to 240 kg/m^{2}s, depending on system pressure. The average inlet subcooling level was controlled in the range of 10ºC to 30ºC. Figures 4.35 and 4.36 show typical boiling curves and plots of their corresponding heat transfer coefficients, respectively. The data shown in Figures 4.35 and 4.36 were obtained for 400kPa system pressure, liquid velocity at 0.1m/s and inlet subcooling of 10ºC, on the copper surface. In Figure 4.35, single phase convection is dominant in this low wall superheat region. Boiling then starts at a wall temperature, which is referred to as onset of nucleate boiling (ONB). As the wall temperature increases, more and more bubbles are generated on the heating surface and fully developed nucleate flow boiling develops. Between single phase convection and fully developed nucleate boiling, a transition region is normally present. As the wall temperature is increased even more, the bubble number reaches a limiting point above which it cannot increase more and departure from nucleate boiling (DNB) takes place, and the heating surface experiences a maximum heat flux. After reaching this maximum heat flux, the heat transfer coefficient drops dramatically and the wall temperature increases rapidly. The maximum heat flux achieved on a heating surface under such a condition is referred as the critical heat flux (CHF).

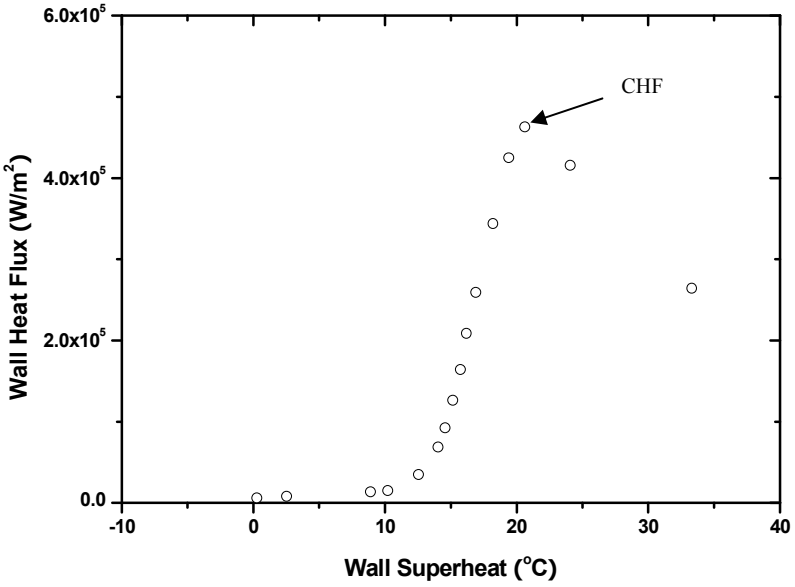

Figure 4.35. A typical boiling curve obtained from the copper surface at a pressure at 400 kPa, bulk liquid velocity at 0.1 m/s, inlet subcooling at 10 ºC.

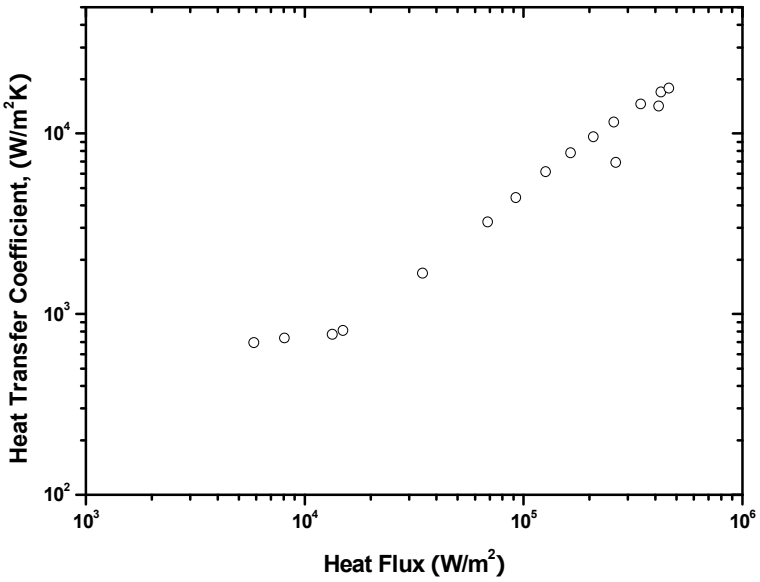

Figure 4.36. A typical heat transfer coefficient vs. wall heat flux curve obtained from the copper surface with system pressure at 400 kPa, bulk liquid velocity at 0.1 m/s, inlet subcooling at 10 ºC.

Figures 4.37 and 4.38 show the effect of heating surface material on flow boiling heat transfer performance. The effect of heating surface materials on boiling heat transfer has been studied in the past (Rohsenow, 1952; Gorenflo et al., 2004; Ribatski and Saiz Jabardo, 2003). Rohsenow (Rohsenow, 1952) expressed the material effect indirectly by introducing combined surface/liquid coefficients. Some other researchers included this effect explicitly using parameters directly involving material physical properties. In the current study, boiling curves for both copper and stainless steel heating surfaces are plotted in Figure 4.37. Heat fluxes were measured at an average liquid velocity of 0.10m/s, with system pressures ranging from 400 kPa to 700 kPa. For same system pressure, inlet subcooling levels were kept the same for these two surfaces, while they were higher for higher pressures. This plot clearly shows that the copper surface has better performance in terms of boiling heat transfer. More specifically, the copper surface achieves higher heat fluxes than the stainless steel surface at the same wall superheat temperature. In other words, at given wall heat flux, the copper surface has lower wall superheat temperatures than the stainless steel surface. The heat transfer coefficient plotted against wall heat flux in the fully developed flow boiling regime is shown in Figure 4.38. It shows that the copper surface has higher heat transfer coefficients at given wall superheat temperatures. Data obtained at a bulk liquid velocity of 0.2 m/s are plotted in Figures 4.39 and 4.40, similar to Figures 4.37 and 4.38. A linear correlation is observed between heat transfer coefficient and heat flux on these log-log plots, indicating that the heat transfer coefficient can be expressed in the form of,

$$h = Cq^m \tag{4-20}$$

in which, the exponent m is the slope of the heat transfer coefficient vs. heat flux (h *vs.* q) curve. Corresponding to boiling curves shown in Figures 4.37 and 4.39, (h *vs.* q) curves on the copper surface have larger slopes than those on the stainless steel surface. Values of m are estimated by curve fittings to experimental data. For example, values of m shown in Figure 4.38 on the copper surface are 0.9338, 0.9731, 0.9899, and 0.9933 for system pressures of 400,

500, 600, and 700 kPa, respectively. The corresponding *m* values for the stainless steel surface are 0.8194, 0.8832, 0.8836 and 0.9145, respectively.

Critical heat fluxes experienced by these two surfaces were also experimentally measured, as plotted in Figure 4.41. At a low bulk liquid velocity, 0.1m/s, critical heat fluxes on the copper surface are slightly higher than those on the stainless steel surface. The differences between them are not significant. At a relatively higher bulk liquid velocity, 0.2m/s, it's clear that the copper surface has higher critical heat fluxes. Compared to the stainless steel surface, the copper surface has about 5% higher critical heat flux values. However, it should be noted that Figure 4.41 does not necessarily reflect the pressure effect on critical heat flux since different inlet subcooling levels were used.

The pressure effect on the heat transfer coefficient is plotted in Figures 4.42 and 4.43. Heat fluxes were measured for both heating surfaces, at the same bulk liquid velocity of 0.15m/s and inlet subcooling level of 22.0 ºC, for pressures of 500, 600 and 700kPa. Figure 4.43 shows that pressure does not have a significant impact on boiling heat transfer on both heating surfaces. Values of *m* were determined by curve fitting and are plotted with system pressure and the reduced pressure in Figure 4.43. The reduced pressure is defined as,

$$p_r = \frac{p}{p_{cr}} \tag{4-21}$$

in which, p_r, p and p_{cr} are reduced pressure, system pressure and fluid critical pressure, respectively. Figure 4.43 indicates that in pressure ranges experimentally explored in the current study, pressure does not have a significant impact on boiling heat transfer coefficient. A possible reason is that the pressure explored in the current study is limited in a small range, or more specifically, the reduced pressures ranging from 0.12 to 0.17. The effect of reduced pressure has been studied by different researchers. Cooper (Cooper 1984) proposed a correlation to account for both reduced pressure and surface roughness on heat transfer coefficient. Gorenflo (Gorenflo 2004) proposed a correlation to directly incorporate the effect of the reduced pressure for pool boiling. This correlation is expressed as,

$$m = 0.9 - 0.3 p_r^{0.3} \quad (4\text{-}22)$$

in which, the slope value *m* decreases with reduced pressure. The comparison between experimental data and Gorenflo's correlation is displayed in Figure 4.43. It shows that this correlation for pool boiling but does not give good predictions for flow boiling.

Corresponding critical heat flux data are plotted against pressure in Figure 4.44. Unlike its minor impact on the heat transfer coefficient, pressure shows a significant influence on critical heat flux. For example, on both copper and stainless steel surfaces, critical heat fluxes measured at 700 kPa are around 7-8% higher than those measured at 500 kPa.

Figures 4.45 to 4.48 show the effect of fluid velocity on boiling heat transfer performance on both surfaces. Data shown in Figures 4.45 and 4.46 were obtained from flow boiling on both surfaces at 500 kPa system pressure, inlet subcooling at 18 ºC, with bulk liquid velocities of 0.1, 0.15 and 0.2 m/s. Data shown in Figures 4.47 and 4.48 were obtained from flow boiling on both surfaces at 700 kPa system pressure, inlet subcooling at 27 ºC, with bulk liquid velocities of 0.1, 0.15 and 0.2 m/s. Both figures show that liquid velocity does not have a significant impact on flow boiling heat transfer in the fully developed regime. A similar phenomenon has also been experimentally observed by another researcher (McAdams 1949). It's been found that, with other conditions fixed, boiling curves with different liquid velocities collapse onto the same curve in the fully developed flow boiling regime. Normally, a higher liquid velocity gives a higher heat transfer coefficient in the single-phase convection region. Also, transition from partially to fully developed flow boiling occurs at a higher wall temperature. In addition, critical heat fluxes are higher for higher liquid velocities, which were also experimentally observed for different pressures and inlet subcooling levels in this study, shown in Figure 4.49. The inlet subcooling level effect is shown in Figures 4.50, 4.51 and 4.52. Similarly for the bulk liquid velocity, the inlet subcooling level does not show significant impact on flow boiling heat transfer. However, it's normally accepted that heat fluxes are higher in the fully developed flow boiling regime as the inlet subcooling level is higher. This phenomenon was not clearly observed in the current study, which may be due to

the limited inlet subcooling range explored. The critical heat flux, however, shows an apparent dependence on the inlet subcooling level. Figure 4.52 shows critical heat fluxes measured for both surfaces at different pressures and inlet subcooling levels. It clearly shows that, for given pressures, higher inlet subcooling levels give higher critical heat fluxes.

Flow boiling heat transfer performance on both copper and stainless steel surfaces, including parametric studies, were experimentally carried out in this study. Experimental data clearly show that the copper surface has better performance than the stainless steel surface in terms of both heat transfer coefficient and critical heat flux. Parametric studies, such as effects of pressure, bulk liquid velocity, and inlet subcooling level, were also presented. The comparison between the current study and other research shows good agreement. From experimental results obtained in the current study, it was concluded that heat flux is largely determined by nucleation site density. Also, the bubble dynamics on both surfaces show almost identical characteristics. The differences on boiling heat transfer between these two surfaces, however, raises a question as to what is the root cause for the differences. A possible explanation is that lateral heat transfer just inside the heating surface creates a non-uniform surface temperature distribution. The lateral heat transfer is governed by heating surface thermal properties, such as thermal conductivity and thermal diffusivity, which are greatly different for the two heating surfaces investigated. This suggested further model development to investigate the heat transfer inside the heating surface, from which a surface temperature profile can be obtained. This may shed some light on boiling heat transfer performance differences between these two heating surface materials.

4.4 SUMMARY AND DISCUSSION

In this study, the subcooled flow boiling on copper and stainless steel heating surfaces was experimentally investigated from both macroscopic and microscopic points of view. Nucleation site density, an essential parameter in determining the flow boiling heat transfer capacity, was measured for both surfaces using a high-speed digital video camera.

Number of nucleation sites and their locations in domains of interest were able to be measured. Several conclusions were made based on these observations and data analysis:

(1) Wall superheat, critical cavity diameter and wall heat flux were used to correlate with the nucleation site density data. Among them, the wall heat flux showed the best correlating behavior to eliminate both pressure and surface properties effects.

(2) The observed nucleation site distribution agreed well with the spatial Poisson distribution when only considering probability density of nucleation numbers counted in sub-domains.

(3) The distribution of nearest-neighbor sites distance, however, did not agree with the spatial Poisson distribution. The observed data had a more uniform distribution compared to the spatial Poisson distribution, which might be a result of interactions of nucleation sites.

(4) The distribution of nucleation sites on the copper surface was slightly more uniform than that on the stainless steel surface, which is probably a result from stronger interactions of nucleation sites due to higher thermal diffusivity.

Bubble dynamics were experimentally observed and recorded via the high-speed digital camera. In this study, some of the important parameters, which are directly related to the boiling heat transfer capacity, were experimentally measured. Some conclusions were made based on the observations and data analysis,

(5) System pressure showed no significant influence on contact angle. The stainless steel surface had slightly larger contact angles than those on the copper surface.

(6) Bubble growth rates measured for both heating surfaces were fairly similar, which agreed very well with Zuber's model. There is no apparent difference between these two surfaces in terms of bubble growth rate.

(7) Bubble waiting time was measured to be negligible compared to bubble lifespan for both surfaces.

(8) Bubble departure size tended to be smaller with either a higher liquid velocity or a higher system pressure. Similarly, heating surface material showed a minor effect.

According to the findings listed above, it is pretty clear that for these two materials investigated, which have similar surface wettability while distinctively different thermal properties, bubble dynamics displays fairly similar behavior.

The last part of the experimental investigation was to measure the flow boiling performance of both surfaces. It was found that,

(9) Experimental data clearly showed a trend that the copper surface had a better performance than the stainless steel surface in terms of both heat transfer coefficient and critical heat flux.

(10) Parametric studies, such as effects of pressure, bulk liquid velocity, and inlet subcooling level, showed good agreement with results from other researches.

A further model development to investigate the lateral heat transfer inside the solid heating surface was suggested to explore possible reasons for performance differences. This model development will be presented in the next chapter.

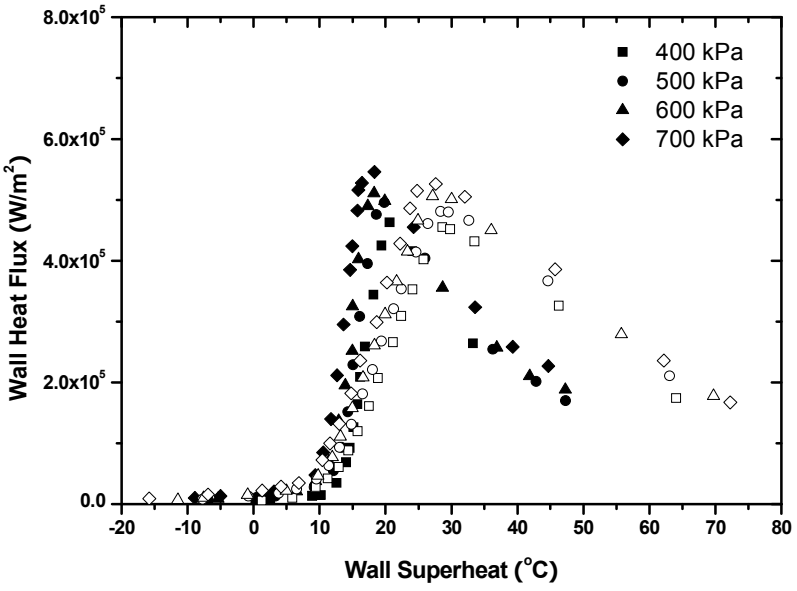

Figure 4.37. Surface material's effect on the flow boiling. Boiling curves at different pressures. Bulk liquid velocity, 0.1 m/s. Blackened symbols, copper surface; open symbols, stainless steel surface.

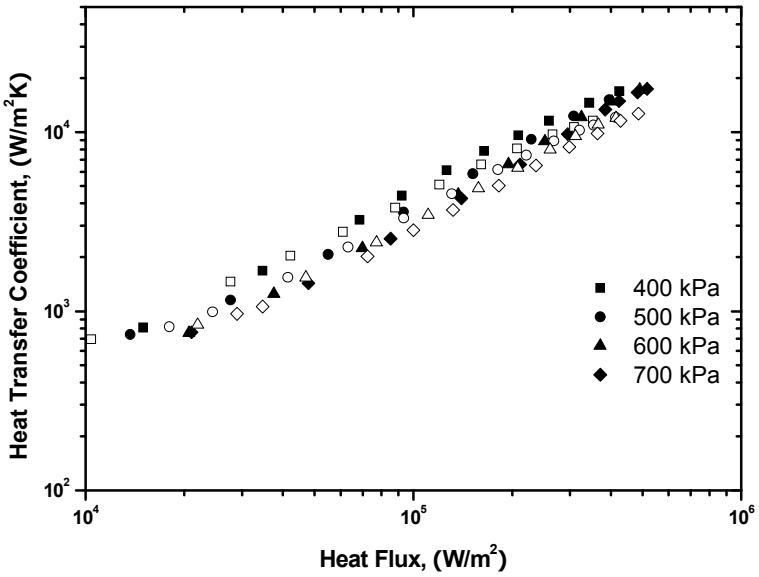

Figure 4.38. Surface material's effect on the flow boiling. Heat transfer coefficient vs. wall heat flux in the fully developed flow boiling region (corresponding to Figure 4.37). Blackened symbols, copper surface; open symbols, stainless steel surface.

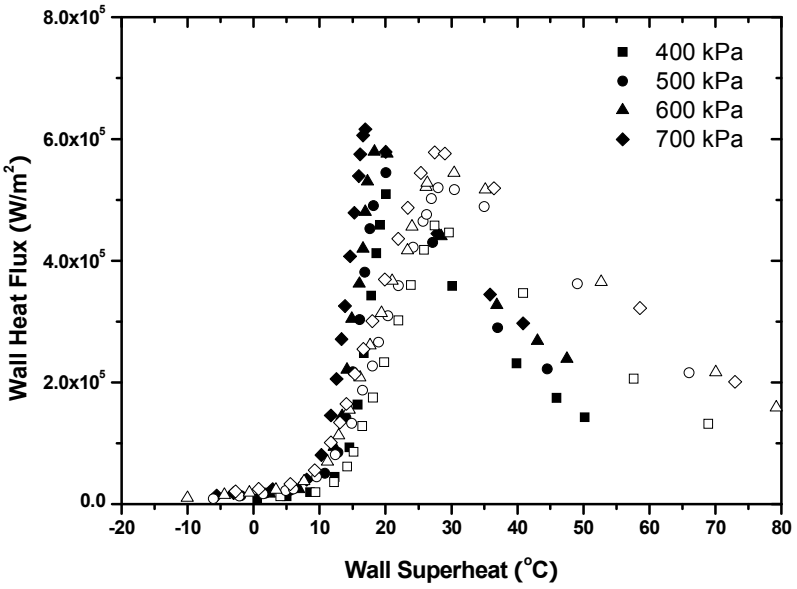

Figure 4.39. Surface material's effect on the flow boiling. Boiling curves at different pressures. Bulk liquid velocity, 0.2 m/s. Blackened symbols, copper surface; open symbols, stainless steel surface.

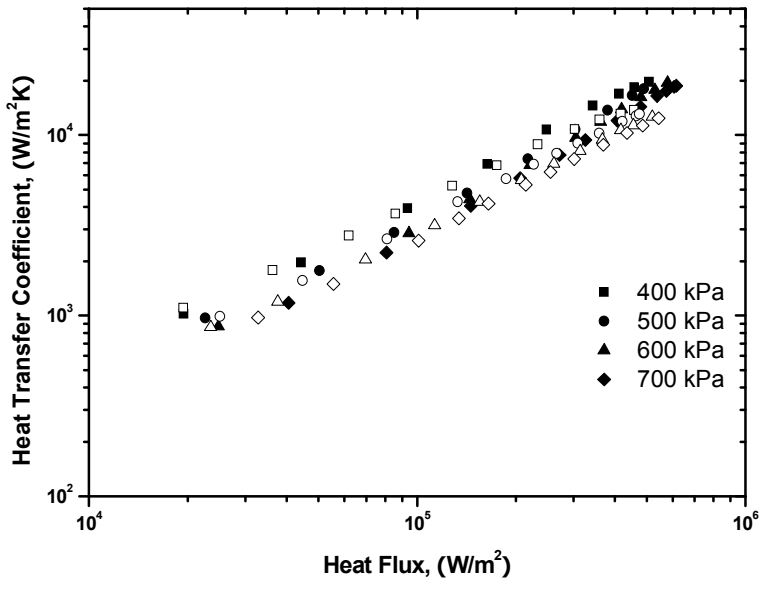

Figure 4.40. Surface material's effect on the flow boiling. Heat transfer coefficient vs. wall heat flux in the fully developed flow boiling region (corresponding to Figure 4.39). Blackened symbols, copper surface; open symbols, stainless steel surface.

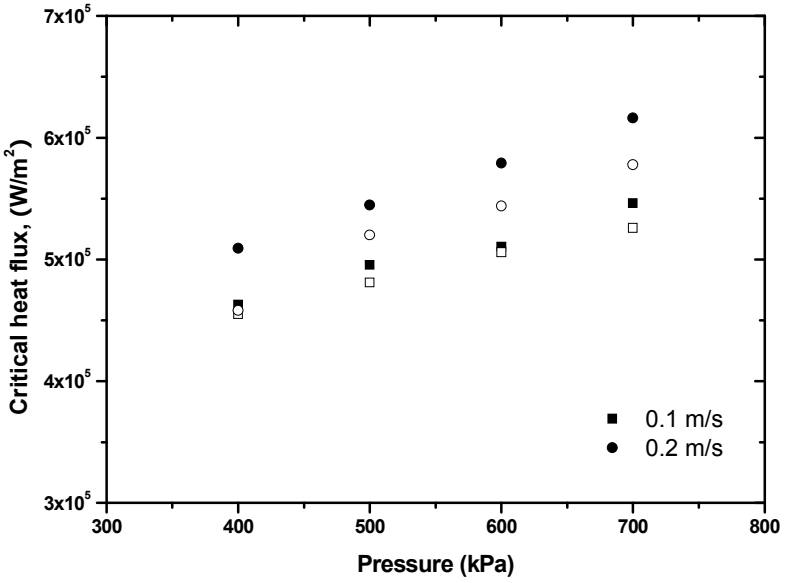

Figure 4.41. Surface material's effect on the critical heat flux. Critical heat flux at different pressures and velocities. Blackened symbols, copper surface; open symbols, stainless steel surface.

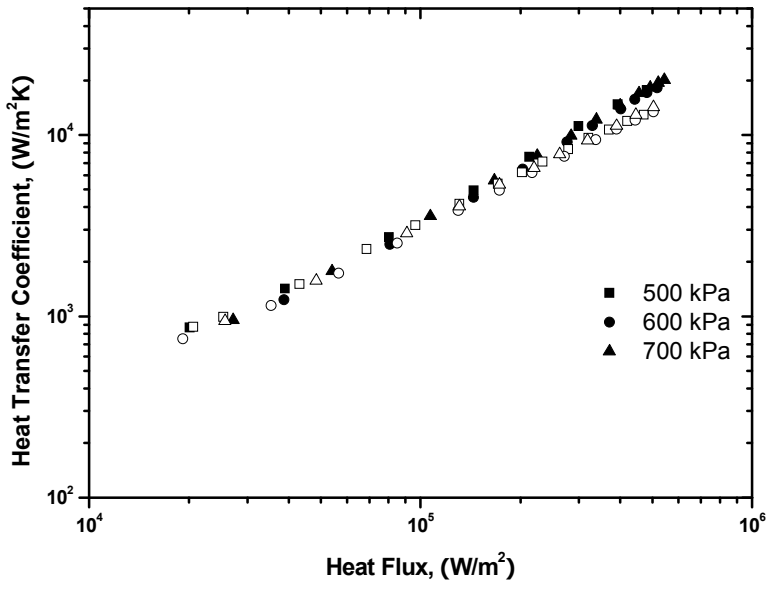

Figure 4.42. Surface material's effect on the flow boiling. Heat transfer coefficient vs. wall heat flux. Bulk liquid velocity at 0.15m/s. Inlet subcooling at 22 ºC. Blackened symbols, copper surface; open symbols, stainless steel surface.

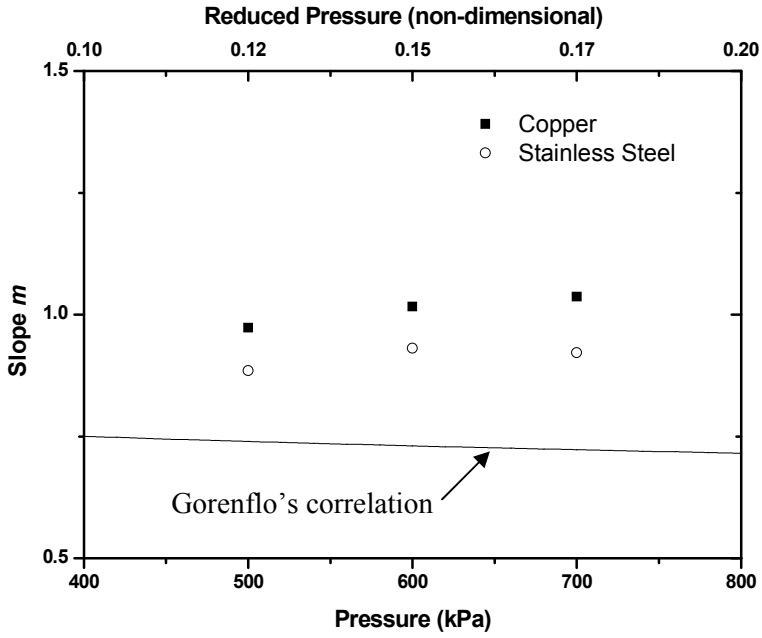

Figure 4.43. Surface material's effect on the flow boiling. Slope, *m*, of heat transfer coefficient vs. wall heat flux curves for both the copper and the stainless steel surfaces shown in Figure 4.42.

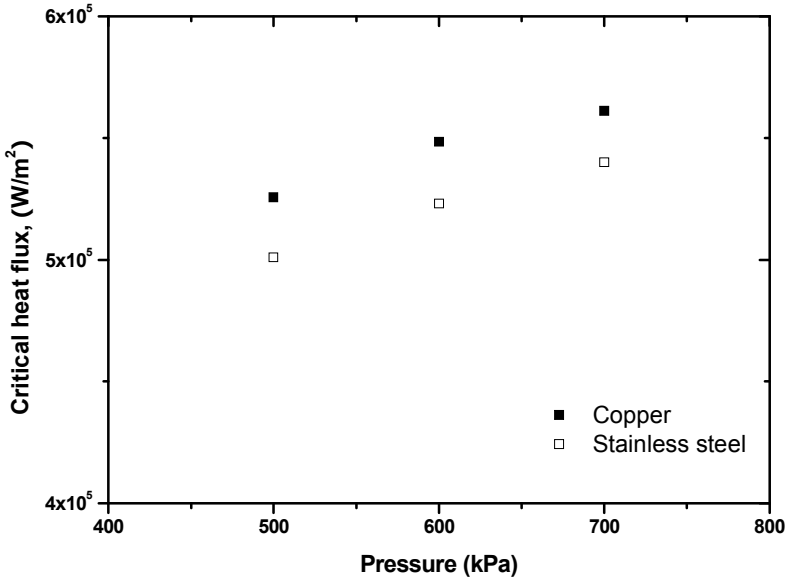

Figure 4.44. Effect of pressure on the critical heat flux. Bulk liquid velocity at 0.15m/s. Inlet subcooling at 22 ºC. Blackened symbols, copper surface; open symbols, stainless steel surface.

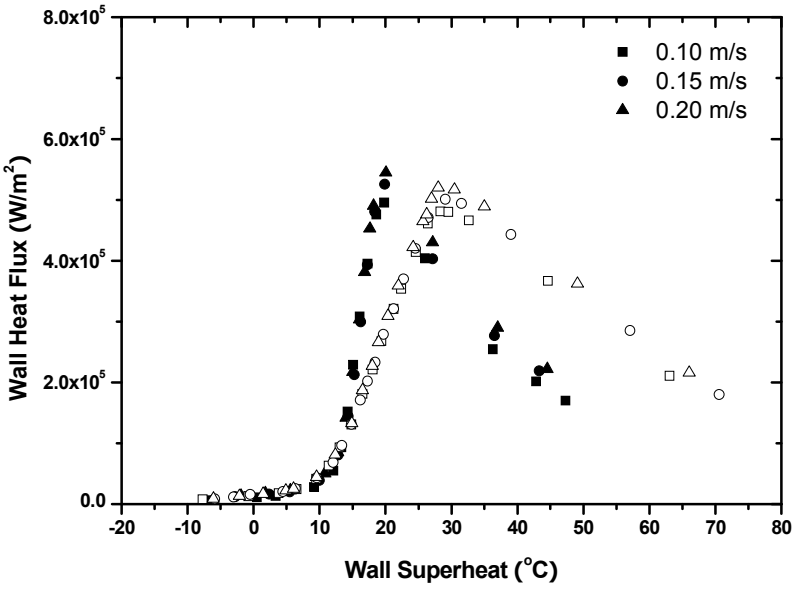

Figure 4.45. Effect of bulk liquid velocity on the flow boiling. Boiling curves at different bulk liquid velocities. Pressure at 500 kPa, inlet subcooling at 18 ºC. Blackened symbols, copper surface; open symbols, stainless steel surface.

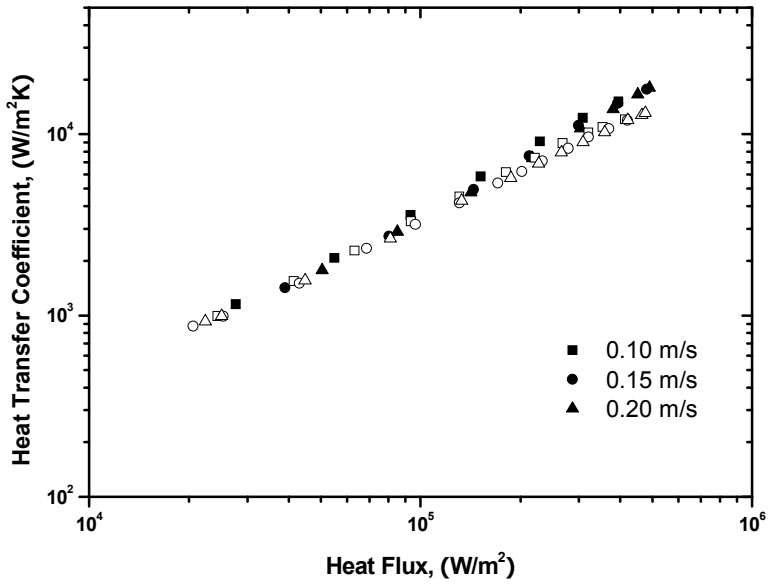

Figure 4.46. Effect of bulk liquid velocity on the flow boiling. Heat transfer coefficient vs. wall heat flux in the fully developed flow boiling region (corresponding to Figure 4.45). Blackened symbols, copper surface; open symbols, stainless steel surface.

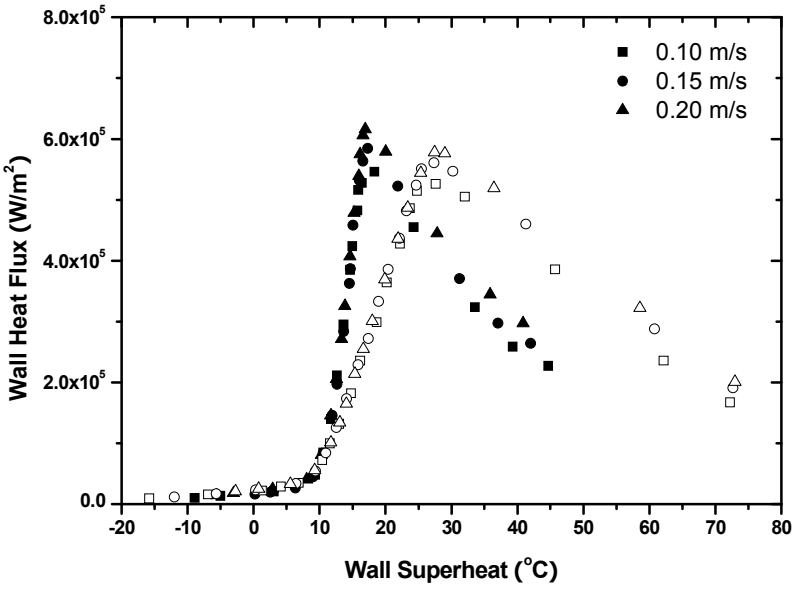

Figure 4.47. Effect of bulk liquid velocity on the flow boiling. Boiling curves at different bulk liquid velocities. Pressure at 700 kPa, inlet subcooling at 27 ºC. Blackened symbols, copper surface; open symbols, stainless steel surface.

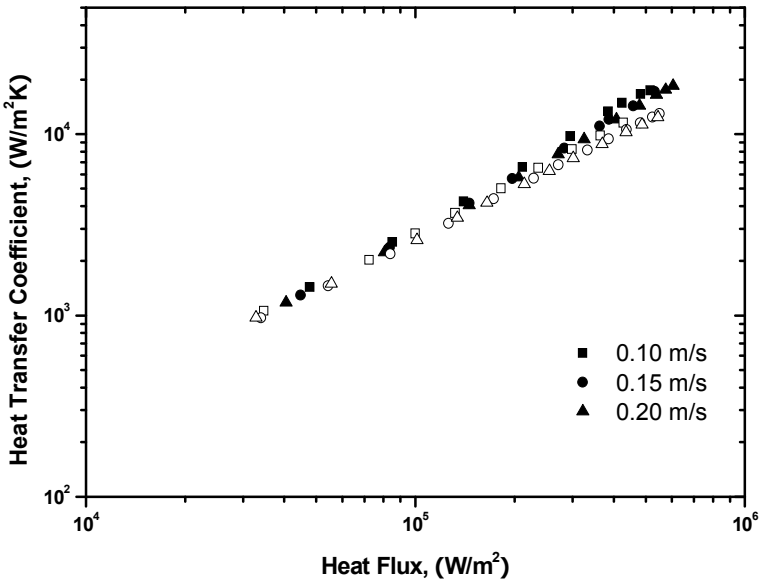

Figure 4.48. Effect of bulk liquid velocity on the flow boiling. Heat transfer coefficient vs. wall heat flux in the fully developed flow boiling region (corresponding to Figure 4.47). Blackened symbols, copper surface; open symbols, stainless steel surface.

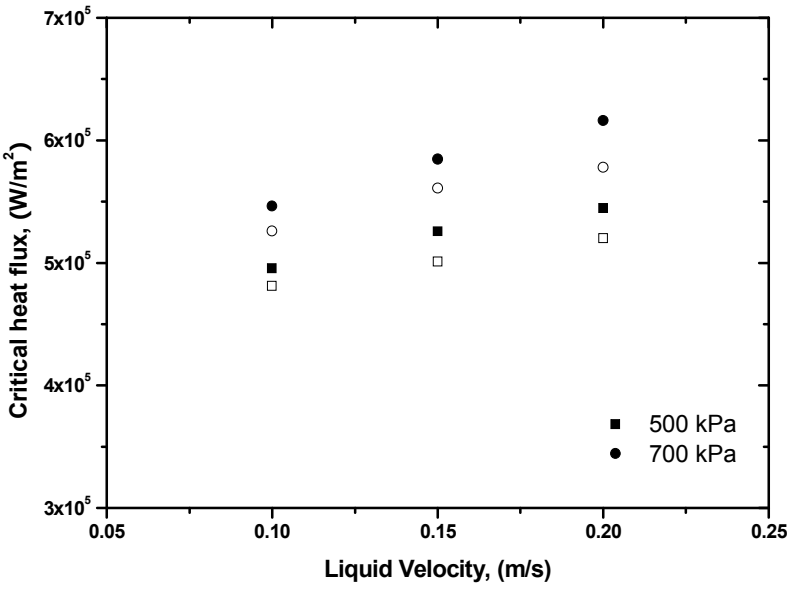

Figure 4.49. Effect of bulk liquid velocity on the critical heat flux. For pressure at 500 kPa, inlet subcooling is 18 ºC; for pressure at 700 kPa, inlet subcooling is 27 ºC. Blackened symbols, copper surface; open symbols, stainless steel surface.

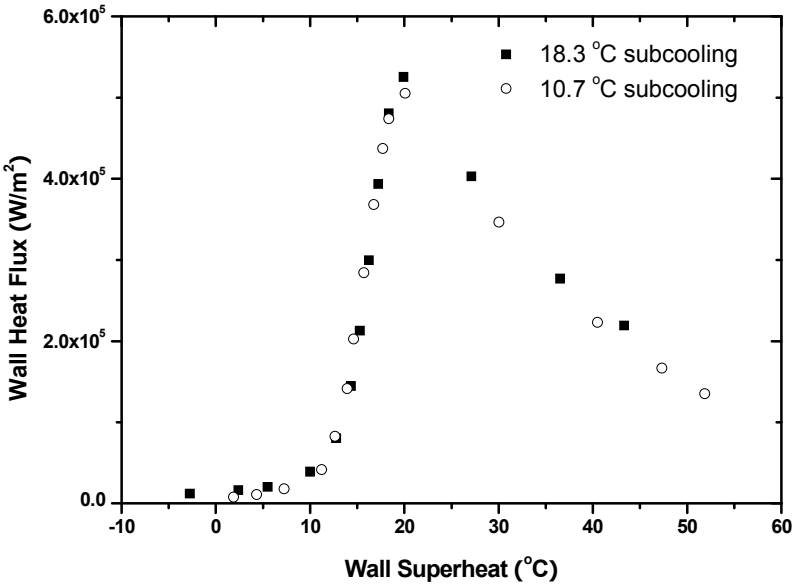

Figure 4.50. Effect of inlet subcooling on the flow boiling. Boiling curves at different inlet subcooling on the copper surface. Pressure at 500 kPa, bulk liquid velocity at 0.15 m/s.

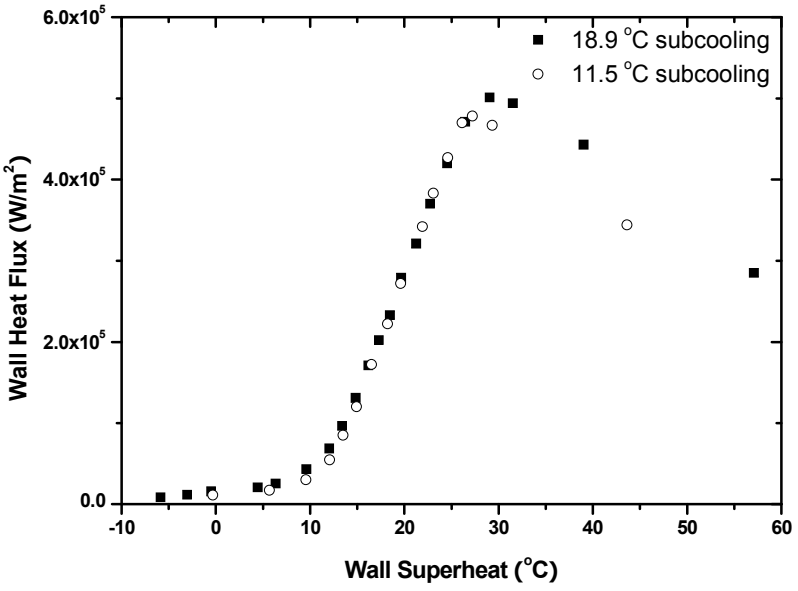

Figure 4.51. Effect of inlet subcooling on the flow boiling. Boiling curves at different inlet subcooling on the stainless steel surface. Pressure at 500 kPa, bulk liquid velocity at 0.15 m/s.

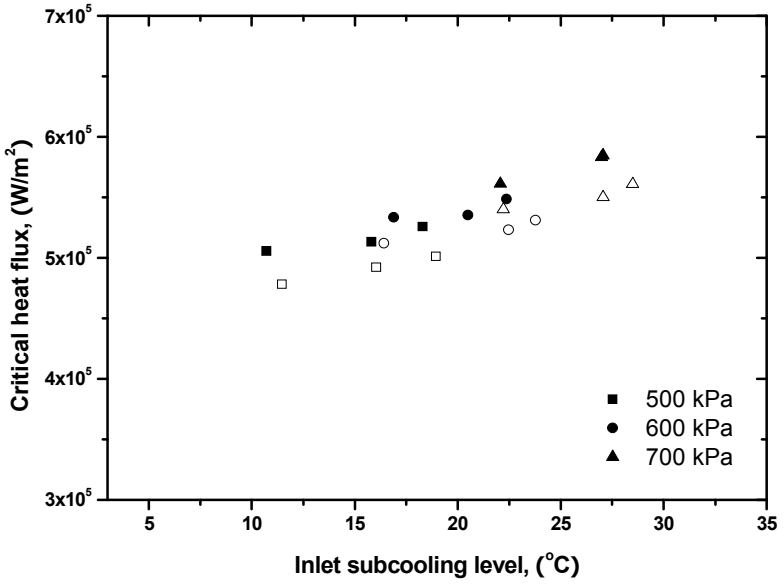

Figure 4.52. Effect of inlet subcooling on the critical heat flux. Pressure at 500 kPa, bulk liquid velocity at 0.15 m/s. Blackened symbols, copper surface; open symbols, stainless steel surface.

CHAPTER 5

MODEL DEVELOPMENT

Subcooled flow boiling heat transfer has been experimentally studied in this thesis work and has been presented in the previous chapter. The wall heat flux has been found to directly correlate with the nucleation site density. Also, experimental evidence shows that the working fluid, R134a, has similar contact angles on both copper and stainless steel surfaces. The measured bubble parameters, such as bubble size and growth rate, are similar on both surfaces too. However, it's been found that the copper heating surface has a better performance than the stainless steel surface in terms of heat transfer coefficient. As discussed in previous chapters, significant differences between these two surface materials are their thermal properties, such as thermal conductivity and thermal diffusivity. This indicates that thermal properties of heating surface materials play important roles in their performance. This is based on the fact that thermal conductivity has a significant impact through lateral heat transfer and consequently temperature uniformity of the heating surface. To quantify the impact of thermal conductivity on boiling heat transfer, a model development is suggested. In this chapter, a simplified model is developed to simulate heat transfer within the heating block at the surface solid domain when bubbles are present on the heating surface. The purpose is to study the impact of several key parameters' on lateral heat transfer and surface temperature profile. These parameters include: material thermal conductivity, bubble size, heating surface thickness, etc.

5.1 MODEL DESCRIPTION

It is known that flow boiling is a complex phenomenon in which several heat transfer mechanisms are present simultaneously. In general, in flow boiling the overall heat transfer consists of three major components: latent heat carried by vapor bubbles, transient conduction due to the quenching effect on heating surface after bubble departure, and single phase

convection from areas without bubble coverage. The first two heat transfer mechanisms are closely related to bubble formation, growth and departure. Models have been developed to account for these two heat transfer mechanisms while single phase convection is relatively easier to estimate. It would be ideal to simulate the transient heat transfer process induced by a bubble during its lifespan so that a time dependant temperature profile on the heating surface can be obtained. An effort to develop such a model would include details such as bubble dynamics, quenching effects induced by bubble movement, thermal and hydraulic interactions between bubbles, etc. Also, such a model would include too many uncertainties as we know that the boiling phenomenon by itself is a random process. For example, the bubble departure size has been measured to be a random number which fits a Gaussian distribution. Again, the purpose of this modeling is to focus on the impact of thermal properties and other key parameters, therefore, a simplified model is proposed rather than the full model described above.

Active nucleation sites have been experimentally observed to fit a random distribution which is similar to, while not exactly the same as, a spatial Poisson distribution. To simplify the model, the sites are assumed to be uniformly distributed and located on a hexagonal lattice, Figure 5.1. Bubbles sit on active nucleation sites and serve as heat sinks. The entire heating surface then can be modeled as a sum of cylindrical 'unit cells'. A cylindrical unit cell has a thickness of δ, which is identical to the heating surface thickness. The radius of a unit cell, R_c, is calculated from the nucleation site density, N_a, using

$$N_a \pi R_C^{\,2} = 1 \tag{5-1}$$

Due to the axially symmetric characteristics of the cylindrical unit cell, the heat transfer within such a unit cell can be described by the two-dimensional Laplace equation in cylindrical coordinates,

$$\frac{1}{r}\frac{\partial}{\partial r}\left(r\frac{\partial}{\partial r}T\right)+\frac{\partial^2}{\partial z^2}T=0 \tag{5-2}$$

in which, T is the temperature.

The boundary conditions are described as follows.. On the bottom side of the heating surface, $z = 0$, it's assumed that there's a uniformly distributed heat flux q'',

$$-k\left.\frac{\partial T}{\partial z}\right|_{(z=0)} = q'' \tag{5-3}$$

in which, k is the thermal conductivity of the heating surface material. Due to repeatability of unit cells, on the unit cell boundary, where $r = R_c$, ,a symmetric boundary condition is assumed,

$$\left.\frac{\partial T}{\partial r}\right|_{(r=R_c)} = 0 \tag{5-4}$$

On the heating surface, $z = \delta$, the boundary condition has to be set properly to represent boiling heat transfer. As discussed above, boiling heat transfer is a very complex phenomenon which consists of several heat transfer mechanisms. Bubbles are the major media to transfer the energy in the form of latent heat and also they agitate local micro-convection. The heat transfer on surfaces not covered by bubbles is dominated by single phase forced convection, which normally contributes only a small fraction to the total heat transfer (Wu 2007, Basu et al. 2005b). To simplify the model, it's assumed that all energy is transferred via bubbles while the surface not covered by bubbles is under adiabatic conditions. The boundary condition on the heating surface, $z = \delta$, then can be expressed as,

$$-k\left.\frac{\partial T}{\partial z}\right|_{(z=\delta)} = h_b\left(T - T_{bulk}\right) \quad \text{at } \left(0 \le r \le R_b\right) \tag{5-5}$$

and,

$$-k\left.\frac{\partial T}{\partial z}\right|_{(z=\delta)} = 0 \quad \text{at } \left(R_b < r \le R_c\right) \tag{5-6}$$

in which, T_{bulk} is the bulk temperature and h_b is the boiling heat transfer coefficient. Since a bubble is always approximately at its saturation temperature, heating surfaces covered by bubbles are assumed to be at the same temperature due to the very high heat transfer coefficient. Therefore, the boiling heat transfer coefficient can be back calculated as,

$$h_b = \frac{q'' \pi R_c^{\,2}}{\pi R_b^{\,2}\left(T_s - T_{bulk}\right)} \tag{5-7}$$

in which, T_s is the saturation temperature.

In the experimental part of current study, the stainless steel surface is attached onto the copper base block by silver soldering. The thickness of the stainless steel layer is 1 mm, which is much larger than the normal bubble size. As discussed in chapter 3, this will assure that the copper base won't have any impact on the boiling performance of the stainless steel. To explore the effect of the stainless steel layer thickness attached onto the copper base, a secondary model was built, schematically shown in figure 5.2. The only difference between these two models is that the secondary model has a two-layer configuration, in which the stainless steel layer lies on the top of the copper block. This secondary model is only used when studying the heating surface thickness effect with the two-layer configuration. The governing equation is still the same as equation (5-2) in both two layers and an additional boundary condition for the stainless steel-copper interface is used,

$$-k_{Cu}\left.\frac{\partial T_{Cu}}{\partial z}\right|_{(z=\delta_c)} = -k_{SS}\left.\frac{\partial T_{SS}}{\partial z}\right|_{(z=\delta_c)} \tag{5-8}$$

in which, T_{Cu} and T_{SS} are temperatures in the copper and stainless steel layers, respectively, and. k_{Cu} and k_{SS} are thermal conductivities of copper and stainless steel, respectively.

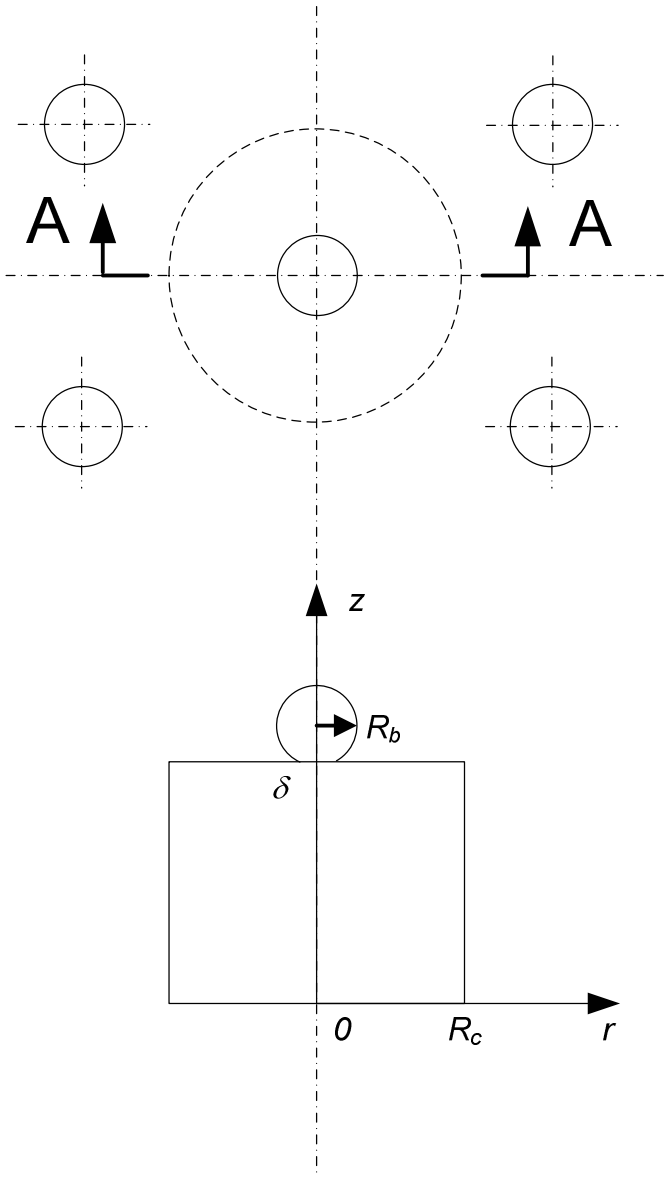

Figure 5.1. Schematic of a unit cell with a single layer of heater material and a bubble in the center.

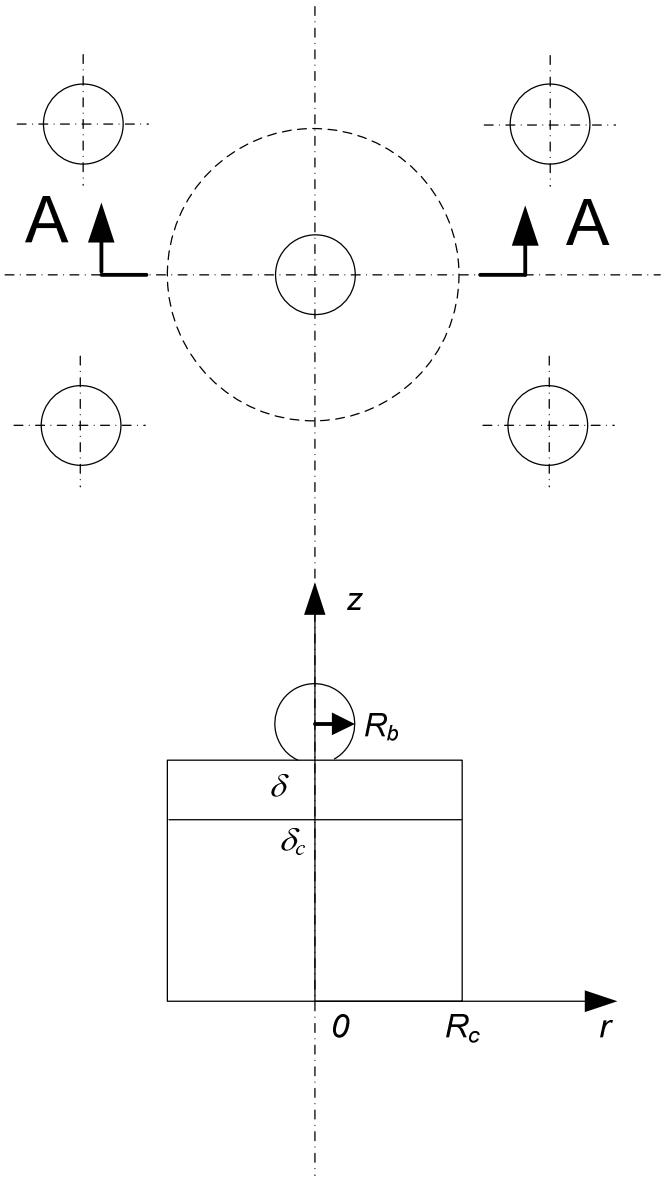

Figure 5.2. Schematic of a unit cell with a two-layer heater configuration and a bubble in the center.

5.2 MODEL RESULTS

In this section, results of the model prediction are presented. As discussed in the previous section, the purpose of this model development was to explore the impact of several key parameters on the lateral heat transfer in the heater block very near to the heating surface and consequently the surface temperature profile. These parameters include the heater surface material thermal conductivity, thickness of heating surface, relative bubble size to unit cell size and also heat flux. The model is numerically solved by a commercial CFD software package, FLUENT ®.

To quantify these parametric effects, a sample case is numerically solved. The system pressure is 300 kPa with the saturation temperature is 270K. The bulk inlet subcooling level is 20 K. The radius of the unit cell is set at 0.1 mm, which is equivalent to a nucleation site density of 3.18×10^7 sites/m^2. The bubble radii explored include 0.02 mm, 0.04 mm, 0.06 mm and 0.08 mm. Heat transfer coefficients are solved using equation (5-7). The thicknesses of heating surface explored include 0.01 mm, 0.02 mm, 0.05 mm, 0.1 mm, 0.15 mm and 0.2 mm. Heating surface materials explored include materials with different thermal conductivities, such as stainless steel, tin, nickel, brass, 7075 aluminum, pure aluminum, and pure copper. Different heat fluxes were also studied, including 1×10^5 up to 5×10^5 W/m^2.

The first parameter explored is the thermal conductivity of the heating surface material. In chapter 4, the experimental results show that the copper and stainless steel heating surfaces have different flow boiling heat transfer capacities, while both nucleation site density and bubble dynamics do not show significant differences. As discussed in the previous chapter, a possible reason for this is that the thermal conductivity of the heating surface material affects the lateral heat transfer inside the heating block and therefore the surface temperature varies with materials. On a heating surface, a bubble serves as a heat sink with a high heat transfer coefficient due to coolant phase change. The temperature under a bubble therefore is expected to be low and close to the saturation temperature. The heating surface without bubbles covering is then controlled by two heat transfer mechanisms, forced convection to the bulk flow and lateral heat conduction to the bubble covered region.

Compared to the phase change during bubble growth, the forced convection is a relatively inefficient to transfer mechanism. If the thermal conductivity is high enough, lateral heat conduction can be even more important than forced convection to transfer energy from the heating surface into the bulk flow. Figure 5.3 shows temperature profiles on heating surfaces made of materials with different thermal conductivities. The temperature profiles were solved in a unit cell with radius of 0.1 mm and thickness of 0.1 mm. The bubble radius was set at 0.02 mm and the heat flux was set at 1×10^5 W/m^2. Figure 5.4 shows the maximum and average surface temperatures corresponding to Figure 5.3. From Figure 5.3, it can be seen that due to the presence of a bubble, all temperature profiles have a dip in the center region. The surface with a higher thermal conductivity has a flatter surface temperature profile, which has both smaller maximum and average surface temperatures. This proves that an active bubble has a larger influence area when the heating surface thermal conductivity is higher. This explains that in flow boiling, on a copper surface tends to have a more uniform nucleation site distribution than on a stainless steel surface, which has been experimentally observed in this study. It is also found that at a relatively low heat flux, 1×10^5 W/m^2, the average surface temperature difference between a copper surface and a stainless steel surface is more than 2 K. This numerical result agrees very well with the experimental results presented in chapter 4. Also, as thermal conductivity increases, the effect of the thermal conductivity becomes negligible.

Figure 5.5 displays surface temperature profiles on a copper heating surface of different thicknesses, ranging from 0.01 mm to 0.2 mm (10 μm to 200 μm). Correspondingly, Figure 5.6 displays the maximum and average surface temperatures for different thicknesses. A similar set of numerical data are presented in Figures 5.7 and 5.8 for a stainless steel heating surface. Both numerical solutions were obtained with the same bubble radius of 0.02 mm and heat flux of 1×10^5 W/m^2. Similar temperature profiles are found for both the copper and the stainless steel surfaces but with different temperature magnitudes. For both material two surfaces, the overall surface temperature becomes higher as the heating surface becomes thinner. For heating surface thicknesses is larger than 0.05 mm, which is 2.5 times of the

bubble radius, the heating surface thickness does not show any significant impact on the temperature profiles. This is also shown in Figures 5.6 and 5.8 for the copper and the stainless surfaces, respectively. Comparing Figures 5.5 and 5.7, shows that thickness has a smaller effect on the surface temperature profile on the copper heating surface due to the much higher thermal conductivity and therefore better lateral heat transfer. The heating surface thickness effect has also been studied in another way with the secondary model described in the previous section. In this secondary model, the stainless steel layer is installed on a copper base block by silver soldering, which is assumed to provide an ideal connection. The total thickness of these two layers is kept constant at 0.2 mm, while the stainless steel layer thickness changes from 0 to 0.2 mm. The thicknesses of 0 and 0.2 mm represent a pure copper layer and a pure stainless steel layer, respectively. The surface temperature profiles are shown in Figure 5.9. Correspondingly, the maximum and average surface temperatures are shown in Figure 5.10. As shown in Figures 5.9 and 5.10, the thickness effect shows an opposite effect on the temperature profiles compared to that in Figures 5.7 and 5.8. More specifically, when a copper base block is present, a thinner stainless steel surface has a lower overall surface temperature. The reason is that the copper base block provides additional lateral heat conduction capacity. A thinner stainless steel layer has a better chance to enhance lateral heat conduction through the copper material. Again, as the stainless steel layer thickness reaches 50μm, which is 2.5 times of the bubble radius, the thickness effect is diminished. Comparing Figures 5.9 and 5.7, it is found that as the thickness becomes larger than 50 μm, the temperature profiles are almost identical for the two conditions, with or without the copper base block. This result is important for justifying the experimental setup described in chapter 3. The stainless steel layer was selected with a thickness of 1 mm, compared to typical bubble radii of 0.02 to 0.08 mm, depending on pressure and bulk flow velocity. The ratio of the thickness to bubble radius is in the range of 12.5 to 50, which is much larger than the 2.5 obtained from the model calculations. This result assures that the 1 mm thickness stainless steel is adequate to represent the characteristics of the stainless steel in terms of flow boiling heat transfer.

The effect of bubble radius and heat flux was also numerically studied. Surface temperature profiles on copper and stainless steel surfaces are shown in Figures 5.11 and 5.12, respectively. The numerical solutions were obtained for a unit cell with radius of 0.1 mm, layer thickness of 0.2 mm, and wall heat flux of 1×10^5 W/m^2. The bubble sizes explored range from 0.02 mm to 0.08 mm. Equivalently, the ratio of bubble radius to unit cell radius ranged from 0.2 to 0.8. The bubble heat transfer coefficient with different bubble sizes was calculated from Equation (5-2). From Figure 5.11 and 5.12, the bubble radius shows a similar effect on surface temperature profiles on both heating surface materials. For large bubble sizes, the overall surface temperature is lower, which is shown in Figure 5.13. As discussed above, the temperature on surfaces without bubble coverage is partially controlled by the lateral heat conduction through the heating surface. With a larger bubble size, more surface area is covered by the bubble and which provides a high heat transfer coefficient. The lateral heat conduction resistance is also reduced due to a smaller lateral distance from the surface area not covered by a bubble to the portion covered by a bubble. In addition, the comparison between Figures 5.11 and 5.12 shows that the temperature profiles on both two surfaces are almost identical for various bubble radii, while the temperature magnitudes are different. This is explained by noting that current model is a steady-state model and the thermal conductivity shows only in the boundary conditions while not in the governing equation. Figure 5.13 also shows that the stainless steel surface temperature has a much stronger dependency on the bubble radius as compared to the copper surface. On the copper surface, the average temperature change with various bubble radii is within 0.1 K, while it's about 2.5 K on the stainless steel surface. This again is due to the high copper thermal conductivity, which ensures better lateral heat conduction and, therefore, a lower overall surface temperature as discussed previously. The surface temperature profiles on copper and stainless steel surfaces with different wall heat fluxes are shown in Figure 5.14 and 5.15, respectively. The numerical solutions are obtained in a unit cell with radius of 0.1 mm and thickness of 0.2 mm, and the bubble size is set at a constant 0.02 mm. The wall heat flux ranges from 1×10^5 to 5×10^5 W/m^2. On both surfaces, it's very clear that the overall temperature increases as the wall heat flux

increases. A linear relationship between surface temperature and the wall heat flux can be found in Figure 5.16. Bubble sizes won't remain constant as wall heat flux changes, the numerical results presented here, however, still shed some light on the impact of wall heat flux. This is not like the heating surface thickness and bubble radius, which have a stronger impact on stainless steel surfaces than on copper surfaces. Heat flux shows a strong impact on the surface temperature for both surfaces, as shown in Figure 5.16. This indicates that the flow boiling process is a strongly wall heat flux dependent process.

In summary, a simplified mathematical model has been proposed in this chapter to simulate steady-state heat conduction through the heating surface with bubble present. The heat transfer governing equation was derived for a unit cell, for which the radius is calculated from nucleation site density and the thickness is identical to the heating surface thickness. A bubble is treated as a heat sink with a high heat transfer coefficient. Impacts of several key parameters, such as heating surface material thermal conductivity, thickness, bubble size and wall heat flux on the surface temperature were numerically studied. It's found that with the same wall heat flux and bubble size, a heating surface with higher thermal conductivity tends to have a lower wall temperature due to better lateral heat conduction inside the heating block. Also, as the heating surface thickness becomes large enough, or more specifically 2.5 times the bubble radius, the thickness effect tends to be diminished. This finding again supports the selection that the 1 mm thick stainless steel used in the experiments to test the stainless steel material boiling heat transfer capacity is a good choice. The results also indicate that, both the bubble radius and thickness show a stronger effect on a stainless steel surface than on a copper one. This is mainly due to the much higher thermal conductivity of copper. The numerical results also indicate that flow boiling is a strongly wall heat flux dependent process.

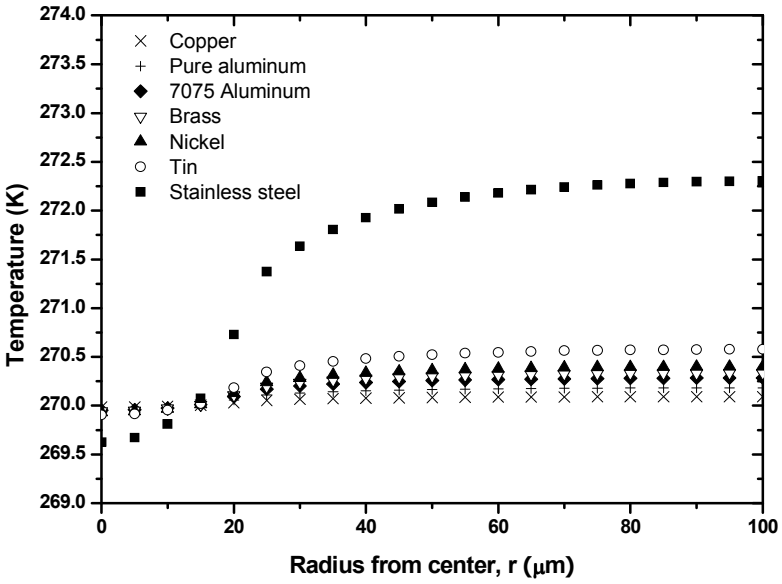

Figure 5.3. Surface temperature profiles on heating surfaces of materials with different thermal conductivities.

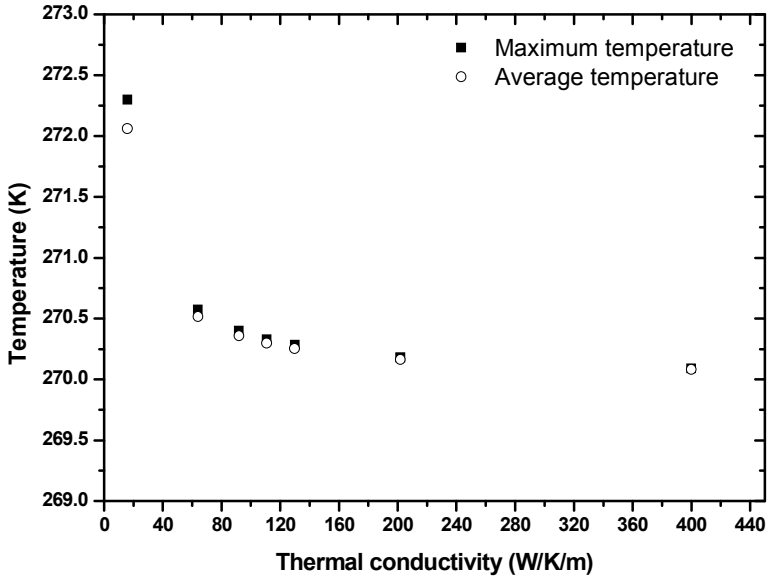

Figure 5.4. Maximum and average surface temperatures on heating surfaces of materials with different thermal conductivities.

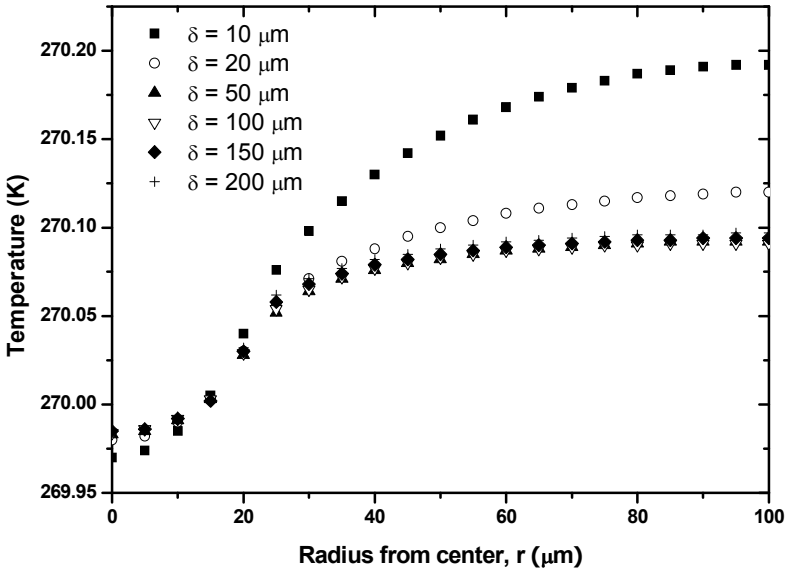

Figure 5.5. Surface temperature profiles on copper heating surfaces with different thicknesses.

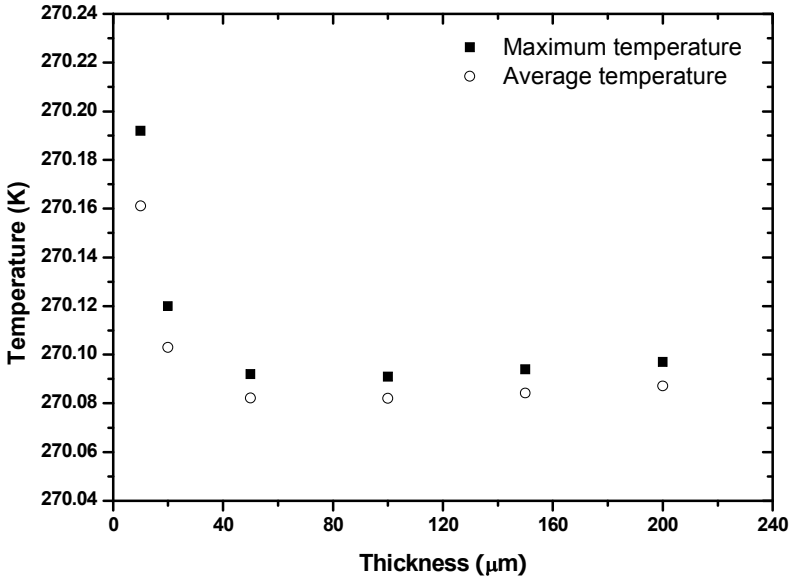

Figure 5.6. Maximum and average surface temperatures profiles on copper heating surfaces fordifferent thicknesses.

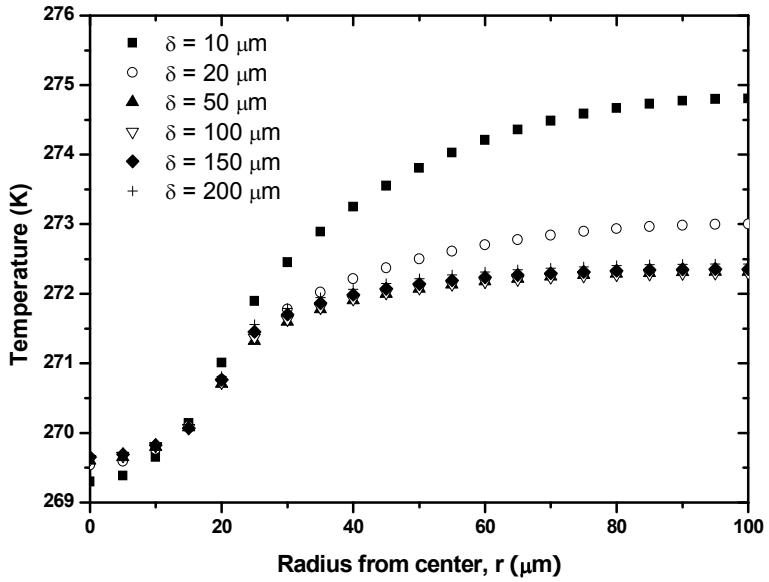

Figure 5.7. Surface temperature profiles on stainless steel heating surfaces for different thicknesses.

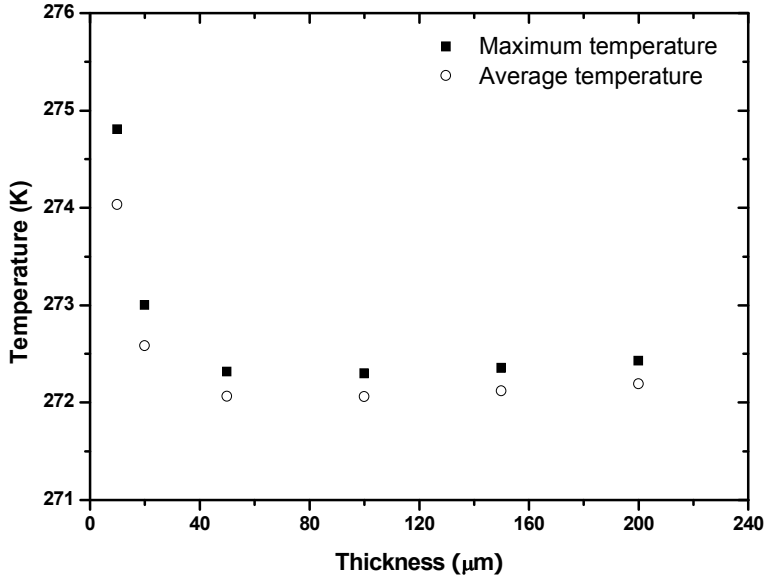

Figure 5.8. Maximum and average surface temperatures on a stainless steel heating surfaces at different thicknesses.

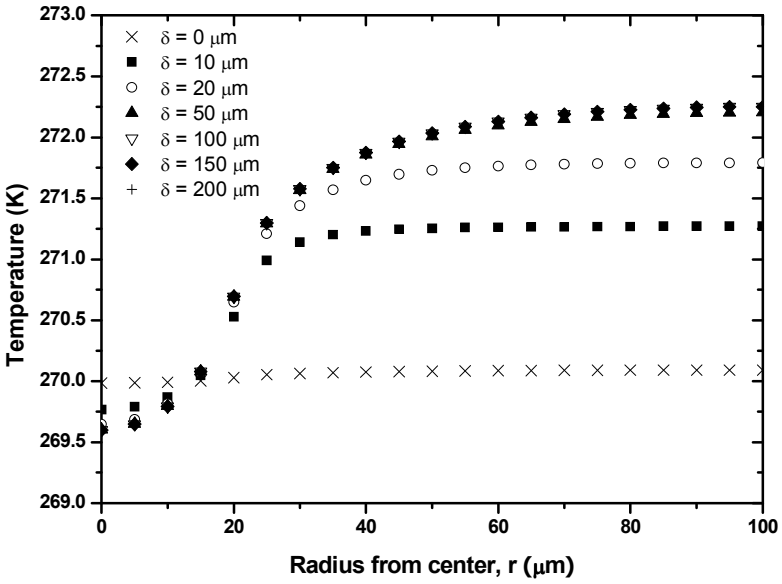

Figure 5.9. Surface temperature profiles on stainless steel heating surfaces with different thickness on a copper base block.

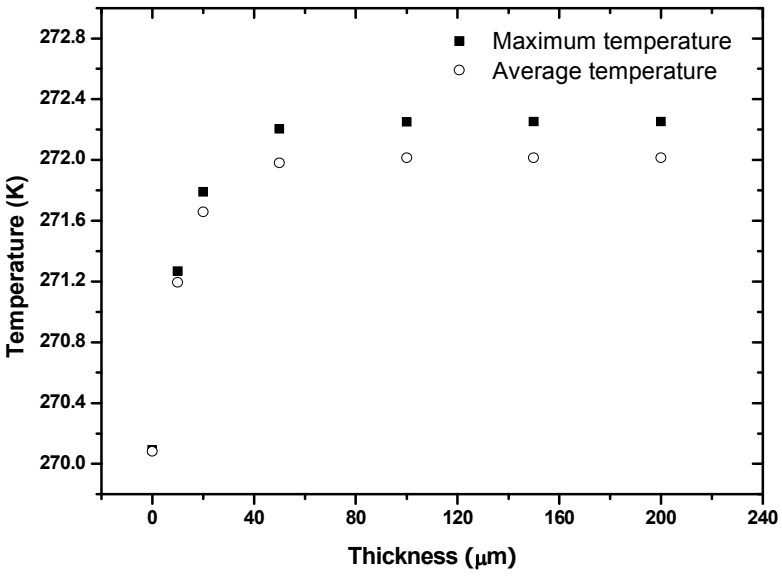

Figure 5.10. Maximum and average surface temperatures over a stainless steel heating surface with different thicknesses on a copper base block.

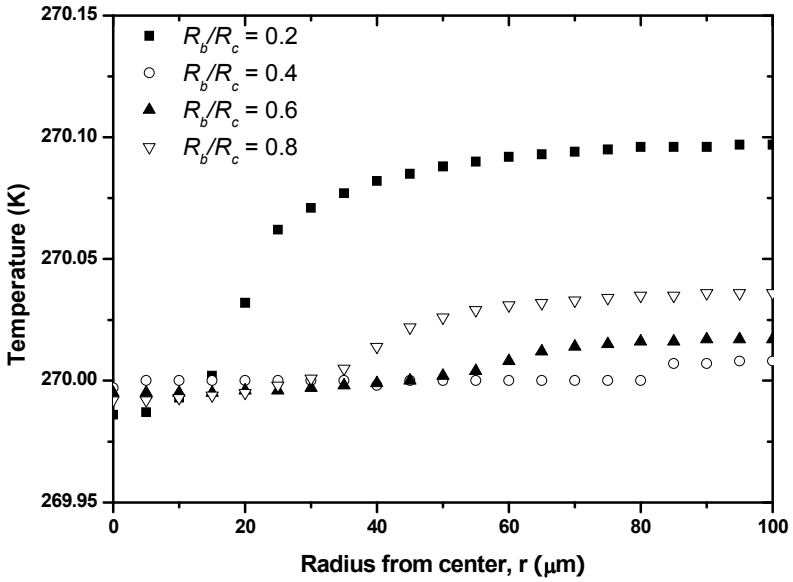

Figure 5.11. Surface temperature profiles on a copper heating surface as bubble size changes.

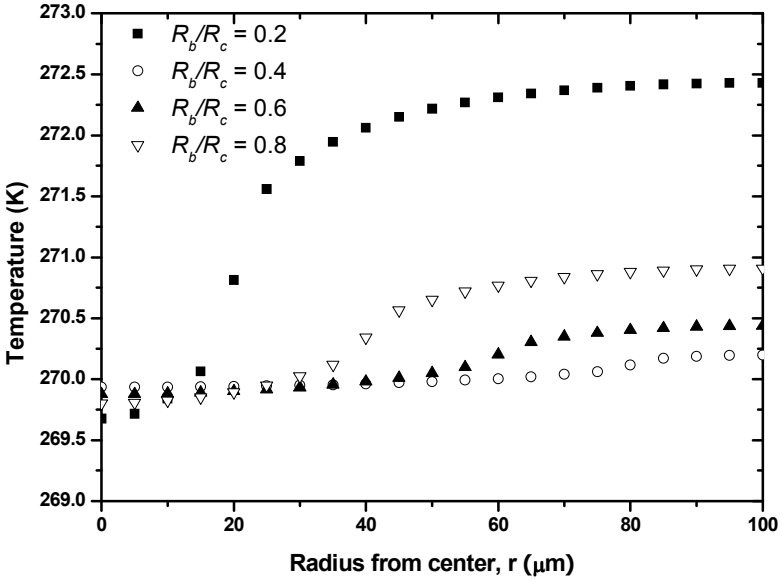

Figure 5.12. Surface temperature profiles on a stainless steel heating surface as bubble size changes.

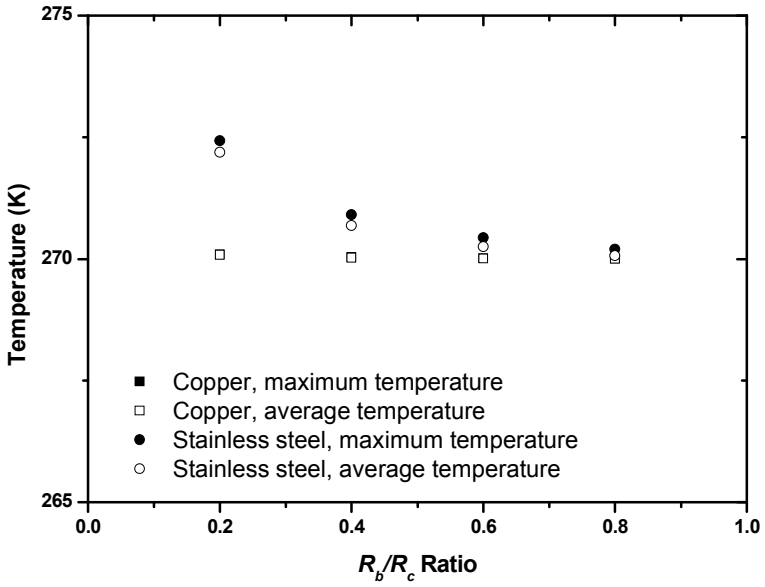

Figure 5.13. Maximum and average surface temperatures on both copper and stainless steel surfaces as bubble size changes.

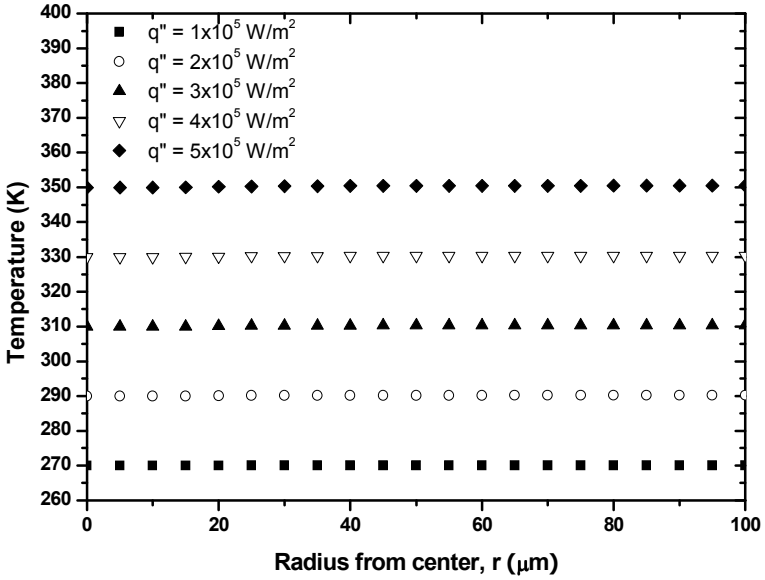

Figure 5.14. Surface temperature profiles on a copper heating surface as wall heat flux changes.

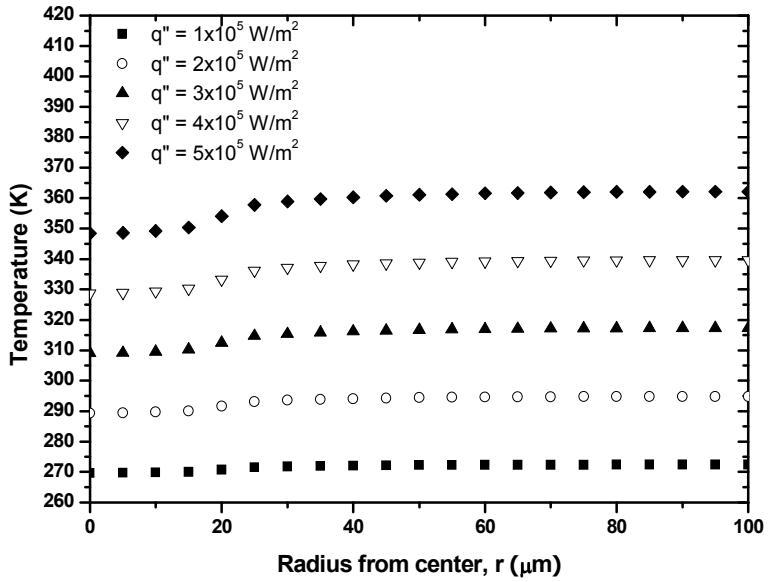

Figure 5.15. Surface temperature profiles on a stainless steel heating surface as wall heat flux changes.

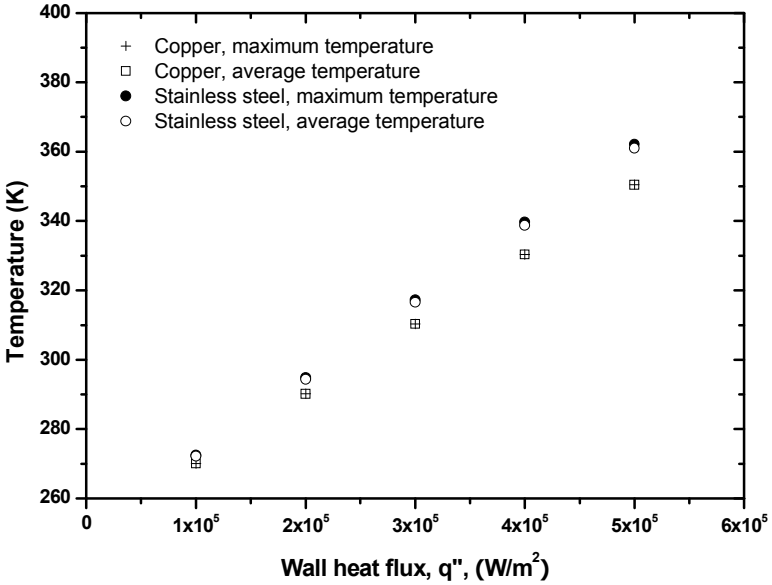

Figure 5.16. Maximum and average surface temperatures on both copper and stainless steel surfaces as wall heat flux changes.

CHAPTER 6

CONCLUSION AND FUTURE WORK

6.1 CONCLUSION AND DISCUSSION

Subcooled flow boiling has been found to have a very high heat transfer capacity while at low wall superheat. Subcooled flow boiling is especially of interest for nuclear industry applications since it's normally present in typical pressurized water reactor (PWR) cores and plays an important role in cooling the rector core. Other than the high heat transfer capacity, which is essential for nuclear reactor heat transfer, subcooled flow boiling is also of interest since it has been identified as a possible reason for inducing the CRUD (Chalk River Unidentified Deposits) layer found on fuel bundles. This layer potentially causes the undesired reactor power shift, normally referred as axial offset anomaly (AOA). In addition, the understanding of critical heat flux in subcooled flow boiling is critical for reactor safety and design of nuclear reactors.

The objective of this thesis was to experimentally study subcooled flow boiling from both macroscopic and microscopic points of view, through using a simulant coolant fluid, R134a. The experimental work mainly included subcooled flow boiling performance, nucleation site density and its distribution, and bubble dynamics. Nucleation site density, its distribution and bubble size data have been obtained from images and videos taken using a high-speed video camera. The subcooled flow boiling performance was directly estimated by measuring wall temperature and wall heat flux, which was implemented by mounting thermocouples into a heating block. The impact of thermal properties of surface materials on boiling heat transfer was examined by employing two different heating blocks made of copper and stainless steel, respectively. A simplified heat transfer model within the heating block was proposed to explain the different flow boiling behaviors between these two materials.

The nucleation site density has been experimentally studied and measured for both the copper and the stainless steel surfaces using a high-speed, high-fidelity video camera. The

nucleation site density data were correlated with wall superheat, critical cavity size and wall heat flux. All these parameters showed good correlation with nucleation site density. However, the wall superheat was not able to be correlated with nucleation site density data for different system pressures. This leads to the selection of critical cavity size as the new correlating parameter, to account for pressure effects. However, the critical cavity size does not achieve success in correlating the data for both surface materials. The wall heat flux does show good correlation with nucleation site density data for both surfaces.

The measured nucleation site distribution data was compared with a spatial Poisson distribution. This data show good agreement with the spatial Poisson distribution by counting nucleation site numbers in sub-domains. However, the comparison of the distribution of the nearest-neighbor distance indicates the experimentally obtained nucleation site density has a more uniform distribution than the spatial Poisson distribution. This is mainly due to interactions of bubbles and nucleation sites, because boiling system bubbles tend to be self-organized to cover as much heating surface area as possible. In addition, the copper surface has a more uniform bubble site distribution than the stainless steel surface. This can be explained by the interaction of nucleation sites due to lateral conduction inside the heating block. The heating surface beneath a vapor bubble is cooled by the bubble, thus having a relatively low temperature, and therefore another bubble can't be activated inside under influence of this existing bubble. The size of this low temperature zone is controlled by the lateral heat conduction inside the solid heating block and consequently by material's thermal conductivity. As heating surface material's thermal conductivity is higher, the size of this low temperature zone is larger due to better lateral heat conduction, and therefore has a more uniform nucleation site distribution.

Bubble dynamics is a very wide topic in a boiling system, especially in a flow boiling system due to its complexity and nonlinearity. In flow boiling, a bubble begins from an embryo and grows from this active nucleation site. After reaching a certain size, it departs and then may slide from its original site. A sliding bubble generally coalesces with a bubble downstream and lifts-off into the bulk flow. If heat fluxes are low, sliding bubbles may not

have a chance to coalesce before they lift-off. On the contrary, coalescence can happen before a bubble starts to slide, due to high bubble number densities. There are also intense interactions between bubbles and nucleation sites. A nucleation site can be activated or deactivated by an adjacent bubble or a bubble sliding from upstream, which occasionally happens. The bubble contact angle, or in other words, the surface wettability has also been observed to have significant impact on bubble behaviors and consequently boiling heat transfer. A high-speed digital camera has been used to visually study these bubble dynamics during the flow boiling experiments. In this study, some of the important parameters, which are directly related to boiling heat transfer capacity, were experimentally measured. Contact angles were measured for both material heating surfaces at different system pressures. The system pressure was found to have no apparent effect on the contact angle. The stainless surface has a slightly larger contact angle than the copper surface. The bubble growth rate was estimated by measuring bubble size at different times. It was found that Zuber's model fits the bubble growth experimental data to within a ±25% error. Again, the heating surface material does not display a significant effect on the bubble growth rate. The bubble waiting time was found to be negligible compared to bubble lifetime for both heating surfaces. With respect to bubble departure size, both the average liquid bulk velocity and the system pressure show significant effects. The comparison of bubble departure sizes for the two heating surfaces indicates heating surface material has a minor effect on bubble departure sizes. As a summary, copper and stainless steel heating surfaces were investigated with the same working fluid, R134a. Both surfaces have the same surface finish and also exhibit similar wettabilities. By comparing bubble parameters, it was found that the bubble dynamics are primarily controlled by liquid thermal and hydraulic conditions, while the heating surface thermal properties have a minor effect.

Flow boiling heat transfer performance on both the copper and the stainless steel surfaces, including parametric studies, were experimentally carried out in this study. Experimental data clearly show a trend that the copper surface has better performance than the stainless steel surface in terms of both heat transfer coefficient and critical heat flux.

Parametric studies, such as effects of pressure, bulk liquid velocity, and inlet subcooling level were also presented. The comparison between the current study and those of other researches shows good agreement. From experimental results obtained in the current study, it was concluded that heat flux is largely determined by nucleation site density. Also, the bubble dynamics on both surfaces show almost identical characteristics. The difference of boiling heat transfer between these two surfaces, however, raises a question as to what is the root-cause for the difference. A possible explanation is that the lateral heat transfer just inside the heating surface creates a non-uniform surface temperature distribution. This lateral heat transfer is determined by the heating surface thermal properties, such as thermal conductivity and thermal diffusivity, which are significantly different for the two heating surfaces investigated. This suggests further model development is needed to investigate the heat transfer inside the solid heating surface, from which a surface temperature profile can be obtained. This may shed some light on the boiling heat transfer performance differences.

A model was then developed to simulate the heat transfer inside the heating block when bubbles are present on the heating surface. On a heating surface, bubbles serve as a heat sink with a high heat transfer coefficient due to phase change. The temperature beneath a bubble, therefore, is expected to be low and close to the saturation temperature. The heating surface without bubbles covering it is then controlled by two heat transfer mechanisms, forced convection to the bulk flow and lateral heat conduction to the bubble covered region. Compared to phase change during bubble growth, the forced convection is relatively inefficient in transferring energy. If the thermal conductivity is sufficiently high, lateral heat conduction can be even more important than forced convection in transferring energy from the heating surface into the bulk flow. The results predicted by the model show that the thermal conductivity plays an important role through lateral heat conduction inside the heater block and, therefore, has a significant impact on boiling heat transfer performance.

6.2 FUTURE WORK

In this thesis work, copper and stainless steel heating surfaces with significantly different thermal properties, such as thermal conductivity, were experimentally studied. Experimental evidence shows that, , nucleation site density, bubbles growth rate and departure sizes, do not display significant differences between the two heating surfaces investigated. A further observation on contact angles of the working fluid, R134a, over the heating surfaces, indicates that both materials have fairly similar wettabilities with the working fluid. As discussed in previous chapters, similar bubble characteristics is mainly due to their similar surface wettabilities, while their different boiling heat transfer is due to their difference in thermal conductivity.

To further extend the current study, it's proposed to explore the effects of surface wettability on boiling heat transfer. The surface wettability may have two major effects on boiling, including its effect on nucleation site density and bubble dynamics. This can be visually observed with the techniques developed in the current and previous studies carried out by our laboratory. A commonly used way to alter the surface wettability is to utilize a nanocoating. The surface can be coated with either hydrophilic or hydrophobic material. As described in chapter 3, a new heating block with a stainless steel heating surface was manufactured separately for the current study. A similar approach can be used to prepare a heating surface using nanocoatings. A hydrophilic surface tends to have smaller contact angles, while a hydrophobic one tends to have larger contact angles, as shown in Figure 6.1. Also, due to the different shapes of bubbles, it's expected that bubbles will have different sliding characteristics in flow boiling. Bubbles tend to have round shapes on hydrophilic surfaces, while they tend to have flatter shapes on hydrophobic surfaces. Consequently, bubble shape will have an effect on forces bubbles experience during their growth and sliding phases. These forces include hydrostatic, hydrodynamic and surface tension, which are impacted by bubble size and shape. The shape and size of bubbles on hydrophilic and hydrophobic surfaces can be measured from images captured by the high-speed digital video camera used in the current study. More detailed force analyses are required to understand

bubble behavior differences between these two kinds of surfaces. In addition, the contact angle effect has been demonstrated to have an important effect on nucleation site density, which is an essential parameter in determining boiling heat transfer coefficients. Nucleation site densities can be measured by the methodology developed in this study, by taking bubble emit images from a top view using the video camera.

Other than single bubble dynamics, bubble size and shape are expected to have important impacts on multiple bubble interactions, such as bubbles coalescence and nucleation site interactions. On hydrophilic surfaces, bubbles tend to have spherical shapes and bubbles coalescence happens when two or more adjacent bubbles grow into contact. After coalescence, large bubbles normally form and lift-off from the heating surface. Some recent research (Phan 2009a) shows that on hydrophobic surfaces, vapor bubbles tend to coalescence and attach onto the surface to form a vapor blanket. This will potentially influence the critical heat flux as it's known that during nucleate boiling the formation of vapor blankets might trigger DNB (departure from nucleate boiling). Boiling heat transfer coefficients and critical heat fluxes can be experimentally measured at nominal pressures and temperatures in the Freon loop used in the current thesis study.

In addition, model development work study heat transfer near a growing bubble, including the heat transfer inside the heating block, in the fluid region near the bubble base, the evaporation in the microlayer beneath a bubble and a potential condensation on the apex of a bubble. The heat transfer in the solid and liquid phases is dominant by heat conduction and can be described by two-dimensional Laplace formulations. On the liquid-solid interface, energy conservation has to be satisfied. On the liquid-vapor interface, a similar boundary condition will be applied, except that the heat transfer is either by evaporation or condensation. Moreover, it's generally hypothesized that a liquid microlayer is present beneath a growing bubble and evaporation takes place on the interface between this microlayer and the vapor bubble. With these more advanced features, the model may be able to predict a more complete picture of heat transfer near a bubble. Comparing the model developed in the current study, the proposed modeling may provide better understanding of

bubble behavior and a more accurate prediction on the effect of bubbles on heat transfer from the heating block. Such a model may provide more insight into the differences between hydrophilic and hydrophobic surfaces.

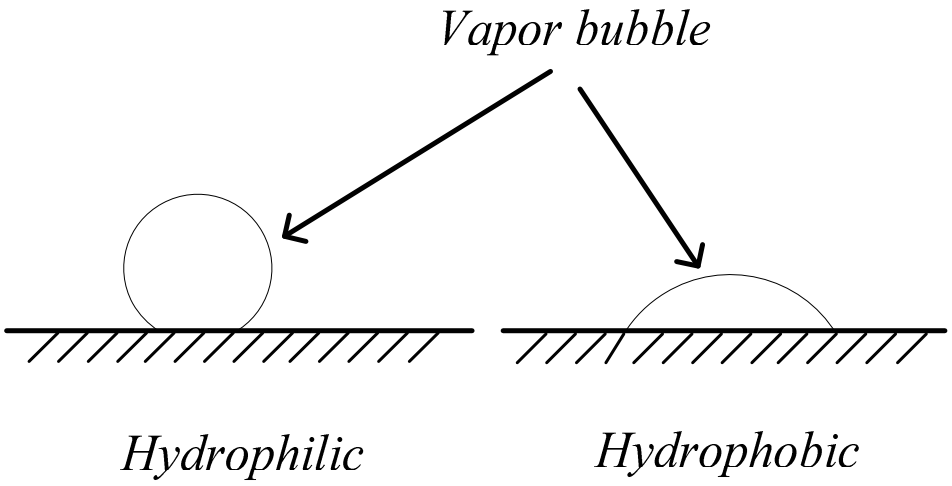

Figure 6.1, Bubbles on hydrophilic and hydrophobic surfaces.

REFERENCE

Akshoy Ranjan, P., Sanchayan, M. and Pijush, R. 2005. *Mechanical science: Engineering thermodynamics and fluid mechanics*. New Delhi: Prentice-Hall of India Private Limited.

Bankoff, S.G. 1958. Entrapment of gas in the spreading of a liquid over a rough surface. *A.I.Ch.E. Journal* 4:24-26

Bang, I.C., Chang, S.H., and Baek, W.P. 2004. Visualization of the subcooled flow boiling of R-134a in a vertical rectangular channel with an electrically heated wall. *International Journal of Heat and Mass Transfer* 47:4349-4363.

Basu, N., Warrier, G.R., and Dhir, V.K. 2002. Onset of nucleate boiling and active nucleation site density during subcooled flow boiling. *Journal of Heat Transfer* 124:717-728.

Basu, N., Warrier, G.R., and Dhir, V.K. 2005a. Wall heat flux partitioning during subcooled flow boiling: Part 1-Model development. *Journal of Heat Transfer* 127(2):131-140.

Basu, N., Warrier, G.R., and Dhir, V.K. 2005b. Wall heat flux partitioning during subcooled flow boiling: Part 2-Model validation. *Journal of Heat Transfer* 127(2):141-148.

Benjamin, R.J. and Balakrishnan, A.R. 1997. Nucleation site density in pool boiling of saturated pure liquids: Effect of surface microroughness and surface and liquid physical properties. *Experimental Thermal and Fluid Science* 15:32-42.

Berenson, P.J. 1962. Experiments on pool-boiling heat transfer. *International Journal of Heat and Mass Transfer* 5:985-999.

Bergles, A.E. and Rohsenow, W.M. 1964. The determination of forced-convection surface-boiling heat transfer. *Journal of Heat Transfer* 86:365-372.

Bier, K., Gorenflo, D., Salem, M. and Tanes, Y. 1978. Pool boiling heat transfer and size of active nucleation centers for horizontal plates with different surface roughness. Paper presented at Proceedings of the 6th International Heat Transfer Conference, Vol. 1:151–156. August 7-11, in Toronto, Canada.

Bliss, F.E., Jr., Hsu, S.T., and Crawford, M. 1969. An investigation into the effects of various platings on the film coefficient during nucleate boiling from horizontal tubes. *International Journal of Heat and Mass Transfer* 12:1061-1072.

Bonilla, C.F. and Perry, C.W. 1941. Heat transmission to boiling binary liquid mixtures, *Trans. AIChE*, Vol. 37:685-705.

Bowring, R.W. 1962. Physical model based on bubble detachment and calculation of steam voidage in the subcooled region of a heated channel. *OECD Halden Reactor Project Report HPR-10.*

Calka, A. and Judd, R.L. 1985. Some aspects of the interaction among nucleation sites during saturated nucleate boiling. *Int. J. Heat Mass Transfer* 28(12):2331-2342.

Chekanov, V.V. 1977. Interaction of centers in nucleate boiling. *High Temp. Phys.* 15:101-106. (Translated from *Teplofizika Vysokikh Temperatur*. 15(1):121-128. 1977)

Chai, L.H. 2004. A theoretical analysis of bubble interaction in boiling systems. *International Journal of Thermal Sciences* 43(11):1067-1073.

Chai, L.H., Peng, X.F. and Wang, B.X. 2000. Nucleation site interaction during boiling. *International Journal of Heat and Mass Transfer* 43:4249-4258.

Chang, S.H., Bang, I.C., and Baek, W.P. 2002. A photographic study on the near-wall bubble behavior in subcooled flow boiling. *Int. J. Therm. Sci.* 41:609-628.

Chen, J.C. 1966. Correlation for boiling heat transfer to saturated liquids in convective flow. *Int. Eng. Chem. Process Design and Development* 5:322-329.

Cole, R. 1960. A photographic study of pool boiling in the region of critical heat flux. *A.I.Ch.E. Journal* 6:533-538.

Cole, R., and Shulman, H.L. 1966. Bubble departure diameters at subatmospheric pressures. *Chem. Eng. Prog. Symp. Ser.* 62:6-16.

Cole, R. 1967. Frequency and departure diameter at sub-atmospheric pressures. *A.I.Ch.E. Journal* 13:779-783.

Cole, R. and Rohsenow, W.M. 1968. Correlation of bubble departure diameters for boiling of saturated liquids. *Chem. Eng. Prog. Symp. Ser.* 65:211-213.

Collier, J.G. and Thome, J.R., *Convective boiling and condensation*, 3rd edition, Oxford University Press, 1996.

Cooper, M.G. 1984. Saturation nucleate boiling, a simple correlation. Paper presented at the 1st U.K. Natn. Conf. on Heat Transfer, July 3-5, in University of Leeds.

Cornwell, K. and Brown, R.D. 1978. Boiling surface topography. Paper presented at Proceedings of the 6th International Heat Transfer Conference, Vol. 1:157–161. August 7-11, in Toronto, Canada.

Donnelly, B., O'Donovan, T.S., and Murray, D.B. 2009. Surface heat transfer due to sliding bubble motion. *Applied Thermal Engineering* 29(7):1319-1326.

Del Valle M., V.H. and Kenning, D.B.R. 1985. Subcooled flow boiling at high heat flux. *Int. J. Heat Mass Transfer* 28(10):1907-1920.

Dittus, F.W. and Boelter, L.M.K. 1930. Heat transfer in automobile radiators of the tubular type. *University of California Publication in Engineering* 2:443-446.

Eddington, R.I. and Kenning, D.B.R. 1978. The prediction of flow boiling bubble populations from gas bubble nucleation experiments. Paper presented at Proceedings of the 6th International Heat Transfer Conference, Vol. 1:275–280. August 7-11, in Toronto, Canada.

Eddington, R.I., Kenning, D.B.R., and Korneichev, A.I. 1978. Comparison of gas and vapor bubble nucleation on a brass surface in water. *Int. J. Heat Mass Transfer* 21(7):855-862.

Eddington, R.I. and Kenning, D.B.R. 1979. The effect of contact angle on bubble nucleation. *Int. J. Heat Mass Transfer* 22(8):1231-1236.

Farber, E.A. and Scorah, R.L. 1968. Heat transfer to water boiling under pressure. *Trans ASME*, Vol. 70:369-384.

Gaertner, R.F. and Westwater, J.W. 1963. Population of active sites in nucleate boiling heat transfer. *Chem. Eng. Prog. Symp. Ser.* 56(30):39-48.

Gaertner, R.F. 1963. Distribution of active sites in the nucleate boiling of liquids. *Chem. Eng. Prog. Symp. Ser.* 59(41):52-61.

Gnielinski, V. 1976. New equations for heat and mass transfer in turbulent pipe and channel flow. *International Chemical Engineering* 16:359-368.

Golobič, I. and Gjerkeš. H. 2001. Interactions between laser-activated nucleation sites in pool boiling. *International Journal of Heat and Mass Transfer* 44:143-153.

Gorenflo, D., Chandra, U., Kotthoff, S., and Luke, A. 2004. Influence of thermophysical properties on pool boiling heat transfer of refrigerants. *Int. J. Refrig.* 27:492-502.

Griffith, P. and Wallis, J.D. 1960. The role of surface conditions in nucleate boiling. *Chem. Eng. Prog. Symp. Ser.* 56(30):49-63.

Hardenberg, J.V., Kenning, D.B.R., Xing, H. and Smith, L.A. 2004. Identification of nucleation site interactions. *International Journal of heat and Fluid Flow* 25:298-304.

Han, C.Y. and Griffith, P. 1965. The mechanism of heat transfer in nucleate pool boiling-Part I, Bubble initiation, growth and departure. *Int. J. heat Mass Transfer* 8:887-904.

Hibiki, T. and Ishii, M. 2003. Active nucleation site density in boiling system. *International Journal of Heat and Mass Transfer* 46:2587-2601.

Hsu, Y.Y. 1962. On the size range of active nucleation cavities on a heating surface. *Journal of Heat Transfer* 84:207-212.

Jens, W.H. and Lottes, P.A. 1951. Analysis of heat transfer burnout, pressure drop and density data for high pressure water. USAEC Rep. ANL-4627.

Judd, R. L. and Lavdas, C.H. 1980. The nature of nucleation site interaction. *Journal of Heat Transfer 102*:461-464.

Judd, R.L. and Chopra, A. 1993. Interaction of nucleation processes occurring at adjacent nucleation sites. *Journal of Heat Transfer* 115:955-962.

Judd, R.L. 1988. On nucleation site interaction. *Journal of Heat Transfer* 110:475-478.

Kandlikar, S.G. 1990. A general correlation for saturated two-phase flow boiling heat transfer inside horizontal and vertical tubes. *Journal of Heat Transfer* 112(1):219-228.

Kandlikar, S.G. 1991. Development of a flow boiling map for subcooled and saturated flow boiling of different fluids inside circular tubes. *Journal of Heat Transfer* 113(1):190-200.

Kandlikar, S.G. 1997. Further development in subcooled flow boiling heat transfer. Paper presented at the Engineering Foundation Conference on Convective and Pool Boiling, May 18-25, in Irsee, Germany.

Kandlikar, S.G. 1998. Heat transfer characteristics in partial boiling, fully developed boiling, and significant void flow regions of subcooled flow boiling. *Journal of Heat Transfer* 120(2):395-401

Kandlikar, S.G., Mizo, V., Cartwright, M., and Ikenze, E. 1997. Bubble nucleation and growth characteristics in subcooled flow boiling of water. Paper presented at the National Heat Transfer Conference Volume 4. HTD-Vol. 342:11-18

Kenning, D.B.R. and Del Valle M., V.H. 1981. Fully-developed nucleate boiling: Overlap of areas of influence and interference between bubble sites. *Int. J. Heat Mass Transfer* 24(6):1025-1032.

Klausner, J.F., Mei, R., Bernhard, D.M. and Zeng, L.Z. 1993. Vapor bubble departure in forced convection boiling. *Int. J. Heat Mass Transfer* 36(3):651-662.

Kocamustafaogullari, G. and Isshi, M. 1983. Interfacial area and nucleation site density in boiling system. *Int. J. Heat Mass Transfer* 26:1377-1387.

Kutateladze, S.S. 1961. Boiling heat transfer. *Int. J. Heat Mass Transfer* 4:31-45.

Liu, Z. and Winterton, R.H.S. 1989. A general correlation for saturated and subcooled flow boiling in tubes and annuli, based on a nucleate pool boiling equation. *Int. J. Heat Mass Transfer* 34:2759-2766.

Mikic, B.B., Rohsenow, W.M., and Griffith, P. 1970. On bubble growth rates. *Int. J. Heat Mass Transfer* 13:657-666.

McAdams, W.H., Minden, C.S., Carl, R., Picornell, D.M., and Dew, J.E. 1949. Heat transfer at high rates to water with surface boiling. *Ind. Eng. Chem.* 41:1945-1953.

Mallozzi, R., Judd, R.L., and Balakrishnan, N. 2000. Investigation of randomness, overlap and the interaction of bubbles forming at adjacent nucleation sites in pool boiling. *International Journal of Heat and Mass Transfer* 43:3317-3330.

Mosdorf, R. and Shoji, M. 2004. Chaos in nucleate boiling – nonlinear analysis and modeling. *International Journal of Heat and Mass Transfer* 47:1515-1524.

Mosdorf, R. and Shoji, M. 2008. Hydrodynamic aspects of interaction between nucleation sites. *International Journal of Heat and Mass Transfer* 51:3378-3386.

Mei, R., Chen, W.C., and Klausner, J.F. 1995a. Vapor bubble growth in heterogeneous boiling – I. Formulation. *Int. J. Heat Mass Transfer* 38(5):909-919.

Mei, R., Chen, W.C., and Klausner, J.F. 1995b. Vapor bubble growth in heterogeneous boiling – I. Growth rate and thermal fields. *Int. J. Heat Mass Transfer* 38(5):921-934.

Mikic, B.B. and Rohsenow, W.M. 1969. A new correlation of pool boiling data including the effect of heating surface characteristics. *Journal of Heat Transfer* 91:245-250.

Petukhov, B.S. and Popov, V.N. 1963. Theoretical calculation of heat exchange in turbulent flow in tubes of an incompressible fluid with variable physical properties. *High Temp.* 1:69-83.

Phan, H.T., Caney, N., Marty, P., Colasson, S., and Gavillet. J. 2009a. How does surface wettability influence nucleate boiling? *C. R. Mecanique* 337:251-259.

Phan, H.T., Caney, N., Marty, P., Colasson, S., and Gavillet. J. 2009b. Surface wettability control by nanocoating: The effects on pool boiling heat transfer and nucleation mechanism *International Journal of Heat and Mass Transfer* 52:5459-5471.

Plesset, M.S. and Zwick, S.A. 1952. A nonsteady heat diffusion problem with spherical symmetry. *Journal of Applied Physics* 23:95-98.

Plesset, M.S. and Zwick, S.A. 1954. The growth of vapor bubble in superheated liquids. *Journal of Applied Physics* 25:493-500.

Podowski, M.Z. and Podowski, R.M. 2009. Mechanistic multidimensional modeling of forced convection boiling heat transfer. *Science and Technology of Nuclear Installations,* Volume 2009, Article ID 387020, Hindawi Publishing Corporation.

Podowski, R.M., Drew, D.A., Lahey Jr., R.T., and Podowski, M.Z. 1997. A mechanistic model of the ebullition cycle in forced convection subcooled boiling, in: *Eight International Topical Meeting on Nuclear Reactor Thermal-Hydraulics* 3:1535 – 1542.

Prodanovic, V., Fraser, D., and Salcudean, M. 2002. Bubble behavior in subcooled flow boiling of water at low pressures and low flow rates. *International Journal of Multiphase Flow* 28(1):1-19.

Qi, Y.S., Klausner, J.F., and Mei, R. 2004. Role of surface structure in heterogeneous nucleation. *International Journal of Heat and Mass Transfer* 47:3097-3107.

Rayleigh, L. 1917. On the pressure developed in a liquid during the collapse of a spherical cavity. *Phil. Mag.* 34:94-98.

Ribatski, G. and Saiz Jabardo, J.M. 2003. Experimental study of nucleate boiling of halocarbon refrigerants on cylindrical surfaces. *Int. J. Heat Mass Transfer* 46:4439-4451.

Rohsenow, W.M. 1952. A method of correlating heat transfer data for surface boiling liquids. *J. Heat Transfer* 74:969-976.

Shoji, M. 2004. Studies of boiling chaos: a review. *International Journal of Heat and Mass Transfer* 47:1105-1128.

Shah, M.M. 1976. A new correlation for heat transfer during boiling flow through pipes. *ASHRAE Trans.* 82:66-86.

Shah, M.M. 1977. A general correlation for heat transfer during subcooled boiling in pipes and annuli. *ASHRAE Trans.* 83:205-215.

Shah, M.M. 1982. Chart correlation for saturated boiling heat transfer: Equations and further study. *ASHRAE Trans.* 88:185-196.

Sateesh, G., Das, S.K., and Balakrishnan, A.R. 2005. Analysis of pool boiling heat transfer: effect of bubbles sliding on the heating surface. *International Journal of Heat and Mass Transfer* 48:1543-1553.

Thorncroft, G.E. and Klausner, J.F. 1999. The influence of vapor bubble sliding on forced convection boiling heat transfer. *Journal of Heat Transfer* 121:73-79.

Thom, J.R.S., Walker, W.M., Fallon, T.A., and Reising, G.F.S. 1965. Boiling in subcooled water during flow up heated tubes or annuli. Paper presented at the Symposium on Boiling Heat Transfer in Steam Generating Units and Heat Exchanger held by Inst. Mech. Engrs., September 15-16, in Manchester, England.

Tong, L.S. and Tang, Y.S., *Boiling heat transfer and two-phase flow*, Taylor and Francis, 1997.

Vadgama, B. and Harris, D.K. 2007. Measurements of the contact angle between R134a and both aluminum and copper surfaces. *Experimental Thermal and Fluid Science* 31:979-984.

Wang, C.H. and Dhir, V.K. 1993a. Effect of surface wettability on active nucleation site density during pool boiling of saturated water. *Journal of Heat Transfer* 115:659-669.

Wang, C.H. and Dhir, V.K. 1993b. On the gas entrapment and nucleation site density during pool boiling of saturated water. *Journal of Heat Transfer* 115:670-679.

Wu, J.Y., Farouk, T. and Ward, C.A. 2007. Pressure dependence of the contact angle. *J. Phys. Chem. B* 111:6189-6197.

Wu, W. 2007, Combined Modeling and Experimental Validation of Boiling Curve and Critical Heat Flux, Ph.D Thesis, University of Illinois at Urbana-Champaign.

Yan, Y., Kenning, D.B.R., and Cornwell, K. 1997. Sliding and sticking vapor bubbles under inclined plane and curved surfaces. *International Journal of Refrigeration* 20:583-591.

Yang, S.R. and Kim, R.H. 1988. A mathematical-model of the pool boiling nucleation site density in terms of the surface characteristics. *Int. J. Heat Mass Transfer* 31:1127-1135.

Zeng, L.Z., Klausner, J.F., and Mei, R. 1993. A unified model for the prediction of bubble detachment diameters in boiling systems— I. Pool boiling. *Int. J. Heat Mass Transfer* 36(9):2261-2270.

Zeng, L.Z., Klausner, J.F., Bernhard, D.M., and Mei, R. 1993. A unified model for the prediction of bubble detachment diameters in boiling systems— I. Flow boiling. *Int. J. Heat Mass Transfer* 36(9):2271-2279.

Zeng, L.Z. and Klausner, J.F. 1993. Nucleation site density in forced convection boiling. *Journal of Heat Transfer* 115(1):215-221.

Zuber, N. 1961. The dynamics of vapor bubbles in nonuniform temperature fields. *Int. J. Heat Mass Transfer* 2:83-98.

AUTHOR'S BIOGRAPHY

Ling Zou was born in Jiangxi Province, P. R. China on July 06, 1980. He received a Bachelor of Science degree in Engineering Physics from Tsinghua University in July 2000. He then received a Master of Science degree in Nuclear Engineering from China Institute of Atomic Energy in July 2003. After that, he shortly worked in China Institute of Atomic Energy before he was enrolled as a graduate student for his Ph.D. study in the Department of Nuclear, Plasma and Radiological Engineering at University of Illinois at Urbana-Champaign.